



NAVAL POSTGRADUATE SCHOOL

MONTEREY, CALIFORNIA

THESIS

**MODELING AND DEMONSTRATING REGENERATIVE
BRAKING OF A SQUIRREL CAGE INDUCTION MOTOR
WITH VARIOUS DECELERATION RATES USING V BY F
CONTROL**

by

Billy J. Nytko

June 2010

Thesis Co-Advisors:

Alexander L. Julian
Roberto Cristi

Approved for public release; distribution is unlimited

THIS PAGE INTENTIONALLY LEFT BLANK

REPORT DOCUMENTATION PAGE			<i>Form Approved OMB No. 0704-0188</i>	
Public reporting burden for this collection of information is estimated to average 1 hour per response, including the time for reviewing instruction, searching existing data sources, gathering and maintaining the data needed, and completing and reviewing the collection of information. Send comments regarding this burden estimate or any other aspect of this collection of information, including suggestions for reducing this burden, to Washington headquarters Services, Directorate for Information Operations and Reports, 1215 Jefferson Davis Highway, Suite 1204, Arlington, VA 22202-4302, and to the Office of Management and Budget, Paperwork Reduction Project (0704-0188) Washington DC 20503.				
1. AGENCY USE ONLY (Leave blank)		2. REPORT DATE June 2010	3. REPORT TYPE AND DATES COVERED Master's Thesis	
4. TITLE AND SUBTITLE Modeling and Demonstrating Regenerative Braking of a Squirrel Cage Induction Motor with Various Deceleration Rates Using V by F Control			5. FUNDING NUMBERS	
6. AUTHOR(S) Billy J. Nytko				
7. PERFORMING ORGANIZATION NAME(S) AND ADDRESS(ES) Naval Postgraduate School Monterey, CA 93943-5000			8. PERFORMING ORGANIZATION REPORT NUMBER	
9. SPONSORING /MONITORING AGENCY NAME(S) AND ADDRESS(ES) N/A			10. SPONSORING/MONITORING AGENCY REPORT NUMBER	
11. SUPPLEMENTARY NOTES The views expressed in this thesis are those of the author and do not reflect the official policy or position of the Department of Defense or the U.S. Government. IRB Protocol Number _____				
12a. DISTRIBUTION / AVAILABILITY STATEMENT Approved for public release; distribution is unlimited			12b. DISTRIBUTION CODE	
13. ABSTRACT (maximum 200 words) Currently, the world's predicament regarding fuel shortages affects the daily activities of nations and directly affects national security. The concept of starving an aggressive nation of resources, in particular fuel, is a war tactic that is effective in preventing the aggressor from accomplishing objectives. This was proven in World War II. National security is affected because shortages leave nations defenseless against invaders. Warfare methodologies will change drastically to accommodate the inability to use fossil fueled assets unless alternative energy sources are found. The focus of this research is to use computer software and electrical hardware available to the Naval Postgraduate School (NPS) to model regenerative braking to support energy conservation technologies and to improve the efficiencies within the United States Navy (USN). The goal of this research is to demonstrate regenerative braking during the deceleration of an induction motor and analyze various aspects during the braking process. This will help in the further development for the "All Electric Ship" by exploring methods to increase its longevity, while improving the efficiency of energy recovery technology. The USN will realize a degree of freedom from fossil fuel and be capable of employing future, more versatile energy recovery systems for Naval base infrastructure.				
14. SUBJECT TERMS Regenerative Braking, Dynamic Braking, Rheostatic Braking, all electric vehicle, all electric ship			15. NUMBER OF PAGES 149	
			16. PRICE CODE	
17. SECURITY CLASSIFICATION OF REPORT Unclassified	18. SECURITY CLASSIFICATION OF THIS PAGE Unclassified	19. SECURITY CLASSIFICATION OF ABSTRACT Unclassified	20. LIMITATION OF ABSTRACT UU	

NSN 7540-01-280-5500

Standard Form 298 (Rev. 2-89)
Prescribed by ANSI Std. Z39-18

THIS PAGE INTENTIONALLY LEFT BLANK

Approved for public release; distribution will be unlimited

**MODELING AND DEMONSTRATING REGENERATIVE BRAKING OF A
SQUIRREL CAGE INDUCTION MOTOR WITH VARIOUS DECELERATION
RATES USING V BY F CONTROL**

Billy J. Nytko
Lieutenant, United States Navy
B.S., Civil Engineering, University of Nevada, Las Vegas, 2000

Submitted in partial fulfillment of the
requirements for the degree of

MASTER OF SCIENCE IN ELECTRICAL ENGINEERING

from the

**NAVAL POSTGRADUATE SCHOOL
June 2010**

Author: Billy J. Nytko

Approved by: Alexander L. Julian
Thesis Advisor

Roberto Cristi
Thesis Co-Advisor

R. Clark Robertson
Chairman, Department of Electrical and Computer Engineering

THIS PAGE INTENTIONALLY LEFT BLANK

ABSTRACT

Currently, the world's predicament regarding fuel shortages affects the daily activities of nations and directly affects national security. The concept of starving an aggressive nation of resources, in particular fuel, is a war tactic that is effective in preventing the aggressor from accomplishing objectives. This was proven in World War II. National security is affected because shortages leave nations defenseless against invaders. Warfare methodologies will change drastically to accommodate the inability to use fossil fueled assets, unless alternative energy sources are found.

The focus of this research is to use computer software and electrical hardware available to the Naval Postgraduate School (NPS) to model regenerative braking to support energy conservation technologies and to improve the efficiencies within the United States Navy (USN). The goal of this research is to demonstrate regenerative braking during the deceleration of an induction motor and analyze various aspects during the braking process. This will help in the further development for the "All Electric Ship" by exploring methods to increase its longevity, while improving the efficiency of energy recovery technology. The USN will realize a degree of freedom from fossil fuel and be capable of employing future, more versatile energy recovery systems for naval base infrastructure.

THIS PAGE INTENTIONALLY LEFT BLANK

TABLE OF CONTENTS

I.	INTRODUCTION.....	1
A.	MISSION APPLICABILITY	1
B.	THE MOTIVATION FOR REGENERATIVE BRAKING	2
C.	BRIEF HISTORY OF REGENERATIVE BRAKING.....	3
1.	The First Steps to Regenerative Braking.....	3
2.	The Inventor of Regenerative Braking	4
D.	OBJECTIVE	5
E.	RESEARCH APPROACH.....	5
F.	THESIS OVERVIEW AND DESCRIPTION	6
II.	EXPERIMENT PREPARATION	7
A.	THEORY	7
1.	Induction Motor Theory	7
2.	Demonstration of Three and Two-Phase Power Calculations.....	17
B.	SOFTWARE AND EQUIPMENT	30
1.	Software and Hardware Continuity Validation.....	30
2.	Electrical and Mechanical Energy Storage	32
3.	Understanding Software and Hardware Interfaces.....	36
III.	REGENERATIVE BRAKING MODELING	41
A.	MODEL SETUP.....	41
B.	TESTING SR-FLIP FLOP OF MODEL.....	48
C.	TESTING THE DELAY TRIGGER MODEL COMPONENT.....	51
IV.	RESULTS	55
A.	COMMANDED AND ACTUAL ANGULAR VELOCITIES, POWER, AND CHANGE IN VOLTAGE ANALYSIS	56
B.	EXPERIMENT COMPARISON ANALYSIS	67
C.	ANGULAR VELOCITY DIFFERENCE ANALYSIS.....	75
D.	PHASE A CURRENT BEHAVIOR ANALYSIS	84
E.	ENERGY ANALYSIS	87
V.	CONCLUSION AND FUTURE RESEARCH RECOMMENDATIONS	91
A.	CONCLUSION	91
B.	FUTURE RESEARCH RECOMMENDATIONS	91
APPENDIX A: SIMULINK MODELS AND MATLAB CODE USED TO GENERATE FIGURES 3 THROUGH 12		93
APPENDIX B: DATA SHEETS [12]		97
APPENDIX C: MATLAB CODE TO GENERATE CAPACITANCE OPTIMIZATION PLOT.....		99
APPENDIX D: MATLAB CODE TO GENERATE FIGURES 33 THROUGH 60.....		101
APPENDIX E: FILTER DESIGNS		119

APPENDIX F: POWER INTEGRATOR TO CALCULATE ENERGY.....	125
LIST OF REFERENCES.....	127
INITIAL DISTRIBUTION LIST	129

LIST OF FIGURES

Figure 1.	Two-pole, 3-phase, Wye-Connected Symmetrical Induction Machine [9]	10
Figure 2.	Transformation for Rotating Circuits Portrayed by Trigonometric Relationships (After [9])	15
Figure 3.	Leading Phase Shift Condition	19
Figure 4.	Zero Phase Shift Condition	19
Figure 5.	Lagging Phase Shift Condition	20
Figure 6.	Current Leads Voltage 45 degrees	21
Figure 7.	Current Leads Voltage 36 degrees	21
Figure 8.	Current Leads Voltage 27 degrees	22
Figure 9.	Current Leads Voltage 18 degrees	22
Figure 10.	Current Voltage Phases are Equal (Power at Maximum)	23
Figure 11.	Three-Dimensional Power Optimization Graph	24
Figure 12.	Wye-Connected Circuit	25
Figure 13.	Three and Two-Phase Power Calculation Methods Simulink Model	27
Figure 14.	Voltage and Current Input Signals for Three-Phase Calculator	28
Figure 15.	Sensor Connections for Three-Phase Power Calculator	28
Figure 16.	Voltage and Current Input Signals for Two-Phase Calculator	29
Figure 17.	Sensor Connections for Two-Phase Power Calculator	29
Figure 18.	Three-Phase Voltage Source Inverter (VSI) Driving an Induction Motor with Open Loop V/f Control Circuit Diagram [11]	31
Figure 19.	AutoCAD Drawing of Rotor and Dimensions	33
Figure 20.	Capacitor Bank Capability Optimization Graph	36
Figure 21.	Software/Hardware Interface Flow Chart	40
Figure 22.	Experiment Circuit Diagram [After 11]	41
Figure 23.	Unmodified Control Model for Laboratory in [11]	43
Figure 24.	Modified Control Model for Regenerative Braking Experiment [After 11] ...	44
Figure 25.	Chipscope GUI Display for Motor Run Configuration [From Chipscope Pro Analyzer, 2010]	46
Figure 26.	Speed Control Component with SR-Flip Flop	47
Figure 27.	SR-Flip Flop Test Model	49
Figure 28.	SR-Flip Flop Wave Output of Test Model	50
Figure 29.	Chipscope GUI Display for Motor Stop Configuration [From Chipscope Pro Analyzer, 2010]	51
Figure 30.	Stop Motor Delay Test Model	51
Figure 31.	Trigger Delay Test Model	52
Figure 32.	Trigger Delay Test Model Wave Output Analysis	53
Figure 33.	Experiment 1 Results	59
Figure 34.	Experiment 2 Results	60
Figure 35.	Experiment 3 Results	61
Figure 36.	Experiment 4 Results	62
Figure 37.	Experiment 5 Results	63
Figure 38.	Experiment 6 Results	64

Figure 39.	Experiment 7 Results	65
Figure 40.	Experiment 8 Results	66
Figure 41.	Experiments 1 and 2 Comparison	68
Figure 42.	Experiments 2 and 3 Comparison	69
Figure 43.	Experiments 3 and 4 Comparison	70
Figure 44.	Experiments 4 and 5 Comparison	71
Figure 45.	Experiments 5 and 6 Comparison	72
Figure 46.	Experiments 6 and 7 Comparison	73
Figure 47.	Experiments 7 and 8 Comparison	74
Figure 48.	Experiment 1 Velocity Difference Analysis	76
Figure 49.	Experiment 2 Velocity Difference Analysis	77
Figure 50.	Experiment 3 Velocity Difference Analysis	78
Figure 51.	Experiment 4 Velocity Difference Analysis	79
Figure 52.	Experiment 5 Velocity Difference Analysis	80
Figure 53.	Experiment 6 Velocity Difference Analysis	81
Figure 54.	Experiment 7 Velocity Difference Analysis	82
Figure 55.	Experiment 8 Velocity Difference Analysis	83
Figure 56.	Experiment 1 Current Behavior Analysis	85
Figure 57.	Experiment 2 Current Behavior Analysis	86
Figure 58.	Experiment 1 Energy Analysis	88
Figure 59.	Experiment 2 Energy Analysis	89

LIST OF TABLES

Table 1.	SR-Flip Flop Truth Table.....	45
Table 2.	Experiment Parameter Table.....	56
Table 3.	Energy Analysis	87

THIS PAGE INTENTIONALLY LEFT BLANK

LIST OF ACRONYMS AND ABBREVIATIONS

AC	Alternating Current
A/D	Analog to Digital
DC	Direct Current
EPA	Environmental Protection Agency
FCCIP	Federal Clean Car Incentive Program
FPGA	Field Programmable Gate Array
NPS	Naval Postgraduate School
RPM	Revolutions per Minute
SVM	Space Vector Modulation
USN	United States Navy
V/f	Voltage by Frequency
VSI	Voltage Source Inverter

THIS PAGE INTENTIONALLY LEFT BLANK

EXECUTIVE SUMMARY

The focus of this thesis was the implementation of computer software and electrical hardware available to Naval Postgraduate School (NPS) students for the modeling and demonstration of regenerative braking using a squirrel cage induction motor. This research is in support of energy recovery and conservation technology development. This thesis first discusses the applicability and benefits of regenerative braking technology to the United States Navy. It also provides the origins and a brief history on regenerative braking. Afterwards, a description is given on the approach used to reach the end product of regenerative braking.

Next, this thesis discusses the theory of induction motors, which includes the equations that mathematically describe their behavior. The effects of phase shift on power and power computation methods are explored through both equations and computer simulations. The methods for solving the power equations were demonstrated using computer simulation software. This demonstration includes a graphical representation of the solutions for illustration purposes with an analysis of the graphs obtained from the simulations. This thesis also covers the methods used to determine key parameters necessary for the experiment's setup. There are demonstrations provided during the model setup of the tests conducted prior to experimentation to ensure the functionality of certain components within the software model.

This thesis also analyzes the data collected during the experiments, which includes:

- A discussion regarding how the various commanded deceleration rates affected power as well as the measured voltage across the capacitor bank of the power inverter
- An analysis observing the difference between the commanded and the actual instantaneous angular velocities
- An overview of current behavior for the first two experiments
- An energy conservation analysis.

The results from the analyses prove the demonstration of regenerative braking. The results also showed by varying the deceleration rates of each experiment, the amount of energy regenerated changed and peak instantaneous power decreased as deceleration rates decreased.

ACKNOWLEDGMENTS

The hardship and journey through academia to achieve this final product, my thesis, would not have become a reality without the help, mentoring, and support of the faculty at NPS, as well as my friends, my mother and mother-in-law, especially my wife. Professor Alexander Julian, by opening his door to me to pursue a field that has yet to be tackled at Naval Postgraduate School gave me a sense of true purpose. Also, I took to heart Professor Julian's side lectures regarding electrical safety. I am greatly appreciative for his diligence in guiding me to a successful thesis.

My mother and mother-in-law understood the seriousness of my distress call as I approached the start of my thesis. Elizabeth, my daughter, entered the world requiring continuous attention on August 30, 2009. Even though my wife and I are extremely happy with our new addition to the family, we were struggling to get the sleep necessary to perform normal daily functions and activities. Both mothers selflessly traveled considerable distances, altering their schedules to help around the house and with our newborn, so I may continue my education and allowing my wife to get some needed rest. Mom, and Mom, you both are my heroes and I am exceedingly lucky to have mothers like you. You have been a real blessing to our lives.

My wife, Clara, probably does not know my gratitude for her patience while enduring me over these last two years. The first few months she started to feel the strain of my frustrations as I struggled through my courses. The majority of the time she listened to my griping, becoming a pin cushion for me so that I could vent when my frustrations got the best of me, and lending me her shoulder where I shed my tears for each homework problem I did not understand. If there were an award for the most devoted, understanding, enduring, compassionate, loving, forgiving, and supporting wife, she would be the most deserving recipient of an award of that magnitude. Clara, I am so grateful for you and your love. I am proud to be your husband!

THIS PAGE INTENTIONALLY LEFT BLANK

I. INTRODUCTION

A. MISSION APPLICABILITY

The United States Navy (USN) can benefit from regenerative braking through its multiple applications within the naval organization. One application could be an energy recovery system to capture energy in descending elevators. This application can be applied aboard aircraft carriers particularly for their massive airlift elevator operations. The primary mechanism that makes a recovery system in elevators possible is gravity, and its action on the mass of the elevator. Instead of using an electrical input to control the descent of the elevator, this descending energy can be harnessed and stored in a battery bank for future use, by employing regenerative braking as a method to control the descending masses, while recovering the kinetic energy. This stored energy increases the electrical distribution system's capacity, by allowing the system to supply energy to meet electrical demands that are greater than the system's electrical generation capacity. These electrical demands might be an electromagnetic catapult system to provide acceleration to aircraft leaving the ships, or rail gun defense systems. This may also give other ship classes, equipped with an elevator system, a greater sense of mission readiness through potentially less fossil fuel consumption. It can also improve the efficiency of the "all electric ship."

Another application for regenerative braking technology, where the USN can realize energy conservation, is within the naval shipyards. Cranes in the shipyards operate almost around the clock hoisting loads in and out of dry-docks, to and from ships, and to and from staging areas. These cranes use fossil fuel driven generators to provide electrical power to electric motors that lift and descend their loads. Cranes can harness the energy from descending masses through an energy recovery system that employs regenerative braking. The energy recovered can be diverted to a battery bank system where the energy is stored, until it can be applied to ascending operations thereby reducing energy demands on the electrical generation system. The crane becomes more

fuel efficient when crane lift demands are supplied by stored electrical energy in place of the fossil fuel converted energy, essentially reducing operating costs to the USN.

The USN can realize a degree of freedom from fossil fueled energy sources by employing more versatile energy recovery systems for Naval Base infrastructure. As with the aircraft carriers' elevator systems, the USN possesses buildings crucial for naval operations that contain passenger elevators. These elevators have the potential of capturing the ascending and descending braking energy through the utilization of recovery systems that incorporate regenerative braking. This conservation will be a contributing factor that lessens building operating expenses to free congressional money for more pertinent mission critical agendas. The USN can benefit from a myriad of applications of regenerative braking technology.

B. THE MOTIVATION FOR REGENERATIVE BRAKING

The world has been placed in a state of crisis searching for reliable energy sources to power motor vehicles beyond fossil fuel due to limited resources. This crisis extends from the Middle East, where there is abundance but not an endless supply of fossil fuels, to the oil dependant lands throughout the globe. For decades, oil prices have been rising, as if there were no end in sight. "The first successful self-propelled road vehicle was a steam automobile invented in 1770 by the French engineer, Nicolas Joseph Cugnot" [1]. Later in the mid-1830s, "Robert Anderson of Scotland invented the first crude electric carriage" that ran on non-rechargeable electric cells [2]; yet the world still became dependent on oil as the automobile technologies evolved to what they are today.

This oil crisis is not a new concept to the world. In the mid-1970s, the world had been challenged with fuel shortages that drastically changed the driving behavior of the United States. The shortages caused the Federal Government to set a national speed limit in efforts of fuel conservation, and forcing the automobile industry to compete for more fuel efficient vehicles. In 1974, the Environmental Protection Agency (EPA) established "an obscured research program called the Federal Clean Car Incentive Program" (FCCIP) [3]. This program encouraged new innovative ideas in the development of reliable alternative energy sources for the automobile industry. The first hybrid vehicle was

invented by Victor Wouk shortly after the FCCIP was implemented. Dr. Wouk had modified a 1972 Buick Skylark into a gasoline-electric vehicle and was able to “cut emissions and save fuel,” but the EPA’s motivation at the time was an all electric vehicle [3].

Today, the automobile industry has been manufacturing hybrid vehicles to supply the public’s demands for more fuel-efficient vehicles due to the higher fuel prices. In efforts to make hybrid vehicles even more fuel efficient energy saving technologies have been implemented. One type of technology for recovering energy in a moving vehicle is regenerative braking. Regenerative braking is also known as rheostatic braking, and more generally known as dynamic braking [4].

Prior to a vehicle slowing down, potential energy is stored in the mass of the vehicle in motion and held at a constant velocity. Once the vehicle brakes, or begins decelerating, the kinetic energy is converted to other types of energy such as heat due to friction or other losses while stopping. Regenerative braking within electric vehicles convert some of the kinetic energy to electrical power in which can charge a battery bank that can later be reused for motor electrical torque. Basically, the motor during normal continuous conditions propels the vehicle forward, and as soon as the brakes are applied the motor, through a circuit control system, becomes a generator slowing the vehicle down and at the same time charging the battery banks. This method of energy conservation helps extend hybrid vehicle range on electrical power and increases its fuel efficiency by reducing the amount of fuel consumption.

C. BRIEF HISTORY OF REGENERATIVE BRAKING

1. The First Steps to Regenerative Braking

“In September 1866, the first self-exciting dynamo—which made electric traction a practical possibility—was invented and constructed by Samuel Alfred Varley” [5]. A self-exciting dynamo is “a dynamo that produces a magnetic field around itself whereby motions of an electrical conductor, carrying magnetic lines of force, generates further current, eventually resulting in a stable external magnetic field” [6]. Essentially, he had

invented compound windings, which are a combination of series and shunt windings [7]. Samuel “Varley did not invent Regenerative Braking” [5], but he did pave the path for electrical engineers who were struggling with the success of the regenerative braking concept.

2. The Inventor of Regenerative Braking

The John-Lundell Company, in 1902, was the first to develop a regenerative braking system that worked, and was able to install the system on one of their tramcars. John Smith Raworth developed a regenerative braking system in his Demi-Cars during the same time period as the John-Lundell Company’s 1902 début. The John-Lundell Company and Raworth struggled for their rights to the invention of regenerative braking. They found themselves losing most of their money to lawyer fees, which drove them to financial instability and forced the John-Lundell Company to withdraw their rights to the invention. This left Raworth as being the inventor of regenerative braking. Within a decade of Raworth’s regenerative braking implementation in his Demi-Cars, the 1911 Rawtenstall accident involving one of Raworth’s Demi-Cars occurred. This gave regenerative braking a bad reputation, causing Raworth to close his company’s doors soon after [5].

Lieutenant Colonel Druitt wrote a report regarding the Rawtenstall accident on November 22, 1911. It stated that regenerative braking was incapable of stopping a tramcar on steep grades, which caused the shunt windings to fuse. This led to the acceleration of the motor, resulting in the two tramcar collision [5]. He further recommended to the Board of Trade that “cars fitted with regenerative control are” [5] not suitable. Following the report, the Board of Trade in the United Kingdom banned regenerative braking in fear of future accidents caused by the technology [5].

It was not until two decades later that regenerative braking became a practical concept. The cost of electrical energy after World War I levied the ban in the United Kingdom that was set by the Board of Trade, and regenerative braking was explored once again. In 1915, the Norfolk and Western Railway Company was able to run “electric locomotives with 3-phase motors off single phase ... using regenerative braking” [5].

Still, motor technology had yet to achieve full potential for a proper demonstration of regenerative braking technology. Due to the war efforts of World War II progression was stagnant until the 1970s fuel crisis [5].

D. OBJECTIVE

The objective of this thesis was to model and demonstrate regenerative braking through the utilization of computer software and hardware available at the Naval Postgraduate School (NPS), Monterey, California. MATLAB's SIMULINK was the environment in which the control model was constructed. Xilinx was the software which produced the computer code language for the Field Programmable Gate Array (FPGA). The FPGA controlled the output of a power inverter capable of Space Vector Modulation (SVM), while Chipscope provided the means to graphically interface the system during the data collection phase of the experiment. It also provided a means to view the data encoded through analog to digital inverters.

E. RESEARCH APPROACH

This thesis encompasses the use of simulation software that interacts with electrical hardware through a graphical interface provided by Chipscope. To understand the capabilities of the software, a validation of continuity between the software and hardware interfaces had to be confirmed. To achieve this validation, a laboratory specifically designed for a course offered by NPS was used. The model within this laboratory was modified to replicate the behavior of a regenerative braking system. After validating continuity and proper operation of the hardware, an understanding of software interactions had to be established. By understanding the manner in which the software interacted with one another, model design and implementation became possible.

Once an acceptable model design was achieved, then multiple experiments were conducted varying the deceleration rate of each experiment. This was to observe the effects of each rate on regenerative braking. The different output waveforms for power, rotor angular velocity, line current, and capacitor bank voltage were measured and analyzed to provide the demonstration of regenerative braking, and to gain some

understanding of the dynamics within the regenerative braking process. A discussion was provided regarding the energy within the system during the experiment.

F. THESIS OVERVIEW AND DESCRIPTION

This thesis contains five chapters. Chapter I contains the applicability of regenerative braking to the USN. This chapter provides a brief history regarding the origins of regenerative braking and it establishes within the reader an understanding of the motivation in the development of regenerative braking technology. Included is the objective and approach of the thesis. Chapter II provides symmetrical induction motor theory and the equations used to mathematically describe the motor's behavior within this experiment. A simulation demonstration was provided to illustrate the three- and two-phase power calculation methods for three-phase circuits, which includes an analysis of the effect phase shift has on power. Chapter III covers the tests involved in model design and the results of these tests. Chapters IV contains the results of the experiments while analyzing the various wave outputs for power, DC bus voltage across the capacitors, current, and an analysis of the difference between commanded and actual angular velocity. A comparison analysis was performed of the waveforms between experiments with deceleration rates that were half or doubled of one another. The energy conservation of the system was discussed and used to provide an explanation for some of the dynamics existing within the system during the regenerative braking process. Chapter V concludes the thesis with the information gained from the research, and provides recommendations for future follow on research in the development regenerative braking.

II. EXPERIMENT PREPARATION

A. THEORY

1. Induction Motor Theory

A squirrel cage induction motor is a common motor that has many applications within our society. A three-phase power supply can be used to create electrical torque to cause the rotor to spin. Sinusoidal voltages are applied to the stator windings, windings usually 120 degrees apart and incased in the motor housing that surrounds the rotor, create a magnetic field that rotates about the rotor at the frequency of the electrical source. Electrical current is induced in conductive bars of the rotor, which are configured similar to a squirrel cage and shorted to one another to allow the current to flow. Initially, the current in the rotor is largest due to the maximum angular velocity difference between the rotor and the stator rotating magnetic field. The current in the rotor creates a magnetic field within the rotor. This magnetic field tries to align itself with the rotating stator magnetic field, which is equal to the induced electromagnetic force (EMF). The rotor's angular velocity increases while aligning these magnetic fields. As the rotor's angular velocity increases, the electrical current induced in the rotor decreases, weakening the magnetic field of the rotor and the resultant EMF. Eventually, the rotor will spin at a frequency less than the stator rotating magnetic field. That frequency difference is dependent upon the load applied to the rotor [8]. The larger the load, the slower the rotor spins, the larger the induced current in the rotor, and the stronger the EMF.

Before pursuing regenerative braking of a squirrel cage induction motor, an understanding of the theory regarding symmetrical, asynchronous induction machines is discussed. The equations used to describe symmetrical, asynchronous induction machines in this chapter are given in [9] and are similar to the equations of a synchronous machine as described in [9] and [12].

The voltage of each phase, v_a , v_b , and v_c for both the stator and the rotor within an induction machine can be expressed by

$$\begin{aligned} \begin{bmatrix} v_{as} \\ v_{bs} \\ v_{cs} \end{bmatrix} &= [r_s] \begin{bmatrix} i_{as} \\ i_{bs} \\ i_{cs} \end{bmatrix} + \rho \begin{bmatrix} \lambda_{as} \\ \lambda_{bs} \\ \lambda_{cs} \end{bmatrix} \\ \begin{bmatrix} v_{ar} \\ v_{br} \\ v_{cr} \end{bmatrix} &= [r_r] \begin{bmatrix} i_{ar} \\ i_{br} \\ i_{cr} \end{bmatrix} + \rho \begin{bmatrix} \lambda_{ar} \\ \lambda_{br} \\ \lambda_{cr} \end{bmatrix} \end{aligned} \quad (1)$$

where

- r_s and r_r are the internal resistances of the stator and the rotor, respectively.
- i_{as} , i_{bs} , and i_{cs} are the currents through the stator windings of each phase.
- i_{ar} , i_{br} , and i_{cr} are the currents through the rotor windings of each phase.
- λ_{as} , λ_{bs} , and λ_{cs} are the flux linkages within the stator.
- λ_{ar} , λ_{br} , and λ_{cr} are the flux linkages within the rotor.
- ρ is the derivative operator used to denote when a derivative is to be taken.

Flux linkages of an induction machine can be represented by

$$\begin{bmatrix} \lambda_{as} \\ \lambda_{bs} \\ \lambda_{cs} \\ \lambda_{ar} \\ \lambda_{br} \\ \lambda_{cr} \end{bmatrix} = \begin{bmatrix} L_s & L_{sr} \\ (L_{sr})^T & L_r \end{bmatrix} \begin{bmatrix} i_{as} \\ i_{bs} \\ i_{cs} \\ i_{ar} \\ i_{br} \\ i_{cr} \end{bmatrix} \quad (2)$$

where

- L_s is the winding inductance of each phase within the stator
- L_{sr} is the mutual inductance of each phase between the stator and the rotor
- L_r is the winding inductance of each phase within the rotor.

These winding inductances can be expressed by

$$L_s = \begin{bmatrix} L_{ls} + L_{ms} & -\frac{1}{2}L_{ms} & -\frac{1}{2}L_{ms} \\ -\frac{1}{2}L_{ms} & L_{ls} + L_{ms} & -\frac{1}{2}L_{ms} \\ -\frac{1}{2}L_{ms} & -\frac{1}{2}L_{ms} & L_{ls} + L_{ms} \end{bmatrix} \quad (3)$$

$$L_r = \begin{bmatrix} L_{lr} + L_{mr} & -\frac{1}{2}L_{mr} & -\frac{1}{2}L_{mr} \\ -\frac{1}{2}L_{mr} & L_{lr} + L_{mr} & -\frac{1}{2}L_{mr} \\ -\frac{1}{2}L_{mr} & -\frac{1}{2}L_{mr} & L_{lr} + L_{mr} \end{bmatrix} \quad (4)$$

$$L_{sr} = L_{sr} \begin{bmatrix} \cos \theta_r & \cos\left(\theta_r + \frac{2\pi}{3}\right) & \cos\left(\theta_r - \frac{2\pi}{3}\right) \\ \cos\left(\theta_r - \frac{2\pi}{3}\right) & \cos \theta_r & \cos\left(\theta_r + \frac{2\pi}{3}\right) \\ \cos\left(\theta_r + \frac{2\pi}{3}\right) & \cos\left(\theta_r - \frac{2\pi}{3}\right) & \cos \theta_r \end{bmatrix} \quad (5)$$

where

- L_{ls} is the leakage inductance of the stator
- L_{ms} is the magnetic inductance of the stator
- L_{lr} is the leakage inductance of the rotor
- L_{mr} is the magnetic inductance of the rotor
- θ_r is the angle of the rotor with respect to the stator as shown in Figure 1.

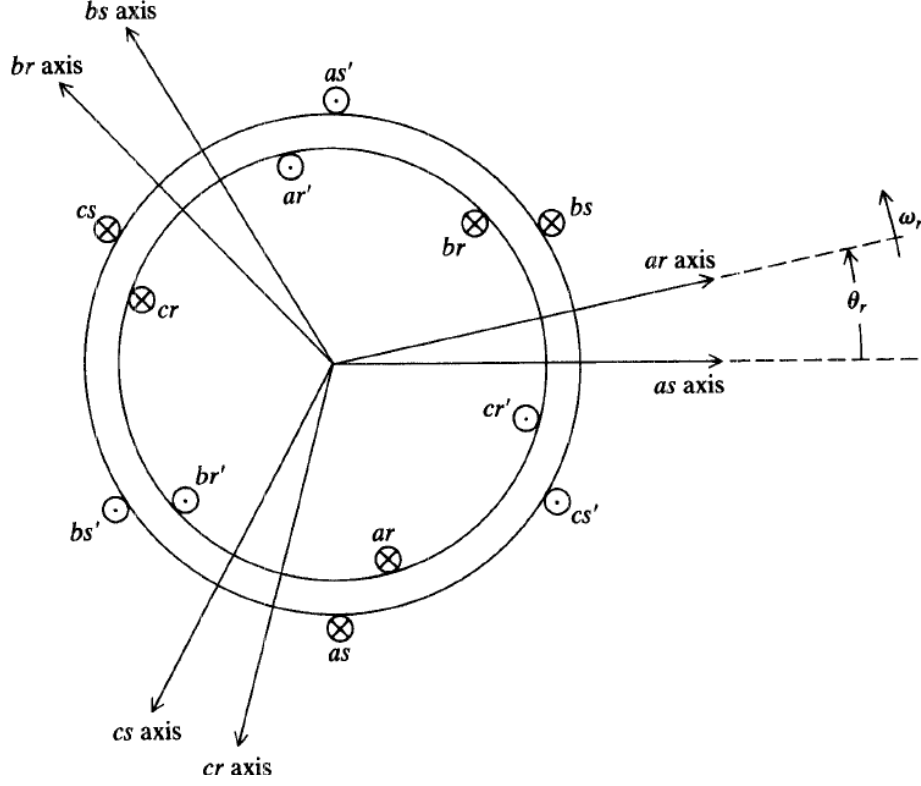


Figure 1. Two-pole, 3-phase, Wye-Connected Symmetrical Induction Machine [9]

By substituting Equations (3), (4), and (5) into Equation (2), the flux linkage equation essentially becomes

$$\begin{bmatrix} \lambda_{as} \\ \lambda_{bs} \\ \lambda_{cs} \\ \lambda_{ar} \\ \lambda_{br} \\ \lambda_{cr} \end{bmatrix} = \begin{bmatrix} L_{ls} + L_{ms} & -\frac{1}{2}L_{ms} & -\frac{1}{2}L_{ms} & L_{sr} \cos \theta_r & L_{sr} \cos(\theta_r + \frac{2\pi}{3}) & L_{sr} \cos(\theta_r - \frac{2\pi}{3}) \\ -\frac{1}{2}L_{ms} & L_{ls} + L_{ms} & -\frac{1}{2}L_{ms} & L_{sr} \cos(\theta_r - \frac{2\pi}{3}) & L_{sr} \cos \theta_r & L_{sr} \cos(\theta_r + \frac{2\pi}{3}) \\ -\frac{1}{2}L_{ms} & -\frac{1}{2}L_{ms} & L_{ls} + L_{ms} & L_{sr} \cos(\theta_r + \frac{2\pi}{3}) & L_{sr} \cos(\theta_r - \frac{2\pi}{3}) & L_{sr} \cos \theta_r \\ L_{sr} \cos \theta_r & L_{sr} \cos(\theta_r - \frac{2\pi}{3}) & L_{sr} \cos(\theta_r + \frac{2\pi}{3}) & L_{lr} + L_{mr} & -\frac{1}{2}L_{mr} & -\frac{1}{2}L_{mr} \\ L_{sr} \cos(\theta_r + \frac{2\pi}{3}) & L_{sr} \cos \theta_r & L_{sr} \cos(\theta_r - \frac{2\pi}{3}) & -\frac{1}{2}L_{mr} & L_{lr} + L_{mr} & -\frac{1}{2}L_{mr} \\ L_{sr} \cos(\theta_r - \frac{2\pi}{3}) & L_{sr} \cos(\theta_r + \frac{2\pi}{3}) & L_{sr} \cos \theta_r & -\frac{1}{2}L_{mr} & -\frac{1}{2}L_{mr} & L_{lr} + L_{mr} \end{bmatrix} \begin{bmatrix} i_{as} \\ i_{bs} \\ i_{cs} \\ i_{ar} \\ i_{br} \\ i_{cr} \end{bmatrix} \quad (6)$$

When determining an equivalent circuit of the motor, a convenient and common method is to describe the circuit by referencing the rotor in terms of the stator. This is accomplished by creating a turns ratio between the number of windings of the rotor to the number of windings of the stator.

Where

- N_s is the number of windings in the stator
- N_r is the number of windings in the rotor.

By combining these winding numbers into a ratio, the rotor part of the circuit is then described in terms of the stator while using prime notation. The currents, voltages, and flux linkages will then become

$$\begin{bmatrix} i'_{ar} \\ i'_{br} \\ i'_{cr} \end{bmatrix} = \frac{N_r}{N_s} \begin{bmatrix} i_{ar} \\ i_{br} \\ i_{cr} \end{bmatrix} \quad (7)$$

$$\begin{bmatrix} v'_{ar} \\ v'_{br} \\ v'_{cr} \end{bmatrix} = \frac{N_s}{N_r} \begin{bmatrix} v_{ar} \\ v_{br} \\ v_{cr} \end{bmatrix} \quad (8)$$

$$\begin{bmatrix} \lambda'_{ar} \\ \lambda'_{br} \\ \lambda'_{cr} \end{bmatrix} = \frac{N_s}{N_r} \begin{bmatrix} \lambda_{ar} \\ \lambda_{br} \\ \lambda_{cr} \end{bmatrix} \quad (9)$$

$$r'_r = \left(\frac{N_s}{N_r} \right)^2 r_r \quad (10)$$

By applying the turns ratio to the inductances of the rotor, the inductances can then also transformed in terms of the stator as shown in Equations (11) through (13)

$$L_{ms} = \frac{N_s}{N_r} L_{sr} \quad (11)$$

$$L'_r = \left(\frac{N_s}{N_r} \right)^2 L_r \quad (12)$$

$$L'_{lr} = \left(\frac{N_s}{N_r} \right)^2 L_{lr} \quad (13)$$

The mutual and magnetic inductances can further be defined using the turns ratio as in Equations (14) and (15)

$$L'_{sr} = \frac{N_s}{N_r} L_{sr} \quad (14)$$

$$L'_{mr} = \left(\frac{N_r}{N_s} \right)^2 L_{ms} \quad (15)$$

transforming the rotor total inductance into Equation (16)

$$L'_r = \begin{bmatrix} L'_{lr} + L_{ms} & -\frac{1}{2} L_{ms} & -\frac{1}{2} L_{ms} \\ -\frac{1}{2} L_{ms} & L'_{lr} + L_{ms} & -\frac{1}{2} L_{ms} \\ -\frac{1}{2} L_{ms} & -\frac{1}{2} L_{ms} & L'_{lr} + L_{ms} \end{bmatrix} \quad (16)$$

and also transforming the mutual inductance of the rotor into Equation (17)

$$L'_{sr} = L_{ms} \begin{bmatrix} \cos \theta_r & \cos(\theta_r + \frac{2\pi}{3}) & \cos(\theta_r - \frac{2\pi}{3}) \\ \cos(\theta_r - \frac{2\pi}{3}) & \cos \theta_r & \cos(\theta_r + \frac{2\pi}{3}) \\ \cos(\theta_r + \frac{2\pi}{3}) & \cos(\theta_r - \frac{2\pi}{3}) & \cos \theta_r \end{bmatrix} \quad (17)$$

The voltage and flux linkage Equations (1) and (2) can now be described completely in terms of the stator as shown in Equations (18) and (19).

$$\begin{bmatrix} v_{as} \\ v_{bs} \\ v_{cs} \end{bmatrix} = [r_s] \begin{bmatrix} i_{as} \\ i_{bs} \\ i_{cs} \end{bmatrix} + \rho [L_s] \begin{bmatrix} i_{as} \\ i_{bs} \\ i_{cs} \end{bmatrix} + \rho [L'_{sr}] \begin{bmatrix} i'_{ar} \\ i'_{br} \\ i'_{cr} \end{bmatrix} \quad (18)$$

$$\begin{bmatrix} v'_{ar} \\ v'_{br} \\ v'_{cr} \end{bmatrix} = [L'_{sr}]^T \begin{bmatrix} i_{as} \\ i_{bs} \\ i_{cs} \end{bmatrix} + [r'_r] \begin{bmatrix} i'_{ar} \\ i'_{br} \\ i'_{cr} \end{bmatrix} + \rho [L'_r] \begin{bmatrix} i'_{ar} \\ i'_{br} \\ i'_{cr} \end{bmatrix} \quad (19)$$

$$\begin{bmatrix} \lambda_{as} \\ \lambda_{bs} \\ \lambda_{cs} \\ \lambda'_{ar} \\ \lambda'_{br} \\ \lambda'_{cr} \end{bmatrix} = \begin{bmatrix} L_s & L'_{sr} \\ (L'_{sr})^T & L'_r \end{bmatrix} \begin{bmatrix} i_{as} \\ i_{bs} \\ i_{cs} \\ i'_{ar} \\ i'_{br} \\ i'_{cr} \end{bmatrix}$$

By substituting Equations (3), (16), and (17), Equation (19) now can be expanded and expressed in terms of the stator as shown in Equation (20).

$$\begin{bmatrix} \lambda_{as} \\ \lambda_{bs} \\ \lambda_{cs} \\ \lambda'_{ar} \\ \lambda'_{br} \\ \lambda'_{cr} \end{bmatrix} = \begin{bmatrix} L_{ls} + L_{ms} & -\frac{1}{2}L_{ms} & -\frac{1}{2}L_{ms} & L_{ms} \cos \theta_r & L_{ms} \cos(\theta_r + \frac{2\pi}{3}) & L_{ms} \cos(\theta_r - \frac{2\pi}{3}) \\ -\frac{1}{2}L_{ms} & L_{ls} + L_{ms} & -\frac{1}{2}L_{ms} & L_{ms} \cos(\theta_r - \frac{2\pi}{3}) & L_{ms} \cos \theta_r & L_{ms} \cos(\theta_r + \frac{2\pi}{3}) \\ -\frac{1}{2}L_{ms} & -\frac{1}{2}L_{ms} & L_{ls} + L_{ms} & L_{ms} \cos(\theta_r + \frac{2\pi}{3}) & L_{ms} \cos(\theta_r - \frac{2\pi}{3}) & L_{ms} \cos \theta_r \\ L_{ms} \cos \theta_r & L_{ms} \cos(\theta_r - \frac{2\pi}{3}) & L_{ms} \cos(\theta_r + \frac{2\pi}{3}) & L'_{lr} + L_{ms} & -\frac{1}{2}L_{ms} & -\frac{1}{2}L_{ms} \\ L_{ms} \cos(\theta_r + \frac{2\pi}{3}) & L_{ms} \cos \theta_r & L_{ms} \cos(\theta_r - \frac{2\pi}{3}) & -\frac{1}{2}L_{ms} & L'_{lr} + L_{ms} & -\frac{1}{2}L_{ms} \\ L_{ms} \cos(\theta_r - \frac{2\pi}{3}) & L_{ms} \cos(\theta_r + \frac{2\pi}{3}) & L_{ms} \cos \theta_r & -\frac{1}{2}L_{ms} & -\frac{1}{2}L_{ms} & L'_{lr} + L_{ms} \end{bmatrix} \begin{bmatrix} i_{as} \\ i_{bs} \\ i_{cs} \\ i'_{ar} \\ i'_{br} \\ i'_{cr} \end{bmatrix} \quad (20)$$

By inverting the turns ratio and applying the ratio to the stator variables, the equivalent circuit is similarly described in terms of the rotor.

The energy stored in the coupling mechanical and electrical fields is related as

$$W_f = \frac{1}{2} \begin{bmatrix} i_{as} \\ i_{bs} \\ i_{cs} \end{bmatrix}^T (L_s - L_{ls} \mathbf{I}) \begin{bmatrix} i_{as} \\ i_{bs} \\ i_{cs} \end{bmatrix} + \begin{bmatrix} i_{as} \\ i_{bs} \\ i_{cs} \end{bmatrix}^T L'_{sr} \begin{bmatrix} i'_{ar} \\ i'_{br} \\ i'_{cr} \end{bmatrix} + \frac{1}{2} \begin{bmatrix} i'_{ar} \\ i'_{br} \\ i'_{cr} \end{bmatrix}^T (L'_r - L'_{lr} \mathbf{I}) \begin{bmatrix} i'_{ar} \\ i'_{br} \\ i'_{cr} \end{bmatrix} \quad (21)$$

where

- W_f is the field energy
- \mathbf{I} is the identity matrix.

Equation (22) associates the change in mechanical energy to the change in rotor position caused by a given electrical torque, T_e

$$dW_m = -T_e d\theta_{rm} \quad (22)$$

where

- W_m is the mechanical energy
- θ_{rm} is the change in rotor position.

Taking into account the number of poles in the machine, the electrical angular displacement is determined using Equation (23).

$$\theta_r = \left(\frac{P}{2} \right) \theta_{rm} \quad (23)$$

Solving for T_e in Equation (22) and taking the partial derivative of mechanical energy with respect to rotor position, electrical torque can be expressed as a function of current and rotor position as shown in Equation (24).

$$T_e(i_j, \theta_r) = \left(\frac{P}{2} \right) \frac{\partial W_m(i_j, \theta_r)}{\partial \theta_r} \quad (24)$$

Since L_s and L_r' are independent of θ_r and substituting W_f , then electrical torque can be expressed as:

$$T_e = \left(\frac{P}{2} \right) \begin{bmatrix} i_{as} \\ i_{bs} \\ i_{cs} \end{bmatrix}^T \frac{\partial}{\partial \theta_r} [L'_{sr}] \begin{bmatrix} i'_{ar} \\ i'_{br} \\ i'_{cr} \end{bmatrix} \quad (25)$$

The torque and rotor speed are related as shown in Equation (26).

$$T_e = J \left(\frac{2}{P} \right) \frac{\partial}{\partial \theta_r} p \omega_r + T_L \quad (26)$$

where

- ω_r is the angular velocity of the rotor
- J is the moment of inertia of the rotor
- T_L is the torque induced on the shaft from the load.

Reference [9] discusses a means to decrease the complexity of the voltage equations. By changing the reference frame to an arbitrary reference frame, the complexity of the equations are significantly reduced. Equation (27) is the general form of changing reference frames

$$\begin{bmatrix} f_{qs}^x \\ f_{ds}^x \\ f_{0s}^x \end{bmatrix} = K_s^x \begin{bmatrix} f_{as} \\ f_{bs} \\ f_{cs} \end{bmatrix} \quad (27)$$

$$\begin{bmatrix} f_{qr}'^x \\ f_{dr}'^x \\ f_{0r}'^x \end{bmatrix} = K_r^x \begin{bmatrix} f_{ar}' \\ f_{br}' \\ f_{cr}' \end{bmatrix}$$

where

- f_s^x and $f_r'^x$ can represent any variable of the stator and rotor respectively
- K_s and K_r are the reference frame conversion factor matrices as shown in Equations (28) and (29).

$$K_s = \frac{2}{3} \begin{bmatrix} \cos \theta & \cos\left(\theta - \frac{2\pi}{3}\right) & \cos\left(\theta + \frac{2\pi}{3}\right) \\ \sin \theta & \sin\left(\theta - \frac{2\pi}{3}\right) & \sin\left(\theta + \frac{2\pi}{3}\right) \\ \frac{1}{2} & \frac{1}{2} & \frac{1}{2} \end{bmatrix} \quad (28)$$

$$K_r = \frac{2}{3} \begin{bmatrix} \cos \beta & \cos\left(\beta - \frac{2\pi}{3}\right) & \cos\left(\beta + \frac{2\pi}{3}\right) \\ \sin \beta & \sin\left(\beta - \frac{2\pi}{3}\right) & \sin\left(\beta + \frac{2\pi}{3}\right) \\ \frac{1}{2} & \frac{1}{2} & \frac{1}{2} \end{bmatrix} \quad (29)$$

In Figure 2, β is defined by $\beta = \theta - \theta_r$.

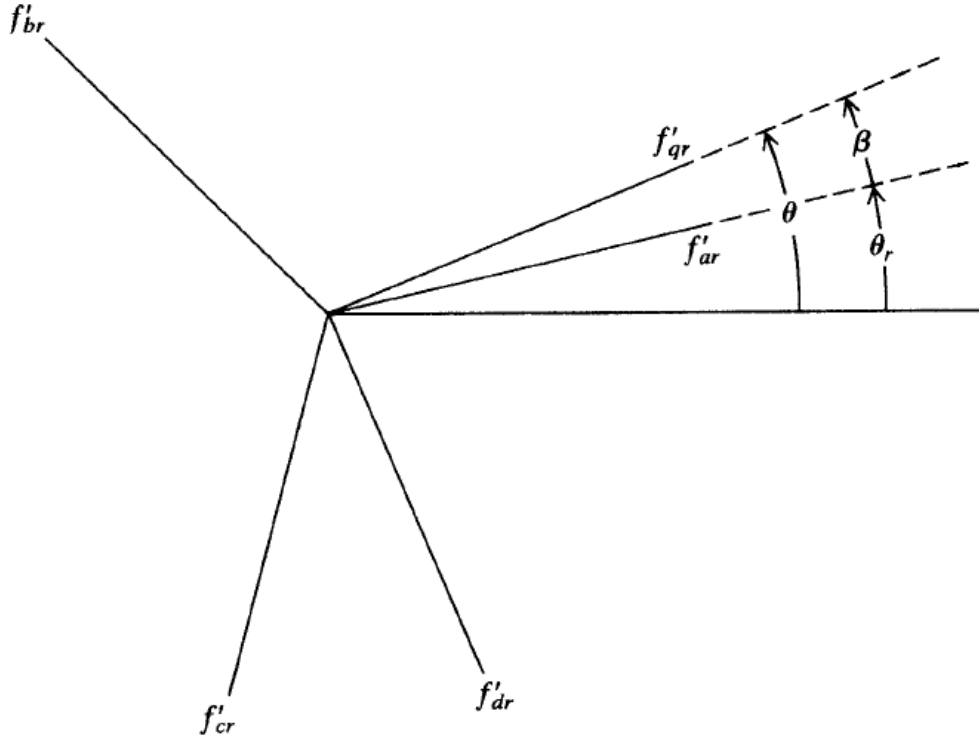


Figure 2. Transformation for Rotating Circuits Portrayed by Trigonometric Relationships (After [9])

To transfer from one reference frame to another, θ is the component used in the transformation of variables in Equations (28) and (29). The x term in Equation (27) specifies the reference frame to which the variable had been transformed. By applying the transformations to Equations (18) and (20) to an arbitrary reference frame, the resultant voltage and flux linkages equations are shown in Equations (30) and (31).

$$\begin{aligned}
v_{qs} &= r_s i_{qs} + \omega \lambda_{ds} + \rho \lambda_{qs} \\
v_{ds} &= r_s i_{ds} - \omega \lambda_{qs} + \rho \lambda_{ds} \\
v_{0s} &= r_s i_{0s} + \rho \lambda'_{0r} \\
v'_{qr} &= r'_r i'_{qr} + (\omega - \omega_r) \lambda'_{qr} + \rho \lambda'_{qr} \\
v'_{dr} &= r'_r i'_{dr} - (\omega - \omega_r) \lambda'_{dr} + \rho \lambda'_{dr} \\
v'_{0r} &= r'_r i'_{0r} + \rho \lambda'_{0r}
\end{aligned} \tag{30}$$

$$\begin{aligned}
\lambda_{qs} &= L_{ls} i_{qs} + L_{ms} (i_{qs} + i'_{qr}) \\
\lambda_{ds} &= L_{ls} i_{ds} + L_{ms} (i_{ds} + i'_{dr}) \\
\lambda_{0s} &= L_{ls} i_{0s} \\
\lambda'_{qr} &= L_{lr} i_{qr} + L_{ms} (i_{qs} + i'_{qr}) \\
\lambda'_{dr} &= L_{lr} i_{dr} + L_{ms} (i_{ds} + i'_{dr}) \\
\lambda'_{0r} &= L_{lr} i'_{0r}
\end{aligned} \tag{31}$$

where

- ω is the angular velocity of the arbitrary reference frame
- ω_b is the base electrical angular velocity
- ω_r is the rotor angular velocity.

Equation (30) can be further manipulated by defining ψ in Equation (32) with units of flux linkage per second to produce Equation (33).

$$\psi = \lambda \omega_b \tag{32}$$

$$\begin{aligned}
v_{qs} &= r_s i_{qs} + \frac{\omega}{\omega_b} \psi_{ds} + \frac{\rho}{\omega_b} \psi_{qs} \\
v_{ds} &= r_s i_{ds} - \frac{\omega}{\omega_b} \psi_{qs} + \frac{\rho}{\omega_b} \psi_{ds} \\
v_{0s} &= r_s i_{0s} + \frac{\rho}{\omega_b} \psi_{0s} \\
v'_{qr} &= r'_r i'_{qr} + \frac{(\omega - \omega_r)}{\omega_b} \psi'_{dr} + \frac{\rho}{\omega_b} \psi'_{qr} \\
v'_{dr} &= r'_r i'_{dr} - \frac{(\omega - \omega_r)}{\omega_b} \psi'_{qr} + \frac{\rho}{\omega_b} \psi'_{dr} \\
v'_{0r} &= r'_r i'_{0r} + \frac{\rho}{\omega_b} \psi'_{0r}
\end{aligned} \tag{33}$$

and the flux linkages per second now become Equation (34).

$$\begin{aligned}
\psi_{qs} &= X_{ls} i_{qs} + X_{ms} (i_{qs} + i'_{qr}) \\
\psi_{ds} &= X_{ls} i_{ds} + X_{ms} (i_{ds} + i'_{dr}) \\
\psi_{0s} &= X_{ls} i_{0s} \\
\psi'_{qr} &= X'_{lr} i_{qr} + X_{ms} (i_{qs} + i'_{qr}) \\
\psi'_{dr} &= X'_{lr} i_{dr} + X_{ms} (i_{ds} + i'_{dr}) \\
\psi'_{0r} &= X'_{lr} i'_{0r}
\end{aligned} \tag{34}$$

2. Demonstration of Three and Two-Phase Power Calculations

There are multiple methods to calculate power for a three-phase wye-connected circuit. The method used will determine the number of measurements taken during the experiment. In this section, two methods will be analyzed to show the validity of both methods. One of these methods to be analyzed is the three-phase voltage/current power calculation, and the other method is the two-phase voltage / two-phase current method. A laboratory in [10] was specifically designed and created for a course offered at Naval Postgraduate School (NPS), Monterey, California and was used to provide background information for calculating power for both methods. The Simulink model and MATLAB code used to generate Figures 3 through 12 are contained in Appendix A.

In a direct current (DC) circuit, steady state power is determined by multiplying the voltage of the circuit by the current of the circuit shown in Equation (35).

$$P = VI \quad (35)$$

Where

- V is voltage
- I is current
- P is power.

For sinusoidal voltages and currents, or alternating current (AC) circuits, steady state as well as instantaneous power is determined in the same manner as the DC circuit with the exception of the phase difference between current and voltage as seen in Equation (36).

$$P = vi \cos(\theta(t)) \quad (36)$$

Where

- v is the AC voltage amplitude
- i is the AC current amplitude
- P is the instantaneous real power (Watts)
- $\theta(t)$ is the phase difference between the voltage and current with respect to time.

Three cases exist relating the phase angle between current and voltage. One case is the condition when the current leads the voltage as shown in Figure 3. In this case, current leads voltage by a 45 degree phase shift. The second case is when the phase shift is equal to zero as shown in Figure 4. In this case, the graph only shows one sinusoid. This is due to both voltage and current being exactly identical to one another. The third condition is when the current lags or follows voltage as shown in Figure 5.

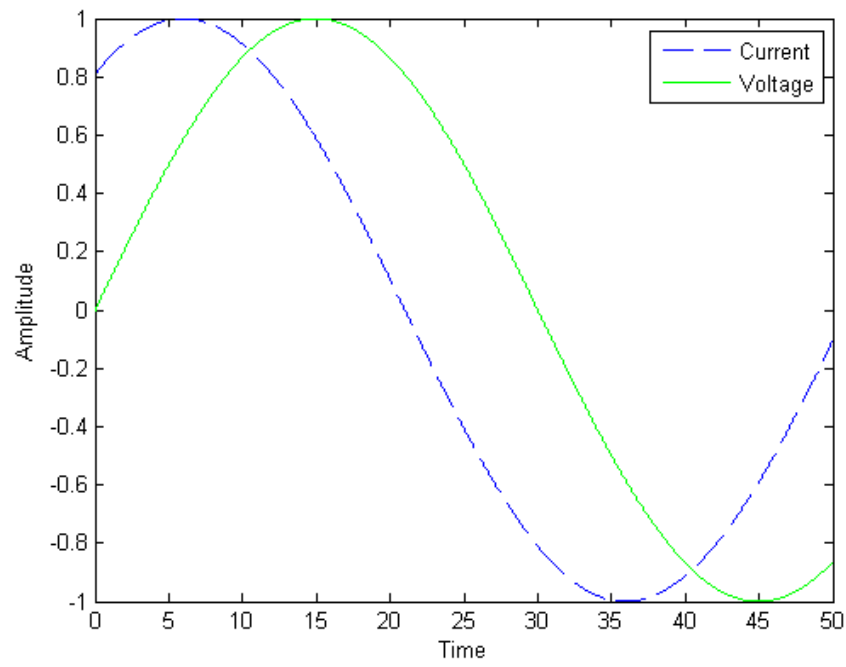


Figure 3. Leading Phase Shift Condition

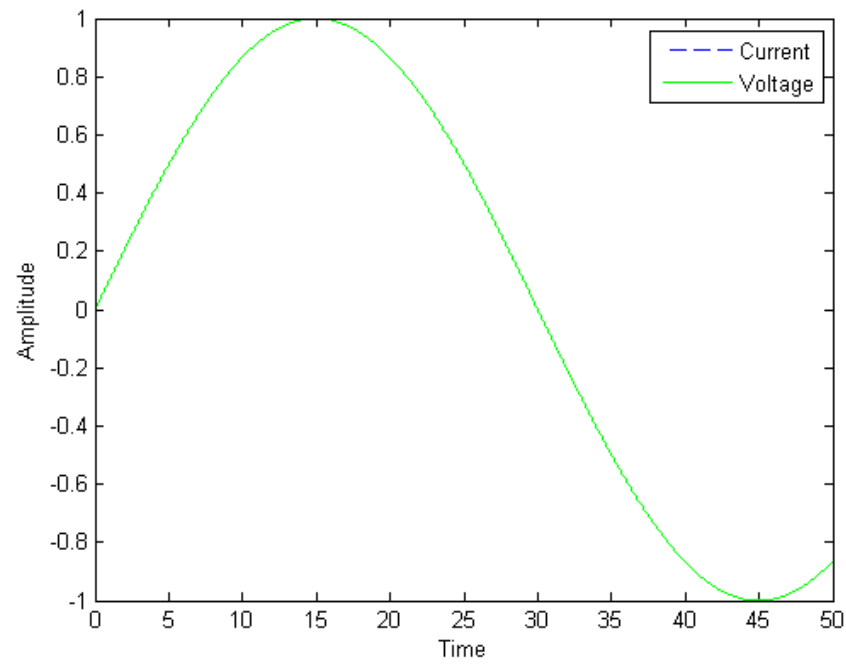


Figure 4. Zero Phase Shift Condition

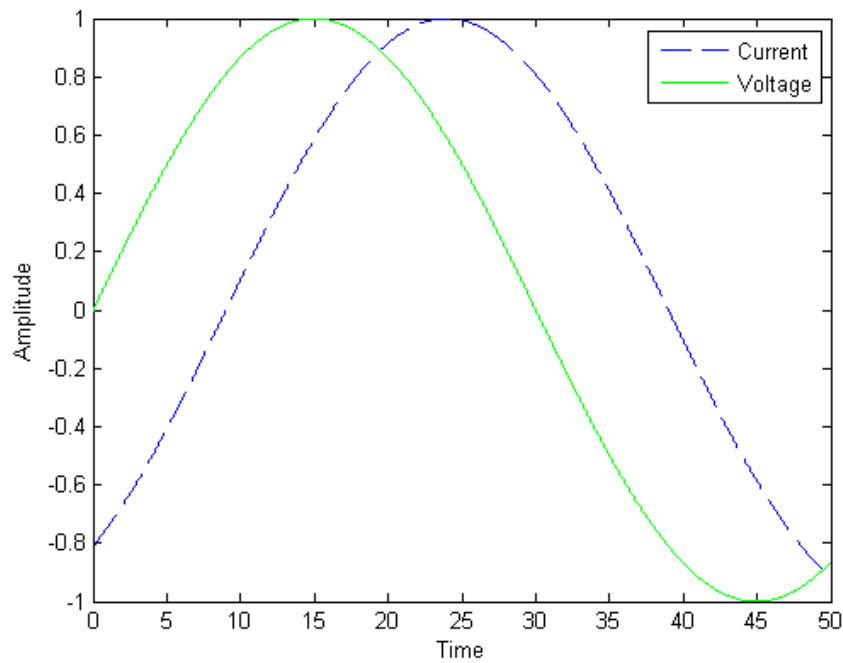


Figure 5. Lagging Phase Shift Condition

Figures 6 through 10 demonstrate the effects of phase difference between voltage and current on power as the phase difference goes from forty-five degrees to zero degrees. Going from Figure 6 to Figure 10, instantaneous power approaches a maximum value as voltage and current align themselves with a zero degree phase shift. Instantaneous power is zero when voltage and current phases are ninety degrees from each other.

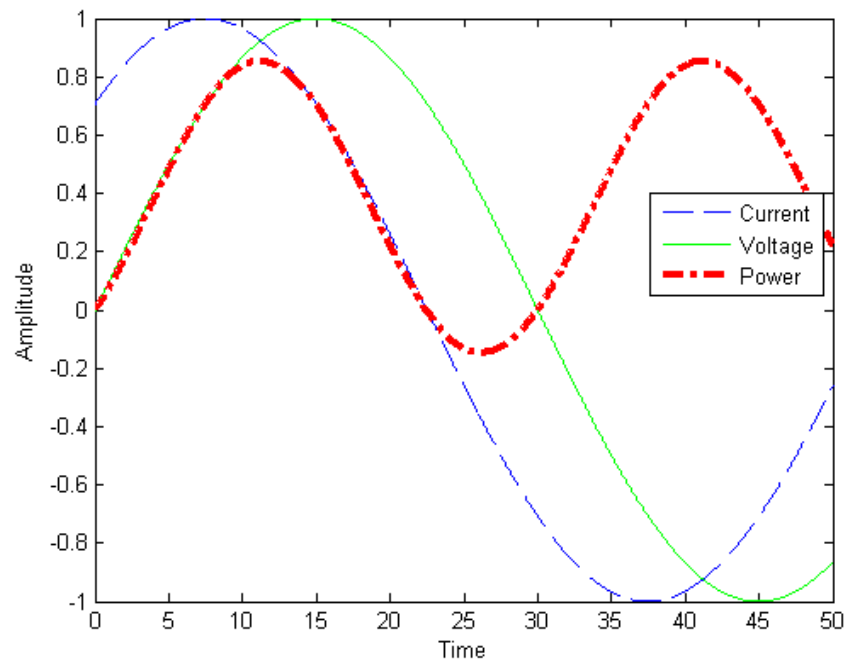


Figure 6. Current Leads Voltage 45 degrees

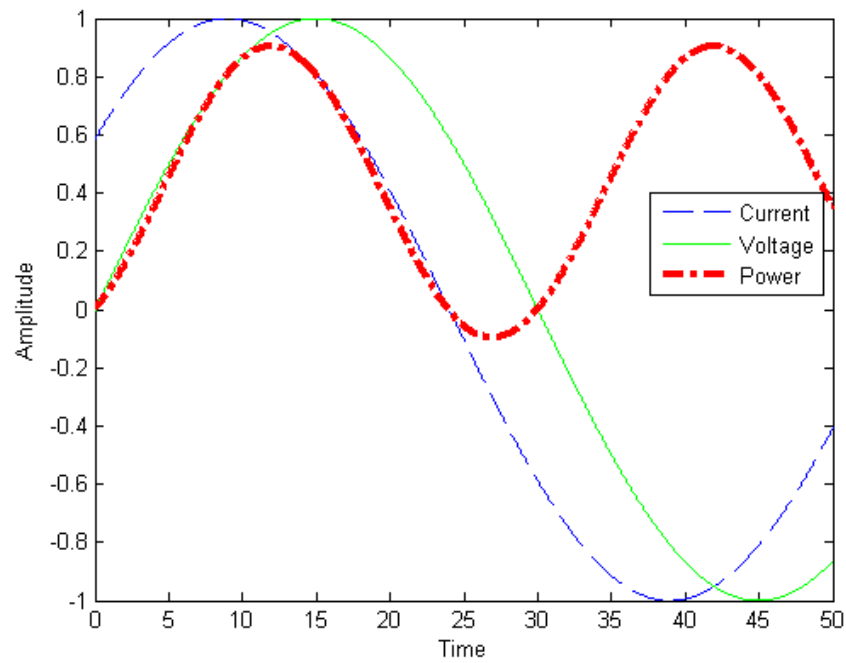


Figure 7. Current Leads Voltage 36 degrees

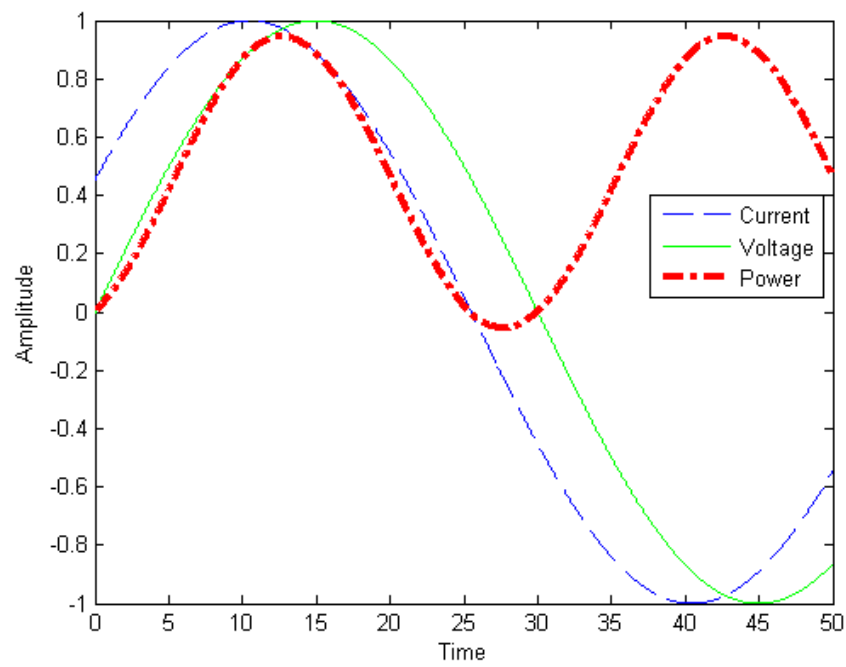


Figure 8. Current Leads Voltage 27 degrees

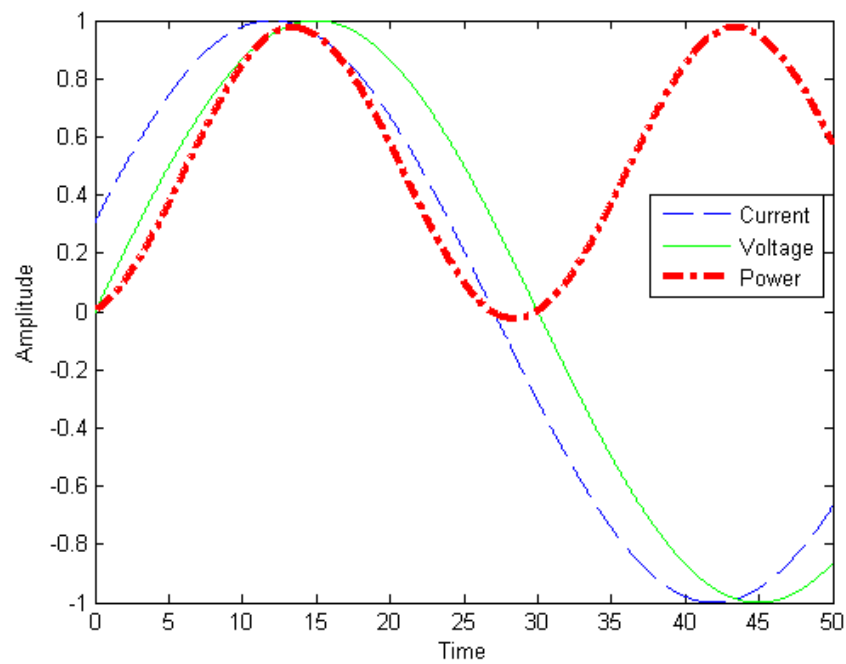


Figure 9. Current Leads Voltage 18 degrees

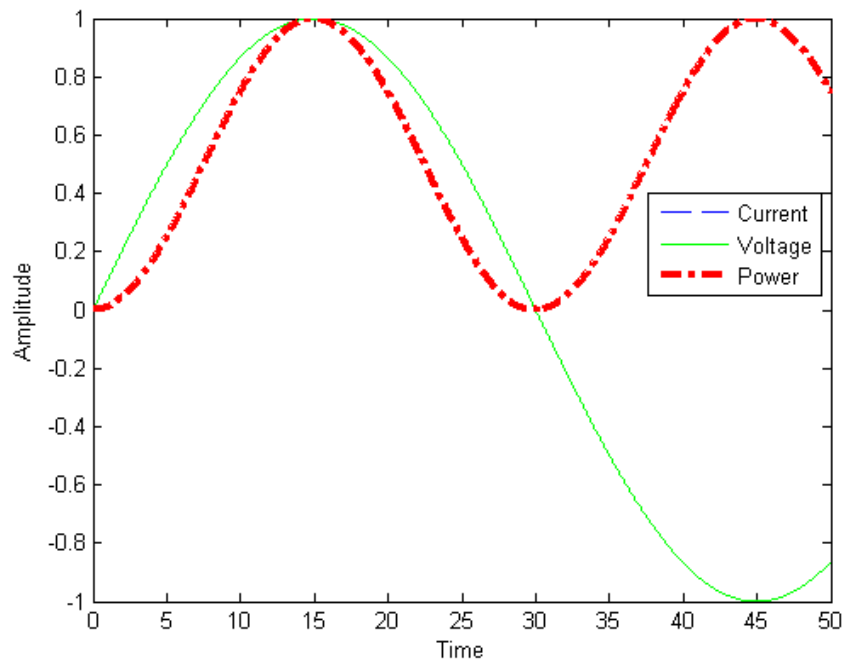


Figure 10. Current Voltage Phases are Equal (Power at Maximum)

To further elaborate the effects of phase shift on power, Figure 11 is a Three-Dimensional Optimization graph that illustrates power on the Z-axis. The X and Y axes both represent the change in angular position relative to one another. It is apparent when phase shift is equal to zero, the power is at its maximum, and the opposite holds true when phase shift is \pm ninety degrees power is at its minimum.

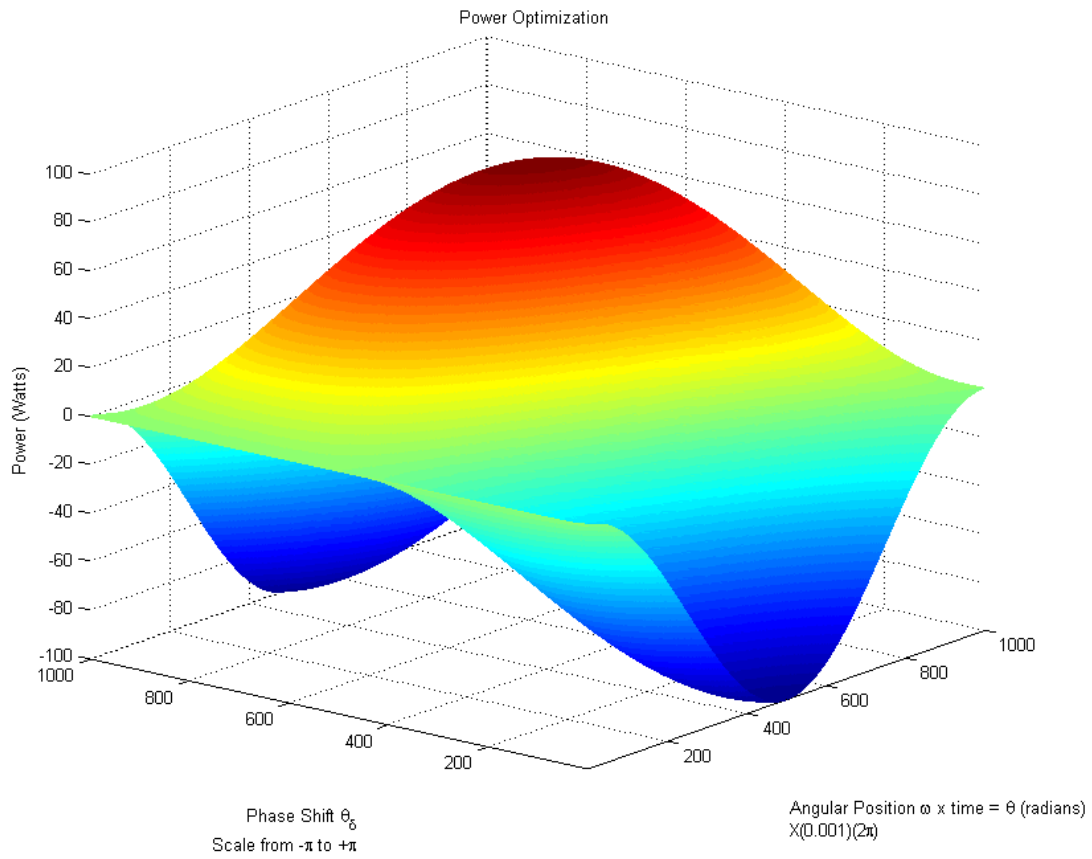


Figure 11. Three-Dimensional Power Optimization Graph

The power of a three-phase floating wye-connected circuit is calculated similar to the single phase circuit, except the calculations must take into account the 120 degrees between each phase and the phase difference between current and voltage. In a wye-connected circuit, as shown in Figure 12, the phases are assumed to be balanced; therefore, the line currents and voltages are equal in amplitude.

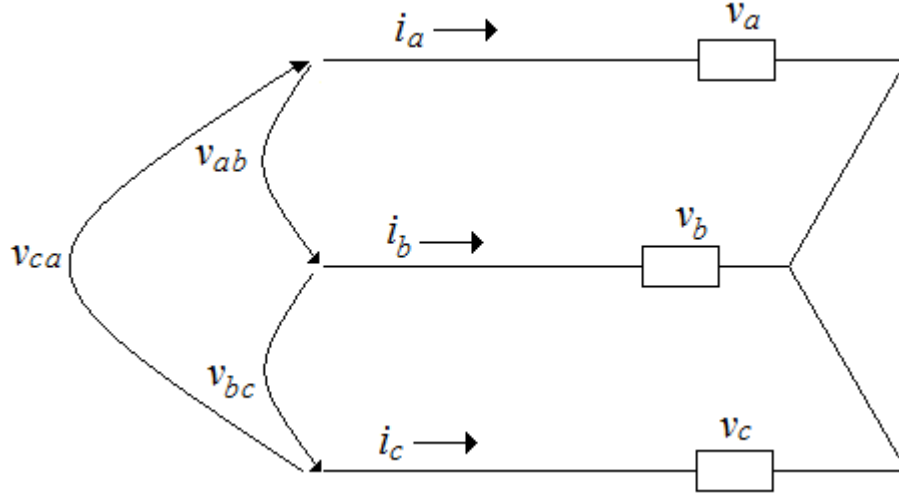


Figure 12. Wye-Connected Circuit

Since the wye-connected circuit is assumed to be balanced, the line-to-line voltages, v_{ab} , v_{bc} , and v_{ca} , which are voltages measured between lines, have the same magnitudes. The line currents, i_{ab} , i_{bc} , and i_{ca} , also have the same magnitudes. The coil voltages of the motor, v_a , v_b , and v_c are all proportional to line voltages as shown in Equation (37),

$$\begin{aligned} v_a &= \frac{v_{ab}}{\sqrt{3}} \\ v_b &= \frac{v_{bc}}{\sqrt{3}} \\ v_c &= \frac{v_{ca}}{\sqrt{3}} \end{aligned} \tag{37}$$

and power is equal to the coil voltages multiplied by the coil currents as shown in Equation (38) [10].

$$P = v_a i_a + v_b i_b + v_c i_c \tag{38}$$

Since the line currents equal the coil currents, then power is equal to the coil voltages multiplied by the line currents. Because the load is wye-connected, the current summation at any particular time is equal to zero as shown in Equation (39).

$$i_a + i_b + i_c = 0 \tag{39}$$

By solving for i_b in Equation (39), the resultant is Equation (40).

$$i_b = -(i_a + i_c) \quad (40)$$

Substituting Equation (40) for Equation (38), the power of a three-phase circuit can now be calculated in terms of two line-to-line voltages and two line currents as shown in Equation (41).

$$\begin{aligned} P &= v_a i_a + v_b (-i_a - i_c) + v_c i_c \\ P &= v_a i_a - v_b i_a + v_c i_c - v_b i_c \\ P &= i_a (v_a - v_b) + i_c (v_c - v_b) \\ P &= i_a v_{ab} + i_c v_{cb} \end{aligned} \quad (41)$$

The model in Figure 13, was created in Simulink to graphically demonstrate the three-phase power calculation is equal to the two-phase method. In this model, the current and voltage phases were all set equal to one another to maximize power while their amplitudes were all set to 1. Figure 14 contains the voltage and current signal inputs to the three-phase power calculator. Figure 15 illustrates the location where the signal was extracted from a wye-connected circuit. Figure 16 contains the voltage and current signal inputs to the two-phase power calculator. Figure 17 illustrates the location where each signal was extracted from a wye-connected circuit.

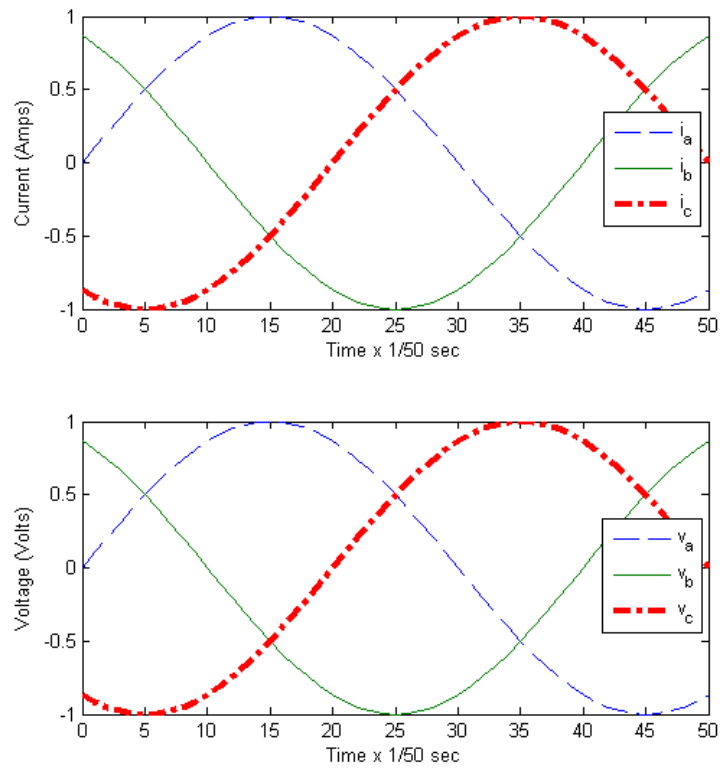


Figure 14. Voltage and Current Input Signals for Three-Phase Calculator

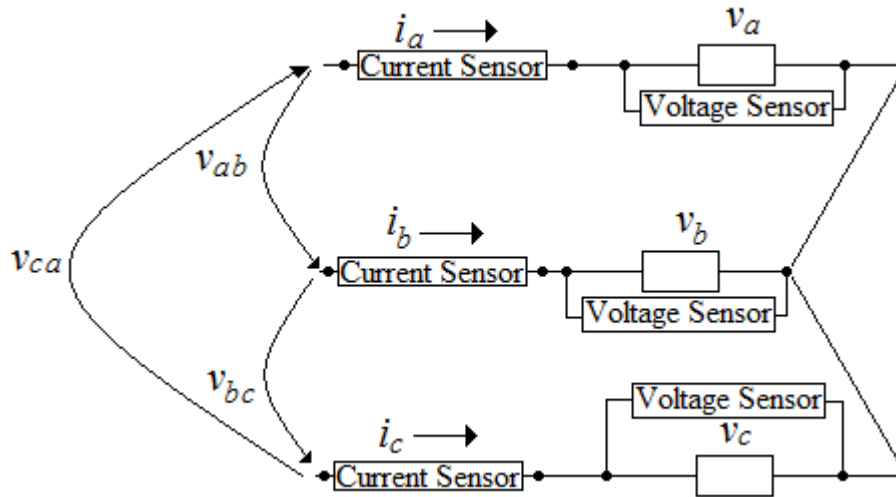


Figure 15. Sensor Connections for Three-Phase Power Calculator

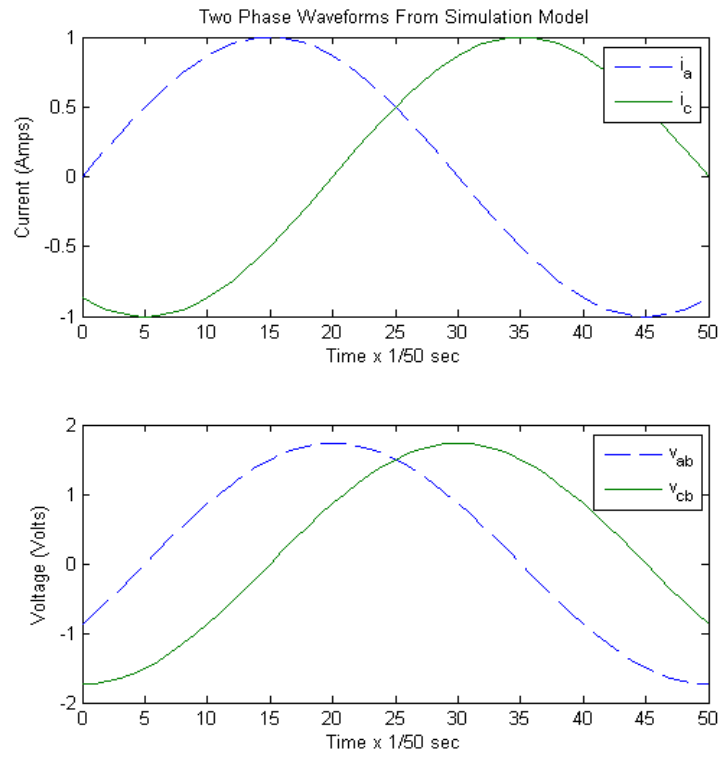


Figure 16. Voltage and Current Input Signals for Two-Phase Calculator

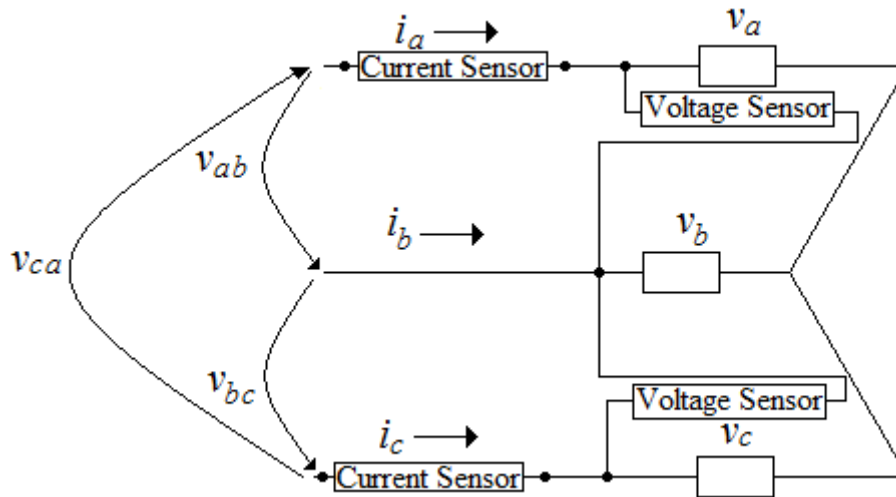


Figure 17. Sensor Connections for Two-Phase Power Calculator

The simulation of the three- and two-phase methods of calculating power are equal therefore Equation (42) can be stated as

$$P = v_a i_a + v_b i_b + v_c i_c = v_{ab} i_a + v_{cb} i_c \quad (42)$$

The only difference between the two methods is the number of sensors necessary to obtain enough information to calculate instantaneous power; therefore, instantaneous power can be measured using two line-to-line voltages and two line currents, because the load is wye-connected.

B. SOFTWARE AND EQUIPMENT

1. Software and Hardware Continuity Validation

A laboratory in [11] was specifically designed and created for a course offered at the Naval Postgraduate School (NPS), Monterey, California, and was used to validate software and hardware continuity in this thesis. The circuit diagram, shown in Figure 18, was taken from the laboratory document. The objective within the laboratory was to take “experimental measurements of voltage and current waveforms typical of a three-phase inverter driving an induction motor using open loop V/f control” [11]. The main goal of the laboratory was to reinforce basic concepts of V/f control and induction motor current harmonic content covered in the NPS course [11].

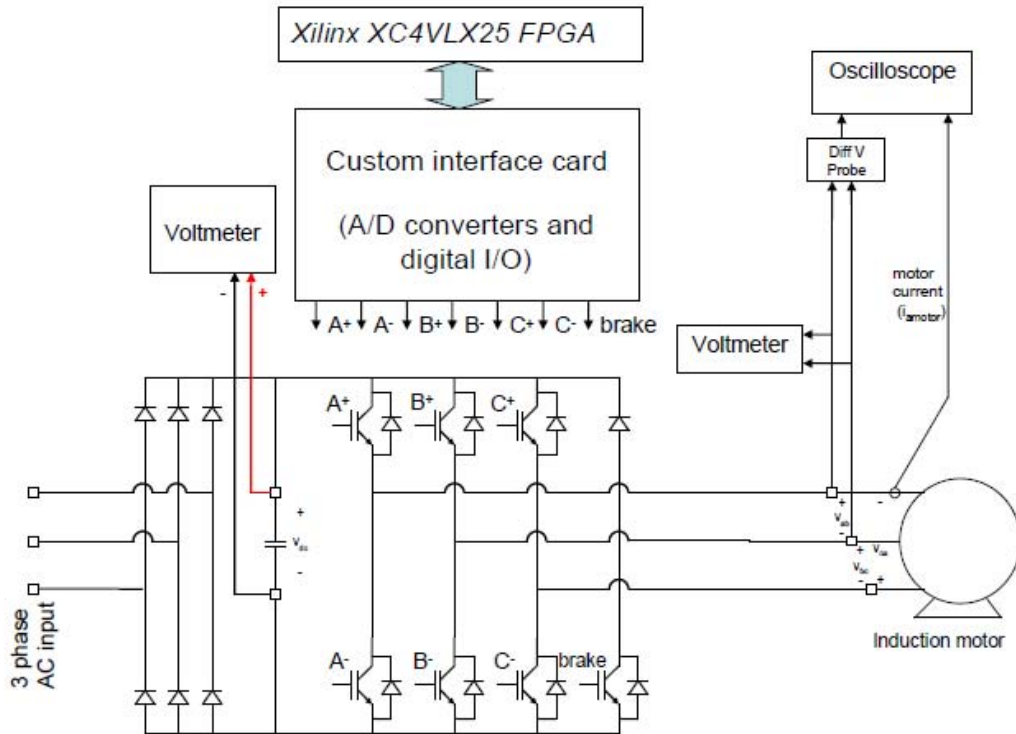


Figure 18. Three-Phase Voltage Source Inverter (VSI) Driving an Induction Motor with Open Loop V/f Control Circuit Diagram [11]

The main equipment used in the laboratory and in this thesis include:

- Xilinx XC4VLX25 FPGA
- Analog to Digital Inverters
- Digital Inputs and Outputs
- Three Phase Squirrel Cage Induction Motor
- Angular Velocity Encoder
- Three Phase Power Supply
- Desktop Computer

For the purpose of this thesis, the completion of the laboratory was necessary to become familiar with the equipment and software while validating the continuity between the software and hardware. The procedures performed are covered in the laboratory

document found in [11]. The concepts regarding space vector modulation is discussed in [11] and [12] and the angular velocity encoder is explained in [12].

2. Electrical and Mechanical Energy Storage

The data sheet for the Semikron power inverter, in Appendix B, contains a description and parameters of the components that comprise the power inverter. The capacitors within the power inverter are two 2200 μF capacitors rated for 400 Volts DC each in series giving the capacitor bank a total of 1100 μF of capacitance at 800 Volts DC. To ensure the capacitor bank was capable of withstanding the energy produced by the motor while the motor was braking, an optimization analysis was performed. This analysis included a three dimensional graph that represents the energy produced for a given change in voltage and the capacitance required to store that energy. Equation (43) is the rotational kinetic energy produced while the rotor and its attached appendages spin down from a given velocity [13].

$$KE_{\text{Rotational}} = \frac{1}{2} I \omega^2 \quad (43)$$

where

- I is the moment of inertia of the rotor and appendages
- ω is the angular velocity of the rotor

While the rotor is braking, this kinetic energy is then converted to an electrical field stored in the capacitor bank neglecting all losses. This energy is calculated by using Equation (44) [14]

$$E_{\text{Electrical}} = \frac{1}{2} C (\Delta V)^2 \quad (44)$$

where

- C is the capacitance of the capacitor bank
- ΔV is the change in voltage across the capacitor bank caused by braking the motor.

The mass of the rotor had to be estimated to determine the moment of inertia of the rotor. To estimate the mass, crude measurements were taken of the rotor and its appendages. The measurements are shown in an AutoCAD drawing, Figure 19.

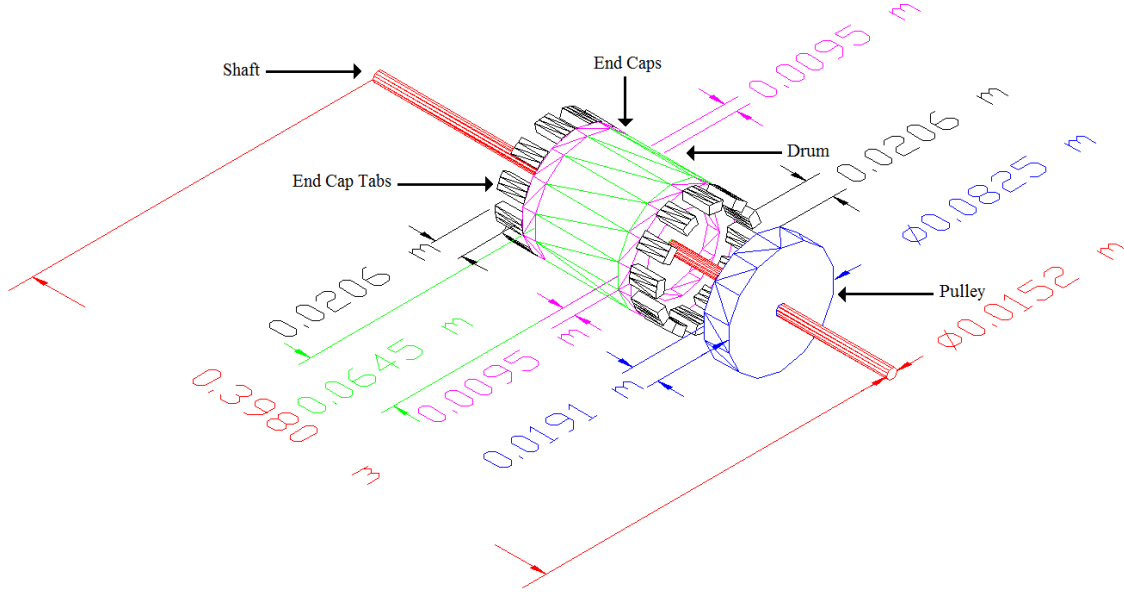


Figure 19. AutoCAD Drawing of Rotor and Dimensions

The rotor attachments were made of various materials, so by judging the materials' appearance, the end caps, end cap tabs, and pulley were assumed to be made of an aluminum alloy, and the main drum of the rotor, including the shaft, was assumed to be made of steel.

The densities, ρ , of the materials were estimated to be:

- Steel [15] $\rho_{Steel} = 7850 \frac{kg}{m^3}$
- Aluminum Alloy [16] $\rho_{Alloy} = 2800 \frac{kg}{m^3}$

Knowing the densities and the dimensions of the material, the volume, V , and mass, m , of each component can then be calculated by using Equations (45) through (55).

$$V_{Drum} = \pi \left(\frac{\phi_{Outside} - \phi_{Inside}}{2} \right)^2 L = \pi \left(\frac{0.0826m - 0.0152m}{2} \right)^2 0.0645m = 2.30 \times 10^{-4} m^3 \quad (45)$$

$$V_{Shaft} = \pi \left(\frac{\phi_{Outside}}{2} \right)^2 L = \pi \left(\frac{0.0152m}{2} \right)^2 0.398m = 7.22 \times 10^{-5} m^3 \quad (46)$$

$$V_{Pulley} = \pi \left(\frac{\phi_{Outside} - \phi_{Inside}}{2} \right)^2 L = \pi \left(\frac{0.0826m - 0.0152m}{2} \right)^2 0.0191m = 6.81 \times 10^{-5} m^3 \quad (47)$$

$$V_{End\ Cap} = 2\pi \left(\frac{\phi_{Outside} - \phi_{Inside}}{2} \right)^2 L = 2\pi \left(\frac{0.0826m - 0.0572m}{2} \right)^2 0.00953m = 9.66 \times 10^{-6} m^3 \quad (48)$$

$$V_{End\ Cap\ Tabs} = 24LWH = 24(0.0206m)(0.0111m)(0.00953m) = 5.23 \times 10^{-5} m^3 \quad (49)$$

$$m_{Drum} = \rho_{Steel} V_{Drum} = \left(7850 \frac{kg}{m^3} \right) (2.30 \times 10^{-4} m^3) = 1.81kg \quad (50)$$

$$m_{Shaft} = \rho_{Steel} V_{Shaft} = \left(7850 \frac{kg}{m^3} \right) (7.22 \times 10^{-5} m^3) = 0.567kg \quad (51)$$

$$m_{Pulley} = \rho_{Alloy} V_{Pulley} = \left(2800 \frac{kg}{m^3} \right) (6.81 \times 10^{-5} m^3) = 0.191kg \quad (52)$$

$$m_{End\ Caps} = \rho_{Alloy} V_{End\ Caps} = \left(2800 \frac{kg}{m^3} \right) (9.66 \times 10^{-6} m^3) = 2.71 \times 10^{-2} kg \quad (53)$$

$$(54)$$

$$m_{End\ Cap\ Tabs} = \rho_{Alloy} V_{End\ Cap\ Tabs} = \left(2800 \frac{kg}{m^3} \right) (5.23 \times 10^{-5} m^3) = 0.147kg \quad (55)$$

Where

- V is the volume a component
- ϕ is the diameter of a component
- L is the length of a component

Using Equations (56) and (57), the total moment of inertia, I_{Total} , in Equation (58) can now be calculated.

$$I_{Solid\ Cylinder} = \frac{1}{2} m r^2 \quad [17] \quad (56)$$

$$I_{Thick\ Hollow\ Disk} = \frac{1}{2} m (a^2 + b^2) \quad [18] \quad (57)$$

$$I_{Total} = \sum_{n=1}^i I_n \quad (58)$$

where

- r is the radius
- a is the outer radius
- b is the inner radius

Equations (59) through (64) are the hand calculations performed to calculate the total moment of inertia, I_{Total} .

$$I_{Drum} = \frac{1}{2}(1.81kg) \left(\left(\frac{0.0826m}{2} \right)^2 + \left(\frac{0.0152m}{2} \right)^2 \right) = 1.60 \times 10^{-3} kg \cdot m^2 \quad (59)$$

$$I_{shaft} = \frac{1}{2}(0.567kg) \left(\frac{0.0152m}{2} \right)^2 = 1.64 \times 10^{-5} kg \cdot m^2 \quad (60)$$

$$I_{pulley} = \frac{1}{2}(0.191kg) \left(\left(\frac{0.0826m}{2} \right)^2 + \left(\frac{0.0152m}{2} \right)^2 \right) = 1.68 \times 10^{-4} kg \cdot m^2 \quad (61)$$

$$I_{End Caps} = \frac{1}{2}(2.71 \times 10^{-2} kg) \left(\left(\frac{0.0826m}{2} \right)^2 + \left(\frac{0.0572m}{2} \right)^2 \right) = 3.42 \times 10^{-5} kg \cdot m^2 \quad (62)$$

$$I_{End Caps Tabs} = \frac{1}{2}(0.147kg) \left(\left(\frac{0.0826m}{2} \right)^2 + \left(\frac{0.0731m}{2} \right)^2 \right) = 2.24 \times 10^{-4} kg \cdot m^2 \quad (63)$$

$$I_{Drum} + I_{shaft} + I_{pulley} + I_{End Caps} + I_{End Caps Tabs} = I_{Total} = 2.04 \times 10^{-3} kg \cdot m^2 \quad (64)$$

Since the motor is rated for 1670 revolutions per minute (RPM), the maximum rotational kinetic energy, $KE_{Rotational}$, possibly created by the motor, is displayed in Equation (65).

$$KE_{Rotational} = \frac{1}{2} \left(2.04 \times 10^{-3} kg \cdot m^2 \right) \left(\left(\frac{1670 rev}{min} \right) \left(\frac{360^\circ}{rev} \right) \left(\frac{2\pi rads}{360^\circ} \right) \left(\frac{min}{60 sec} \right) \right)^2 = 31.2 \text{ Joules} \quad (65)$$

An optimization graph, Figure 20, was developed in MATLAB to illustrate the required capacitance for a given energy produced by a given change in voltage. Appendix C contains the code used to generate Figure 20. In this analysis, the worse case voltage change was assumed to be 800 volts since the capacitor bank is rated for 800

volts DC. The capacitance of the capacitor bank is 1100 μF , so the maximum energy that can be absorbed by the capacitor bank with a 800 Volt DC change was found to be 352 Joules, as shown in Equation (66).

$$E_{\text{Electrical}} = \frac{1}{2} C (\Delta V)^2 = \frac{1}{2} (1100 \times 10^{-6} \text{ F}) (800 \text{ V})^2 = 352 \text{ Joules} \quad (66)$$

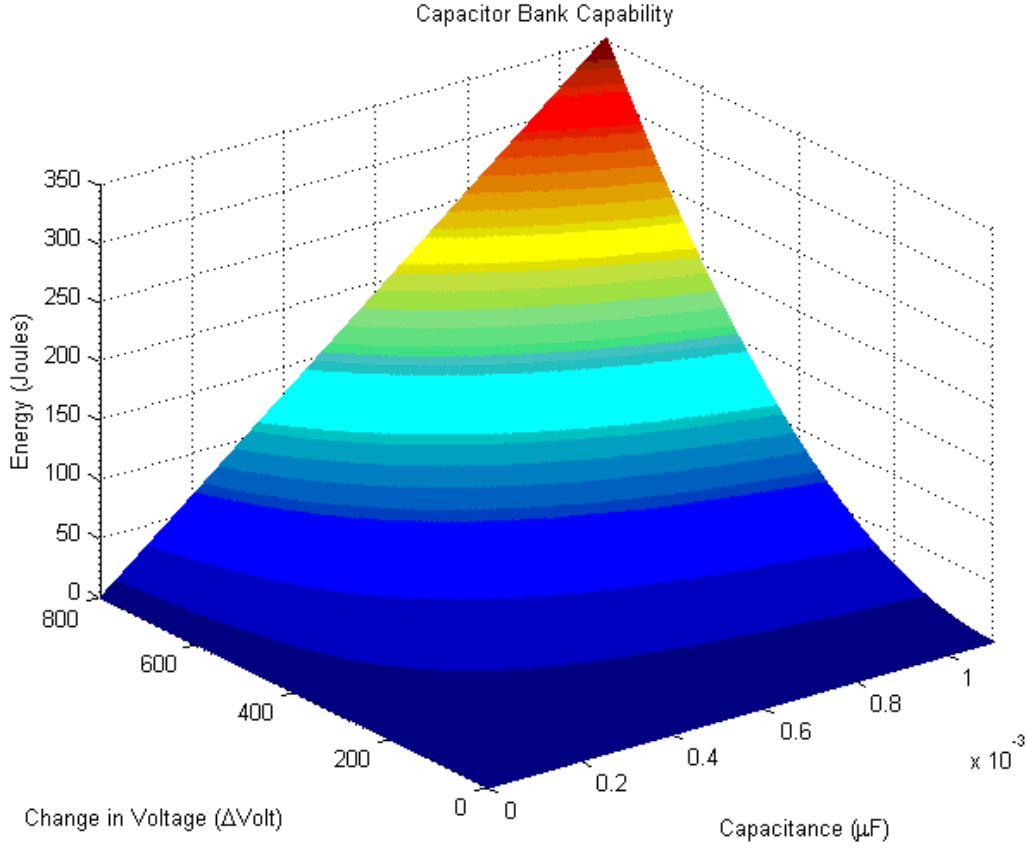


Figure 20. Capacitor Bank Capability Optimization Graph

3. Understanding Software and Hardware Interfaces

To further understand the modeling concept, the multiple interfaces between software, hardware, and end user should be understood. The software used in this thesis includes:

- MATLAB
- Simulink
- Xilinx
- CHIPSCOPE
- Project Navigator

The hardware includes:

- Field Programmable Gate Array (FPGA)
- Semikron Power Inverter Box
- 220 Volt Three Phase (3Φ) 60 Hz AC Power Supply
- 4 pole, 0.25 Hp, 3Φ , 60 Hz Squirrel Cage Induction Motor
- Angular Position Encoder
- Desktop Computer Terminal

A block diagram, Figure 20, was created to illustrate the interface boundaries used in the experiment. This diagram also provides the flow of information between the interfaces. A generalized description of each interface's purpose within this thesis is provided below.

Desktop Computer Terminal

- Provides graphical user interface with computer software
- Provides visual display of status of software code development, data collection, data manipulation

MATLAB

- Provides environment for Simulink software
- Contains initial condition code for Simulink models
- Enables the End User to manipulate data collected by Chipscope during the experimentation for graphical representation

Simulink

- Provides an environment for model creation of any system that can be represented mathematically
- Enables the End User to modify models for thesis experiment
- Provides simulation environment to test model components for functionality and correctness prior to model implementation
- Contains Xilinx model building blocks including Xilinx System Generator
- Uses Xilinx System Generator to convert models into computer language code

Xilinx

- Provides environment for Chipscope and Project Navigator software
- Provides Simulink with capability to convert models into computer language code

Project Navigator

- Converts computer language code to binary code

Chipscope

- Uploads binary code from Xilinx Project Navigator to the FPGA
- Enables End User to control experiment through a graphical user interface with a Motor On/Off command and a Collect Data/Stop Motor Sequence command
- Enables End User to export data collected from each experiment trial to a file format in which MATLAB can read

Field Programmable Gate Array (FPGA)

- Controls Power Inverter voltage output to motor
- Relays data collected from the Angular Position Encoder and A/D Inverter to Chipscope

Analog to Digital (A/D) Converter

- Converts analog signal to a digital signal from power inverter to motor and from motor to power inverter

0.25 Hp Three-Phase (3Φ) 60 Hz Squirrel Cage Induction Motor

- Provide medium for regenerative braking experiment

Angular Position Encoder

- Sends real time encoded angular position of motor to FPGA for processing

220 Volt 3Φ 60 Hz AC Power Supply

- Provides electrical power to power inverter

Semikron Power Inverter Box

- Controls speed of the motor by regulating the voltage supplied to the motor

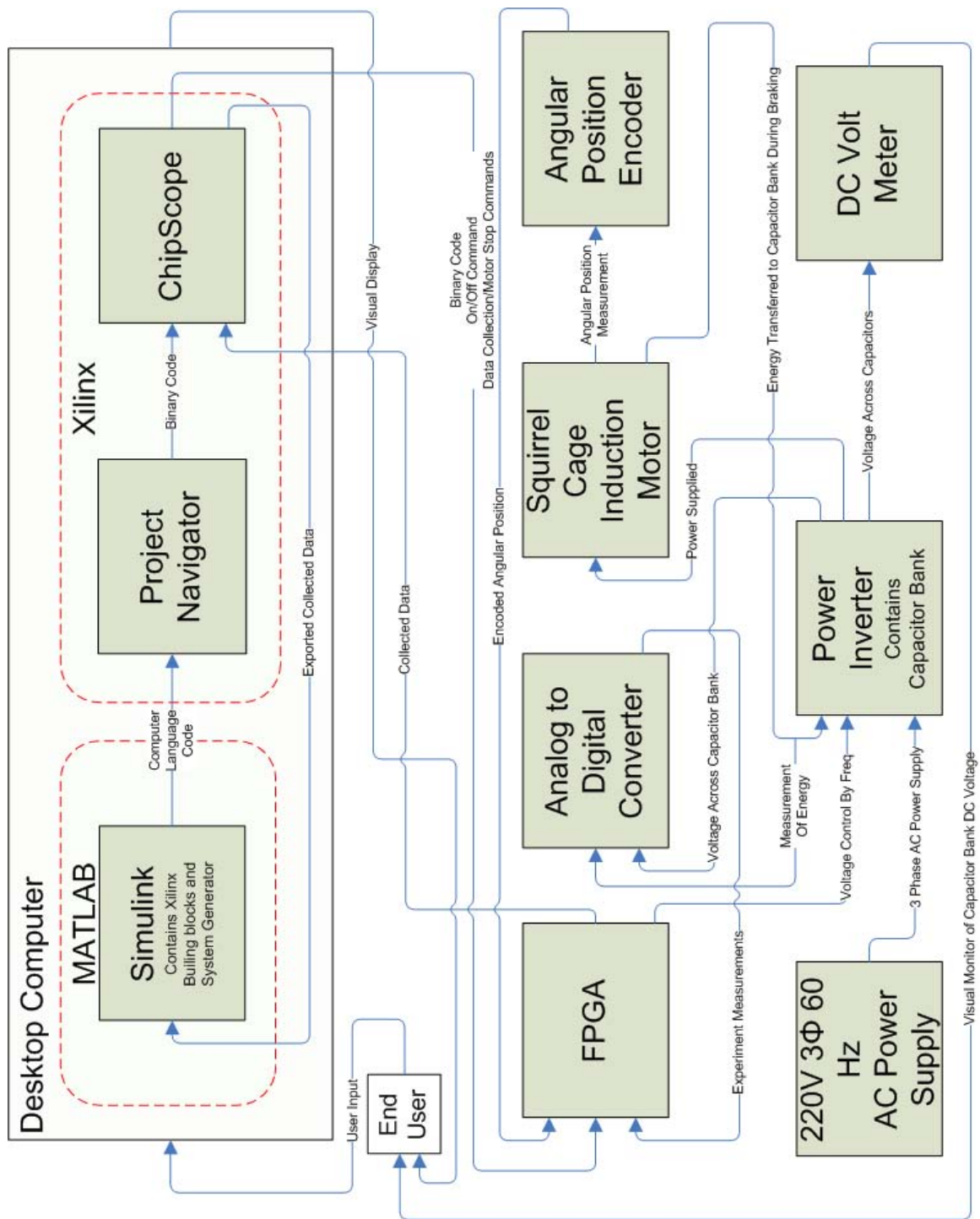


Figure 21. Software/Hardware Interface Flow Chart

III. REGENERATIVE BRAKING MODELING

A. MODEL SETUP

The model setup for the purpose of this thesis consisted of modifying a Simulink model in [11]. This was to allow for the modeling and demonstrating of regenerative braking using a squirrel cage induction motor through V by f control. Figure 22 is the circuit diagram for the experiment. The circuit diagram was modified from [11].

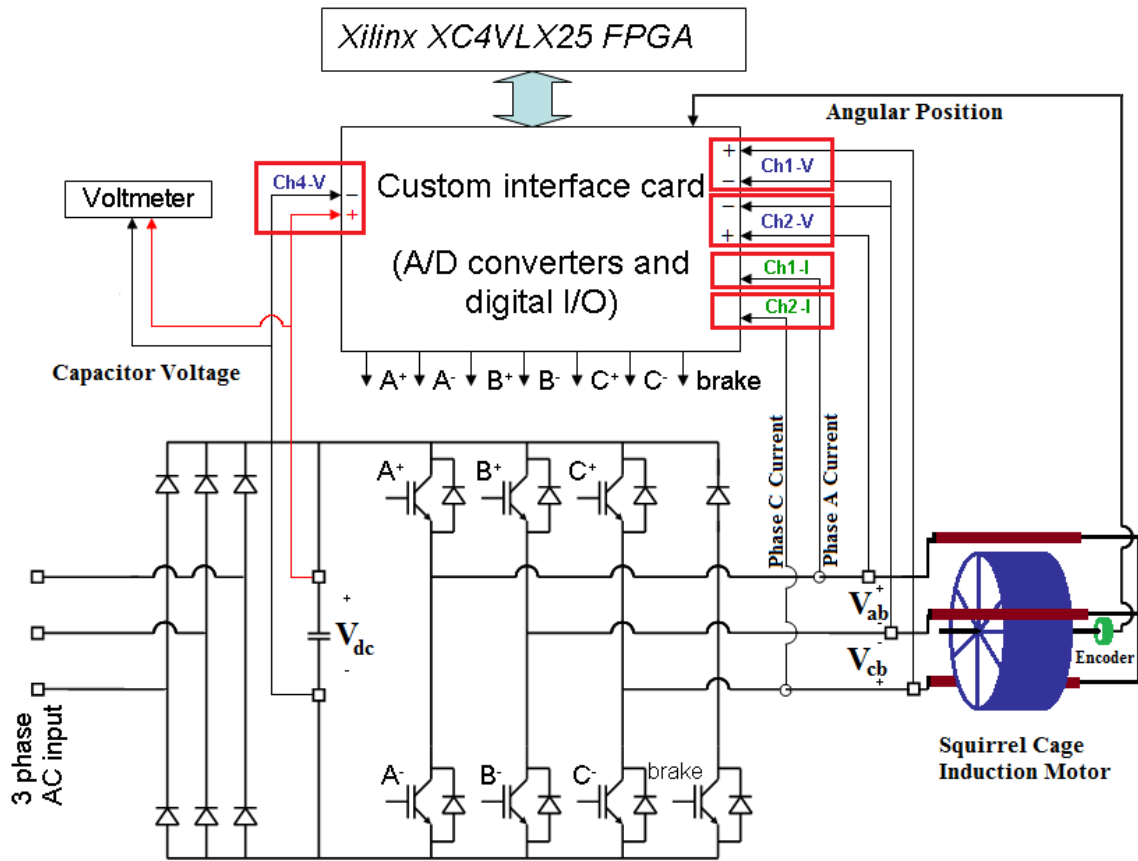


Figure 22. Experiment Circuit Diagram [After 11]

The measurements for v_{ab} and v_{cb} were taken from points between the power inverter and the motor as shown in Figure 22. The capacitor bank voltage was measured directly from the power inverter. The angular velocity of the rotor was measured using

the encoder that was coupled to the rotor. The encoder measured angular position. The transformation from an angular position to an angular velocity is described in [12].

Figure 23 is the original model for the laboratory experiment in [11], and the model for this thesis experiment is shown in Figure 24. The modifications to the original model include:

- Removal of the Data Rate Block
- Replacing the open/closed input of the Speed Control block with an on/off input
- Replacing the `omega_rotor_e` input of the Speed Control block with an `enable_ramp` input
- Adding a Q output for the Speed Control block
- Changing the Phase_B output title to Trigger Data Collection of the Chipscope Interface block
- Adding a Delay Trigger block with a Trigger Motor Stop Countdown input and a Initiate Motor Stop output
- Removal of the `rotor_vs_commanded` speed block
- Adding an A to D voltage and an A to D current block
- Adding a Power Computer block
- Adding an AND gate
- Changing Encoder output from `omega_rotor_e` to `wr`



The Data Rate Control block was removed because the A to D voltage block contains a data rate function that is synonymous to the Data Rate Control block's function. The purpose of the data rate was to establish the length of time of each sample taken in Chipscope. Time for model simulation in Simulink is measured in steps. While configuring the parameters for a model in Simulink, there was an option for length of time for each step. For the purpose of this thesis experiment each step equaled 40 nanoseconds.

The sample times varied for each experiment trial due to the data sampling limitations within Chipscope's programming. The Chipscope program used in this experiment sampled exactly 8191 data points during any given trial. The sample rate in Chipscope is dependent on the data rate established in the Simulink model prior to VHDL code generation. To ensure the collection of data during an entire event trial, the data rate had to be established to fit the event into Chipscope's 8191 sample window.

The speed control block had been modified by adding a SR-Flip Flop and a motor stopping rate control feature called the motor "ramp". The purpose of the SR-Flip Flop is to prevent the motor from restarting the motor stop sequence without End User input. Table 1 contains the truth table of an SR-Flip Flop. The Q signal output of the speed control box only goes "set", a binary value of one, if the operator selects the On/Off Button in Chipscope's GUI to a value one as shown in Figure 25. When the On/Off Button is selected "On," the AND Gate will become a binary one value from a zero value, and the motor will begin to run at the commanded speed.

Table 1. SR-Flip Flop Truth Table

S	R	Q	Q'
0	1	0	1
1	0	1	0
0	0	1	0
1	1	Not Defined	

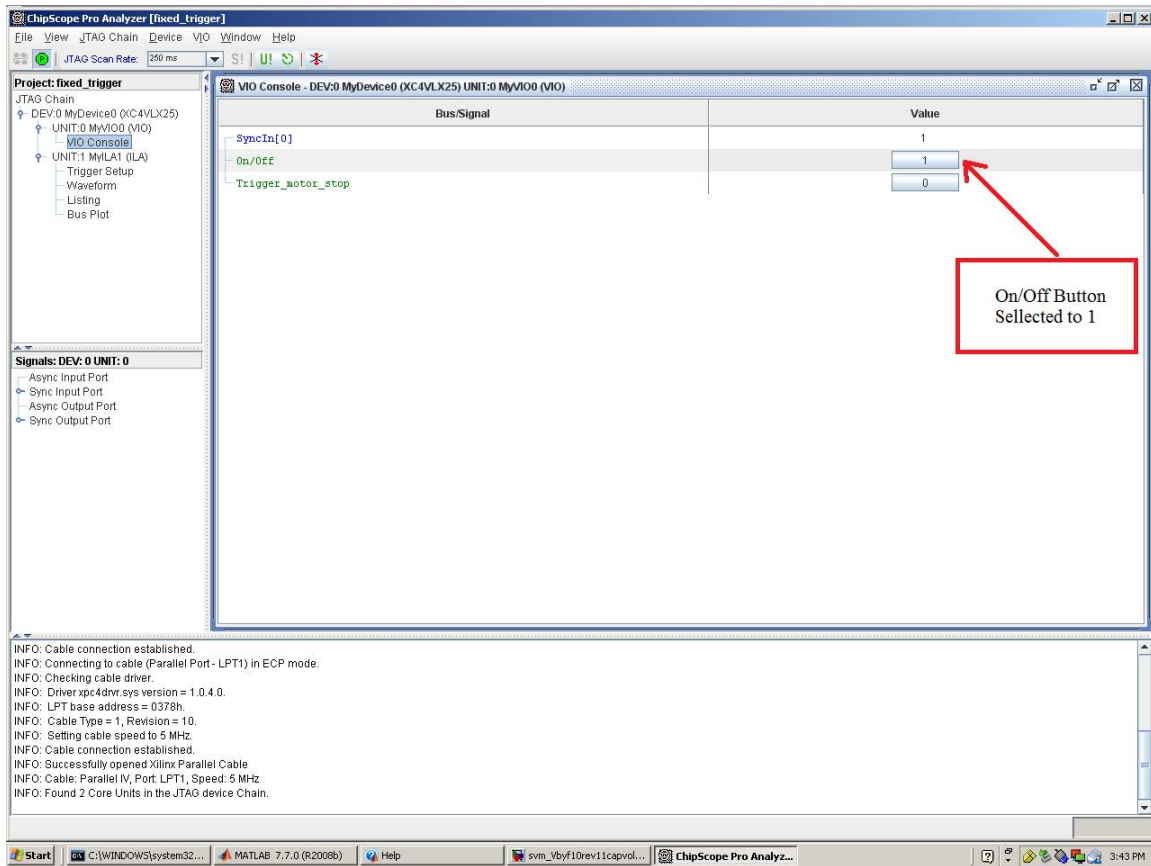


Figure 25. Chipscope GUI Display for Motor Run Configuration [From Chipscope Pro Analyzer, 2010]

The ramp's function was to provide a means to command the motor to stop. The motor was first started at a commanded speed set for 120π radians per second, which is approximately 377 radians per second and remained at this speed until the enable_ramp signal received a binary one value. At that time the counter was enabled, and it began to count up to 378 in steps predetermined in the block parameters, until the rationale of the initial frequency minus the counter value is less than zero. Once the rationale became less than zero, the counter was then disabled. At the same time Q was reset to a binary value of zero, returning the AND gate to a binary value zero, causing the motor power supply to be turned off. Figure 26 is the internal model diagram of the speed control block.

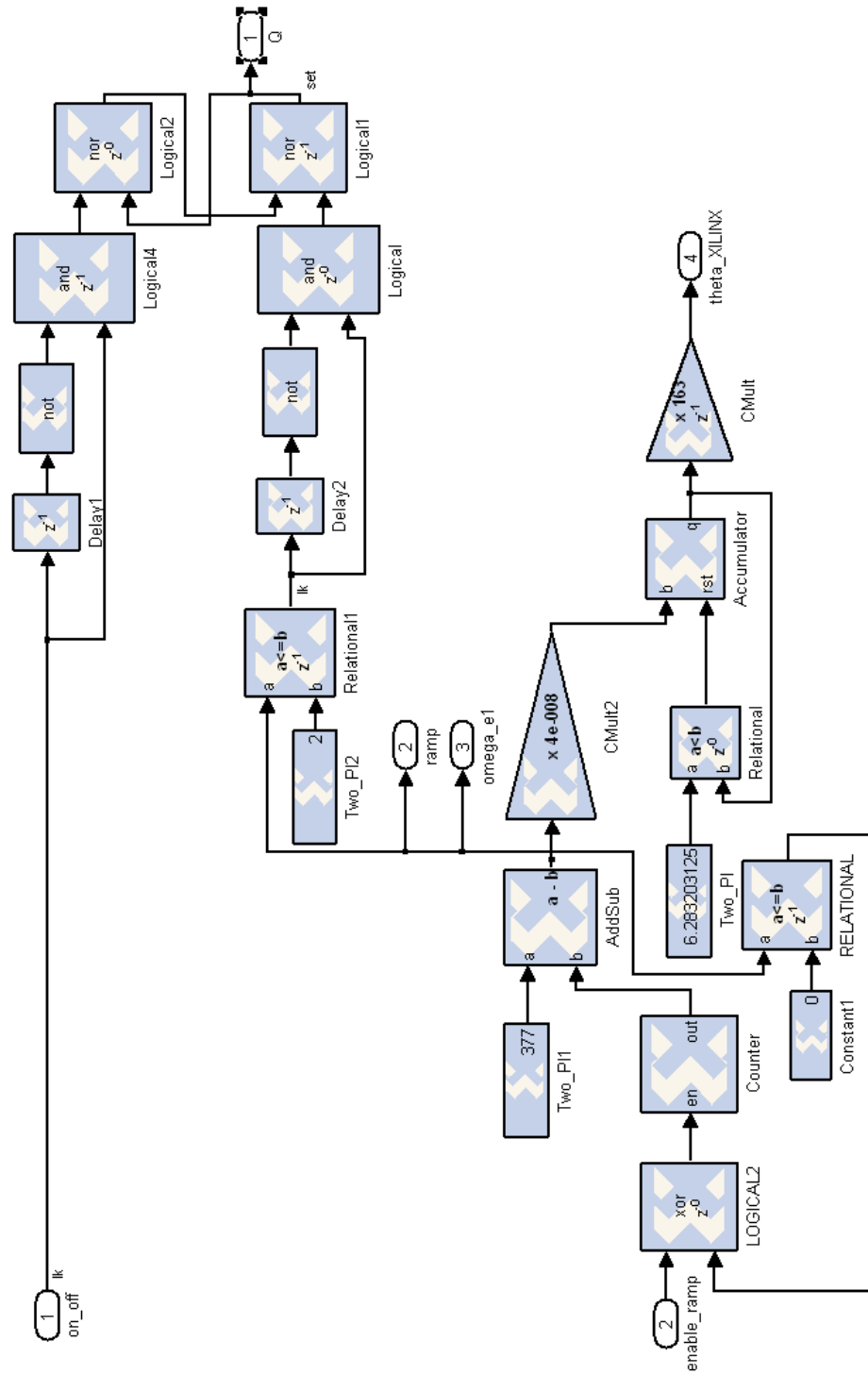


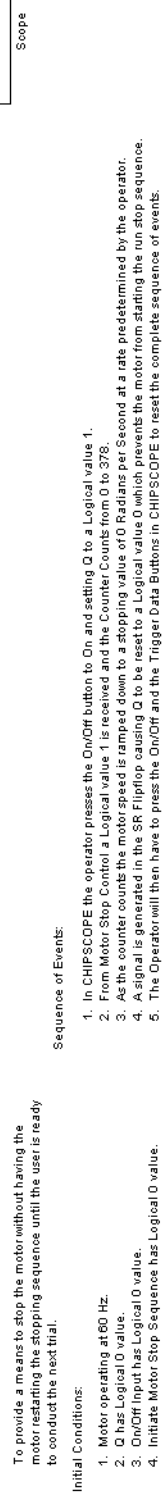
Figure 26. Speed Control Component with SR-Flip Flop

B. TESTING SR-FLIP FLOP OF MODEL

To ensure the SR-Flip Flop functionality was correct, the model in Figure 27 was created in Simulink to simulate the stopping of the motor, resetting of the experiment, and then reinitiating the stopping of the motor. The complete sequences of events are described in the model figure. The waveform outputs for the model are in Figure 28. This figure provides a timeline for the events as they occurred in the simulation.

The Delay Trigger block was necessary to provide enough time to collect data during the steady state speed of the motor prior to the motor being commanded to commence decelerating. Once the motor reached steady state speed, the End User then selected the “Trigger_stop_motor” button in the Chipscope GUI, as shown in Figure 29, to initiate the motor stop sequence. Once this occurred, multiple events took place. Referring back to Figure 24, the output of the Trigger_stop_motor was an input for both the Delay Trigger block and the Data Conversion block. A signal was sent back to Chipscope to initiate the data sampling, and at the same time the motor stop countdown began as described in the following paragraph.

When the binary value one was received by the Delay Trigger block, the counter was enabled and it began to count up in steps predetermined in the block parameters. Once the rationale of the constant 5×10^8 minus the counter value was less than zero, then the counter was disabled and a binary one value was sent to the speed control block. When the speed control block received a binary one signal, the deceleration of the motor was enabled. Figure 30 is the internal model diagram of the speed control block.



49

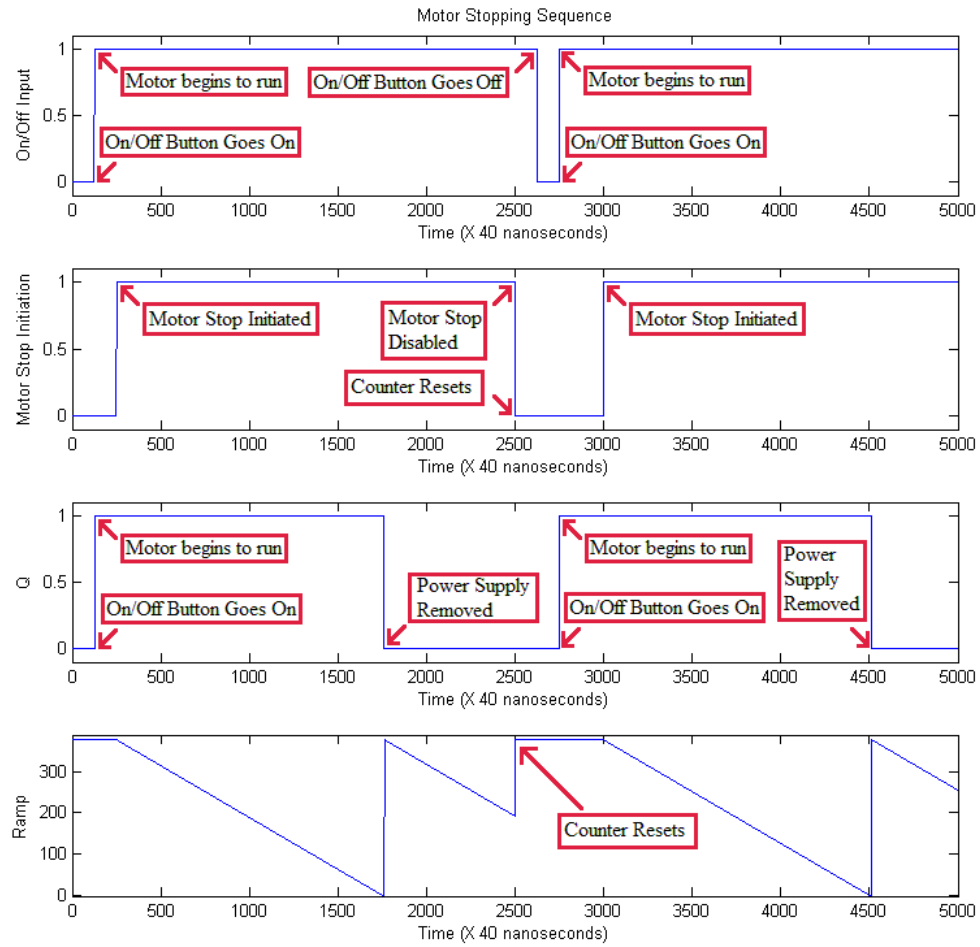


Figure 28. SR-Flip Flop Wave Output of Test Model

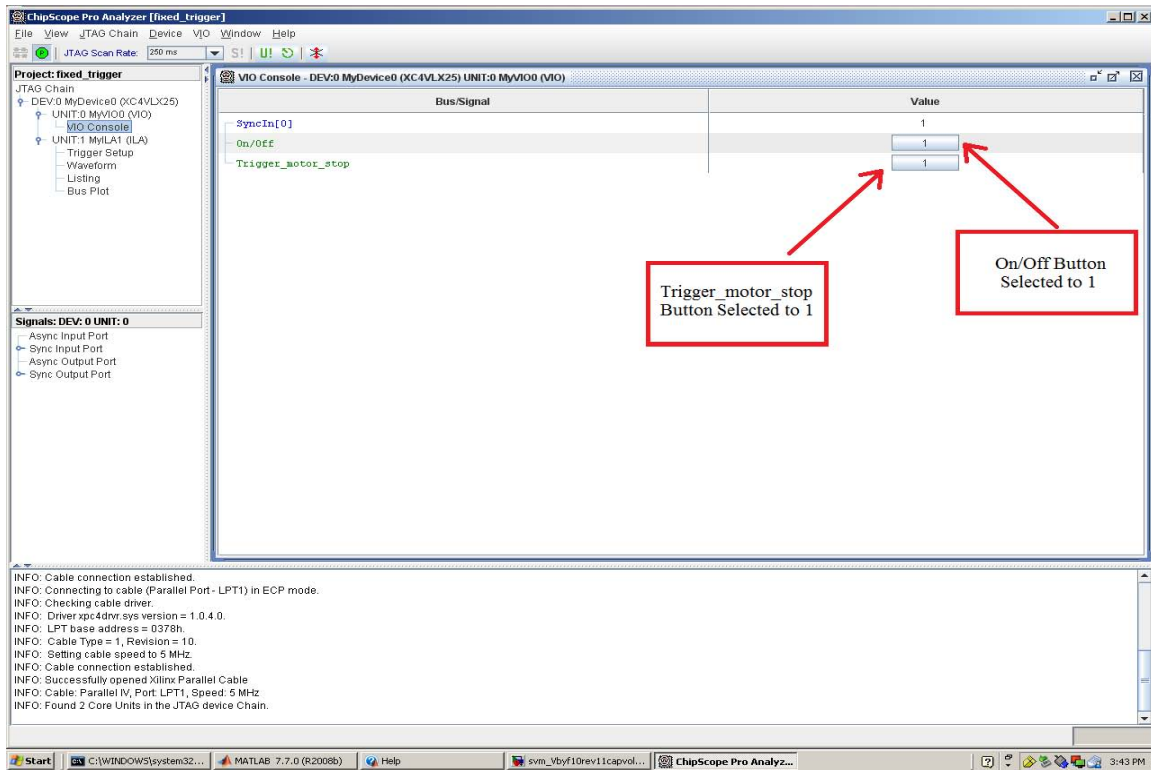


Figure 29. ChipScope GUI Display for Motor Stop Configuration [From ChipScope Pro Analyzer, 2010]

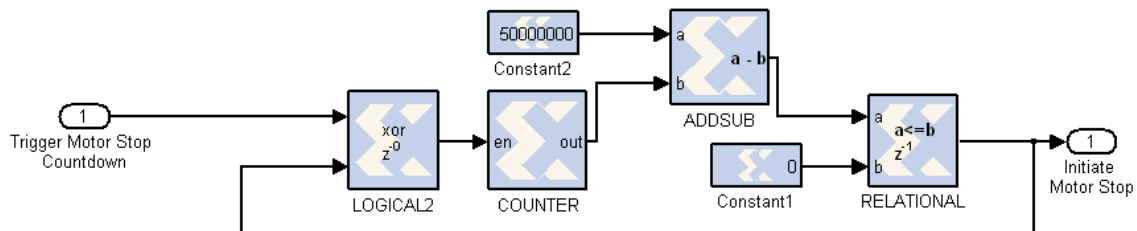


Figure 30. Stop Motor Delay Test Model

C. TESTING THE DELAY TRIGGER MODEL COMPONENT

To ensure the Delay Trigger functioned correctly, the model in Figure 31 was created to simulate the initiation of stopping the motor and resetting of the experiment. The complete sequences of events are described in the model figure. The waveform outputs for the model are in Figure 32. This figure provides a timeline for the events as they occurred in the simulation.

52

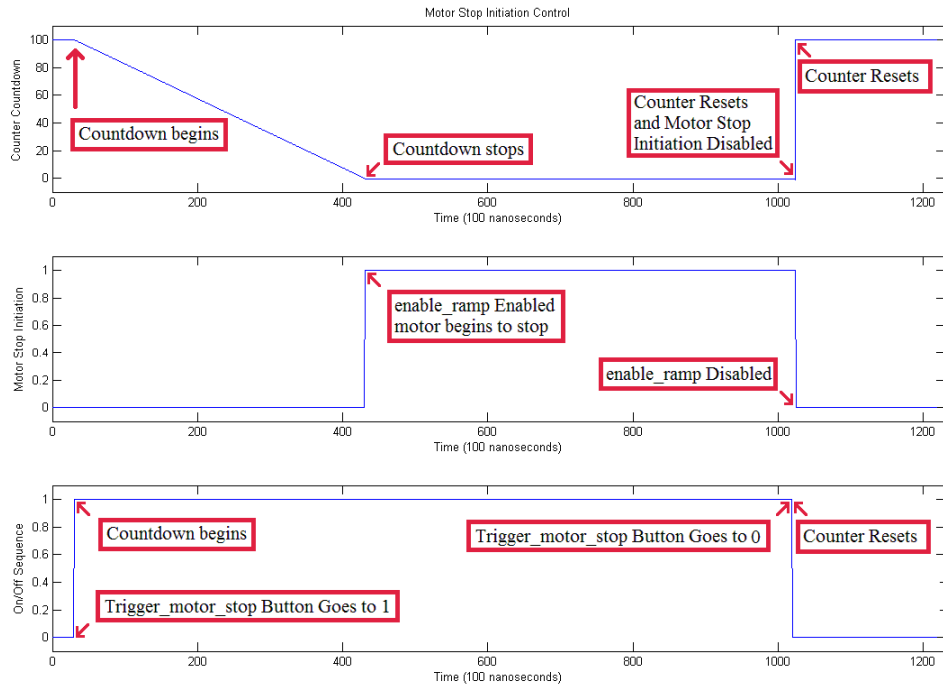


Figure 32. Trigger Delay Test Model Wave Output Analysis

The above tasks were necessary to gain an understanding of the software and hardware used to model and demonstrate regenerative braking of a squirrel cage induction motor using V by f control. Chapter IV will analyze the data collected from the experiments of this thesis.

THIS PAGE INTENTIONALLY LEFT BLANK

IV. RESULTS

In this chapter, the data collected from each experiment was analyzed. The MATLAB code used to generate Figures 33 through 59 is contained in Appendix D. There are six varieties of analysis performed. The first analysis was an observation of three graphs that captured the actual rotor velocity compared to the commanded velocity, the behavior of power as measured between the power inverter and the motor, and the change in voltage across the capacitor bank during the events of each experiment. Another analysis compared two experiments with one another to further understand the effects of varying the deceleration rates on regenerative braking. The comparisons consist of experiments with double and half deceleration times of each other. The third analysis compared the commanded angular velocity with actual angular velocity by graphing the difference between the two angular velocities. A fourth analysis looks at the behavior of current during the experiments. The fifth analysis observes the I^2R losses and power generated, while the last analysis discusses energy allocation and conservation.

Each experiment was conducted under similar conditions. The motor did not have a load attached during the experiments and it was spinning at a steady state speed prior to initiation of the experiment. The voltage across the capacitor bank of the power inverter was measured while the motor was running using a voltmeter to ensure 180 volts DC existed across the capacitors prior to the experiment. Once this condition was met, the experiment was initiated using the toggle button “Trigger Data Collection Button” in Chipscope. After each experiment a filter, created in Simulink, was used to filter the noise in the channels of the analog to digital inverters to produce more legible graphs. The filter designs for each experiment are contained in Appendix E. The “noise in commanded speed is not real. It is an artifact of Chipscope.” Professor Julian, in [19], stated that he had “...extracted internal FPGA signals through Chipscope and a USB interface at the same time and found that the noise in the Chipscope signals was not really present on the FPGA signals” [19].

There were eight independent experimental trials, each with different deceleration times. These deceleration times varied from 0.495 seconds to 63.418 seconds, each doubling in time. Due to Chipscope's data collection limitation, the sample rate had to be adjusted to fit each experiment's events into the 8191 sample points available. Table 2 provides parameters for each experiment conducted. The length of time per step for all trials was 40 nanoseconds.

Referring back to Figure 22, this figure illustrates the model layout for the thesis experiment. The power supply provided electrical power input to the power inverter. The FPGA was programmed to control the power inverter output to the motor to control the motor's speed using SVM, which is described in [12]. Due to the limited number of input channels into Chipscope, multiple runs of each experiment had to be performed to collect all the data necessary for the analyses within this thesis.

Table 2. Experiment Parameter Table

Experiment #	Clock Cycles Per Sample	Commanded		# of Samples Before Deceleration	Pre Motor Stop Data Time (sec)	Total Recorded Time (sec)
		Stop Time (sec)	Deceleration Rate (rad/sec)			
1	4096	0.495	760.9	600	0.098	1.342
2	8192	0.991	380.5	3200	1.049	2.684
3	16384	1.982	190.2	1600	1.049	5.368
4	16384	3.964	95.1	1600	1.049	5.368
5	32768	7.927	47.6	800	1.049	10.736
6	65536	15.854	23.8	400	1.049	21.472
7	131072	31.709	11.9	200	1.049	42.944
8	262144	63.418	5.9	100	1.049	85.889

A. COMMANDED AND ACTUAL ANGULAR VELOCITIES, POWER, AND CHANGE IN VOLTAGE ANALYSIS

Figures 33 through 40 contain the graphs produced from the data collected from the experiments. Referring to the Angular Velocity Graphs of the figures, the rate of deceleration of the rotor followed very closely to the commanded rate of deceleration. Experiments 1 through 4 displayed a mismatch in commanded and actual rotor speeds during the deceleration where the rotor speed was higher than the commanded speed. In Experiment 5, Figure 37, the power became less negative 3 seconds after initiation and then became more negative at 4.5 seconds. This coincides with the speeds for both actual

rotor and commanded speeds becoming more equal around 3 seconds and less equal around 4.5 seconds. This confirms when slip is less, the power induced in an induction generator is less. Therefore, when the magnetic field angular velocity is equal to the rotor angular velocity, no power is induced or consumed. This would explain the initial steady state condition prior to decelerating where rotor speed was slightly less than commanded speed. This was expected due to the no load slip characteristics of the induction motor, but once the deceleration command initiated, the rotor speed over shot commanded speed as in Experiments 1 through 4, and then followed command deceleration rate very closely. The delay in the rotor response was due to the angular momentum of the rotor at the time of the initial deceleration command.

Power started at or less than zero Watts for each experiment. Since power was near zero Watts due to the no load condition previously mentioned, the filters used to help reduce the noise levels in the collected data caused the initial data to become negative. At the time deceleration commenced, the power became more negative until the power supply was removed at the time commanded angular velocity was zero. In this region regeneration occurred and power was being sent back to the power inverter where the energy was routed to the capacitor bank. This is evident because the change in voltage peaked positive at the same time as power. At the time where commanded angular velocity was zero, power should also be zero, but due to filtering of the power signal there was a response time delay before power reached zero.

The reason the actual angular velocity, in Experiments 1 through 3, never reached zero radians per second was because the deceleration rate was too fast for the rotor's angular momentum. The power supply to the motor was controlled by the commanded angular velocity input to the power inverter. As the commanded angular velocity reached zero radians per second, which had been predicted in the SR-Flip Flop tests in Chapter III of this thesis, power supply to the motor was removed. Even though the motor came to a complete stop for all experiments conducted, the explanation for the non-zero angular velocity for the rotor is that the sample rate in Chipscope was too fast. This sample rate shortened the sample window such that the rotor was still rotating when the last sample

was taken. This would explain the exponential decay of actual angular velocity after commanded angular velocity reached zero. At that time, the angular momentum of the rotor prevented the rotor from stopping instantaneously.

During the events for all the experiments, the change in voltage at the end of the experiments was always at a greater value than originally started. The ending value of the voltage across the capacitor bank is related to the energy from the regenerative braking. There are many dynamic considerations that were not taken into account in this thesis. One dynamic situation might include the bleed resistor attached across the capacitor bank to allow the capacitors to discharge when the power inverter is disabled. This feature could have depleted some of the energy while the capacitor banks were being charged. The bleed resistor is most likely a safety feature installed on the power inverter to prevent accidental discharge, which could result in an injury to a person or damage to equipment.

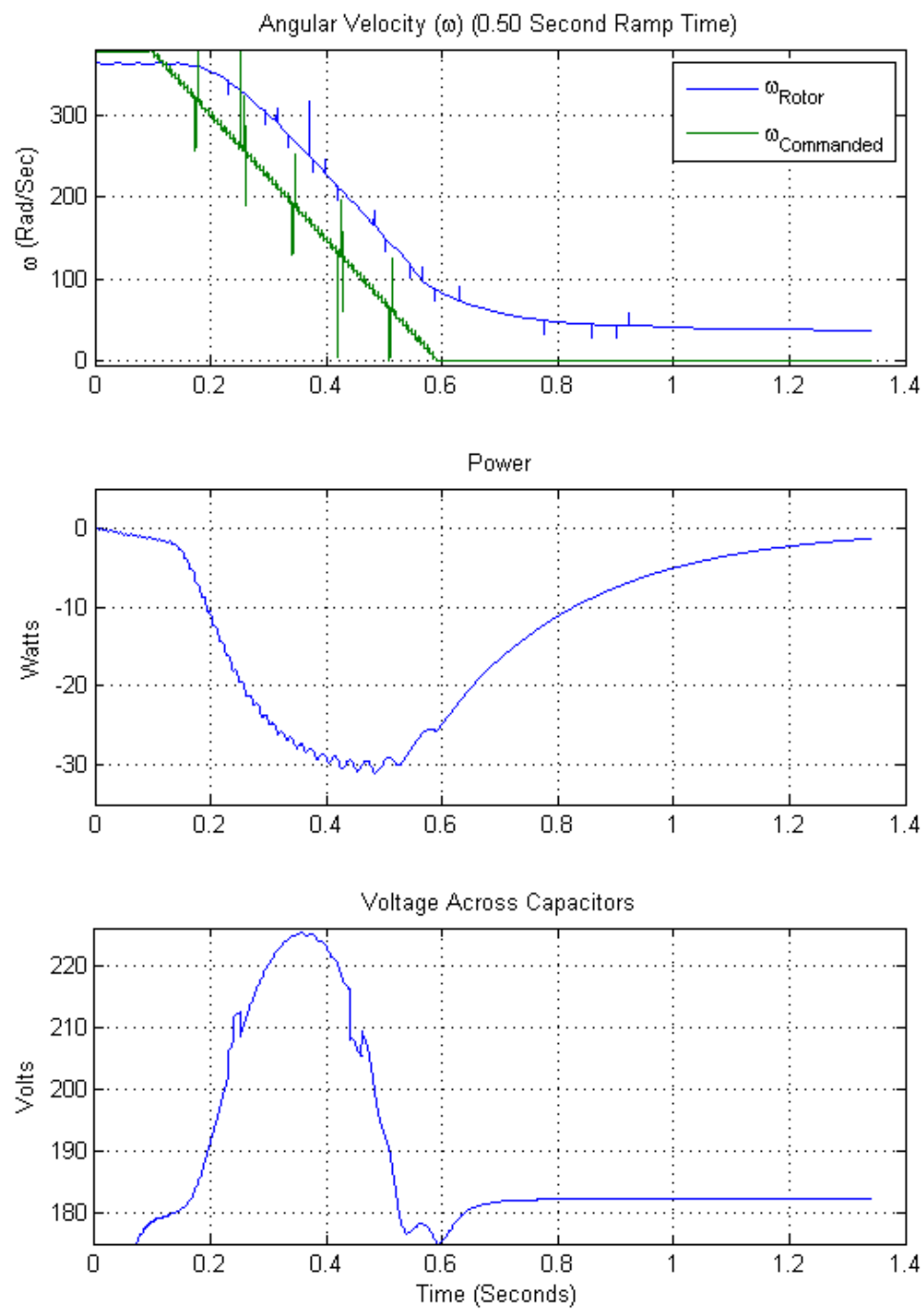


Figure 33. Experiment 1 Results

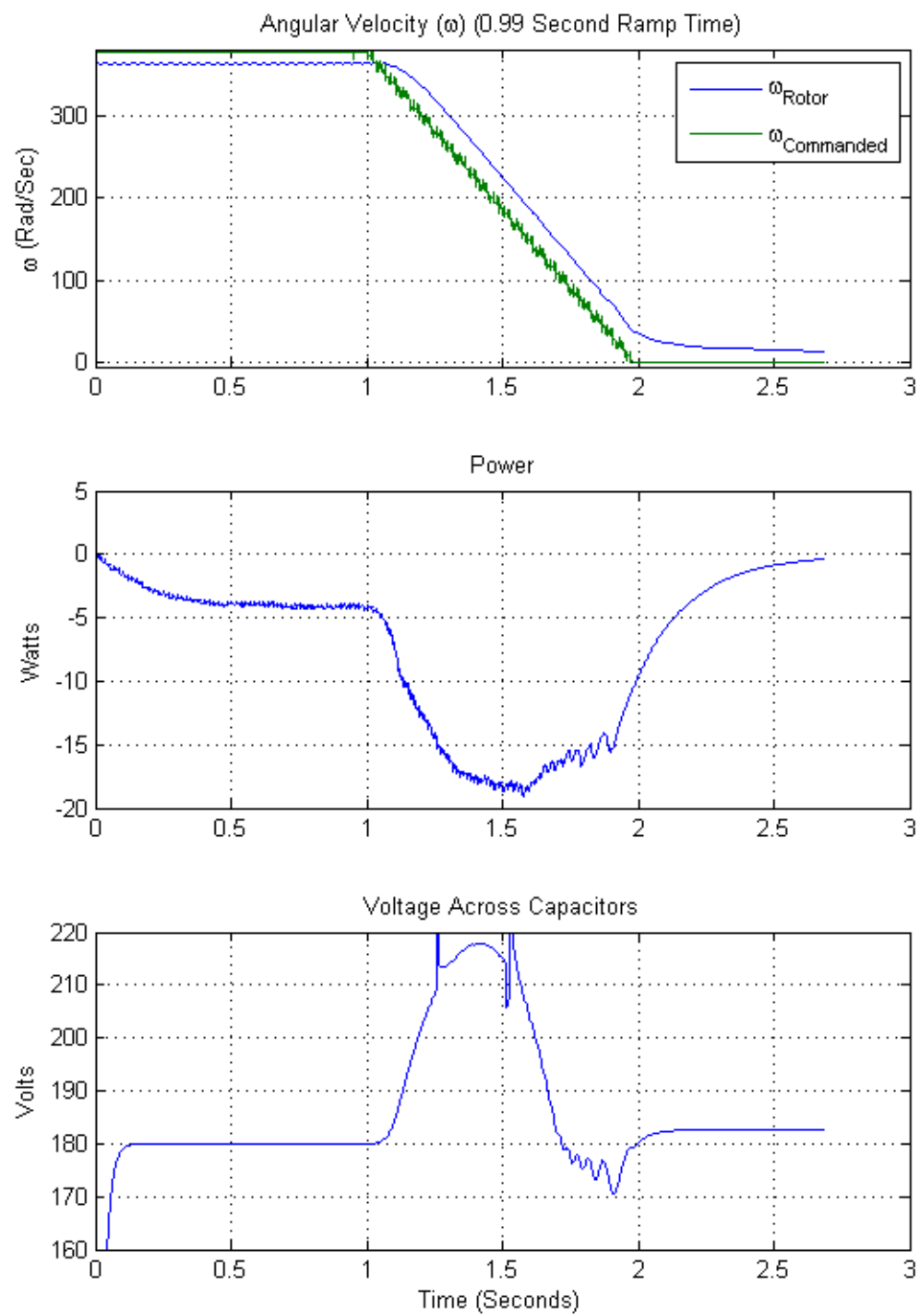


Figure 34. Experiment 2 Results

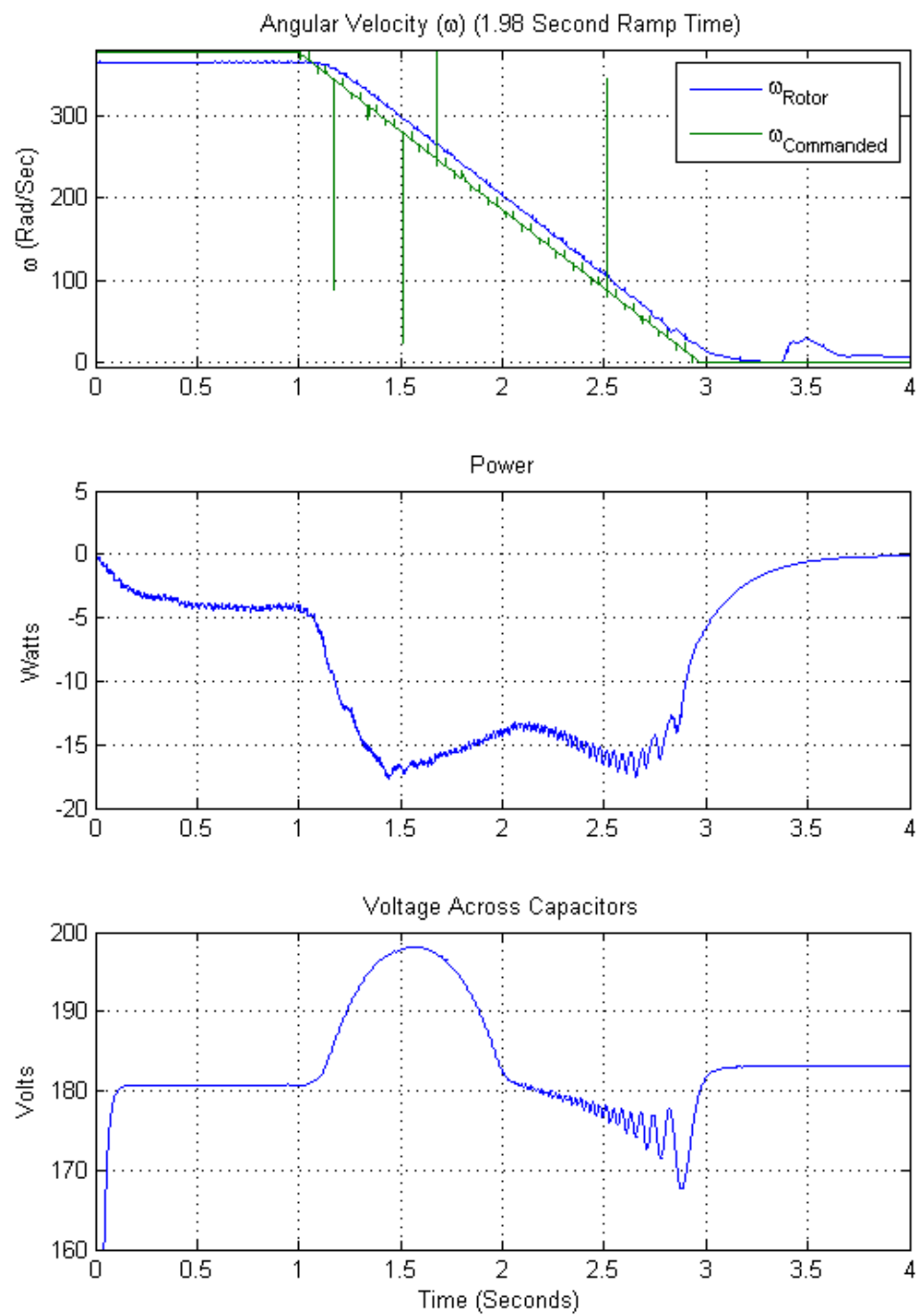


Figure 35. Experiment 3 Results

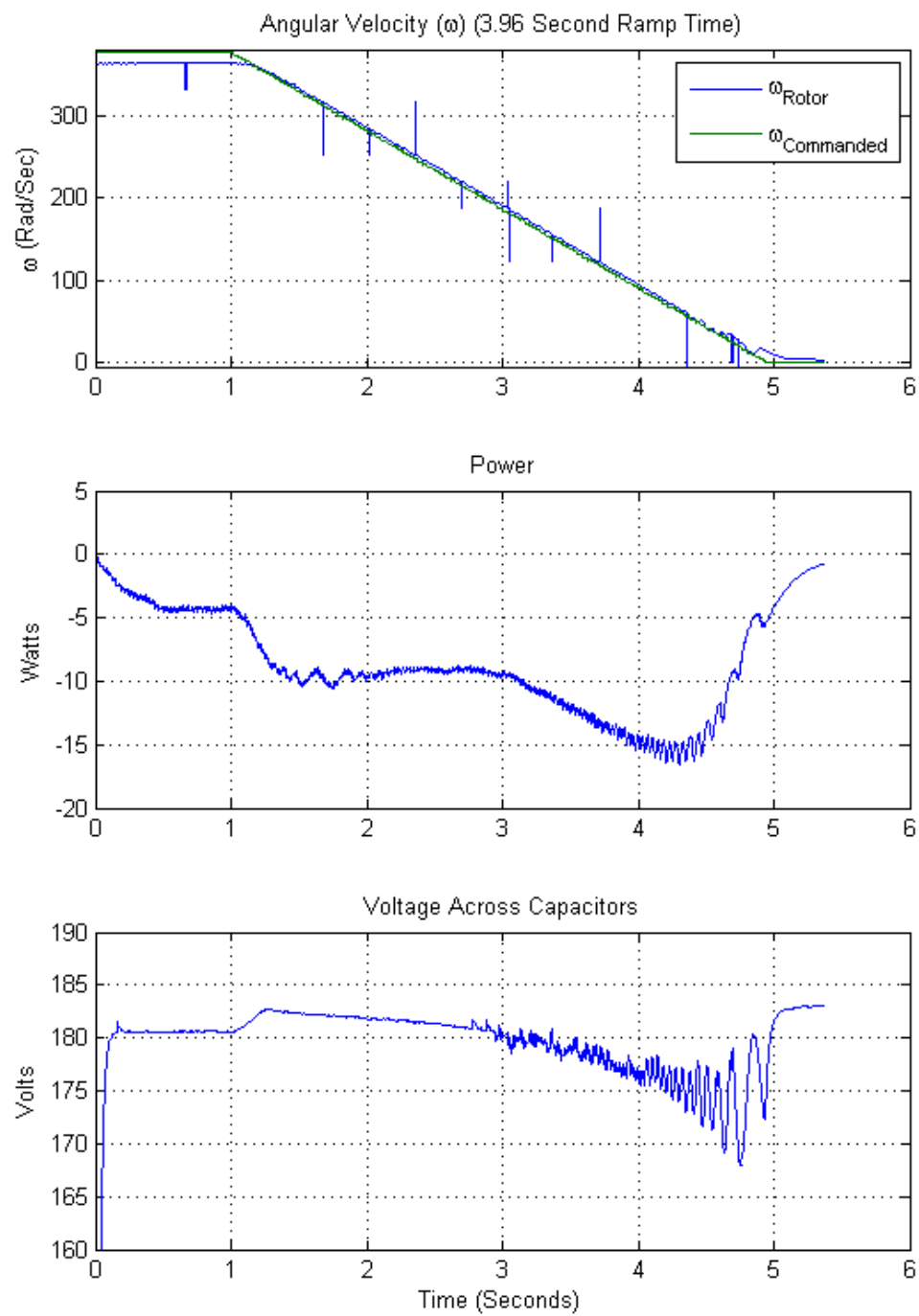


Figure 36. Experiment 4 Results

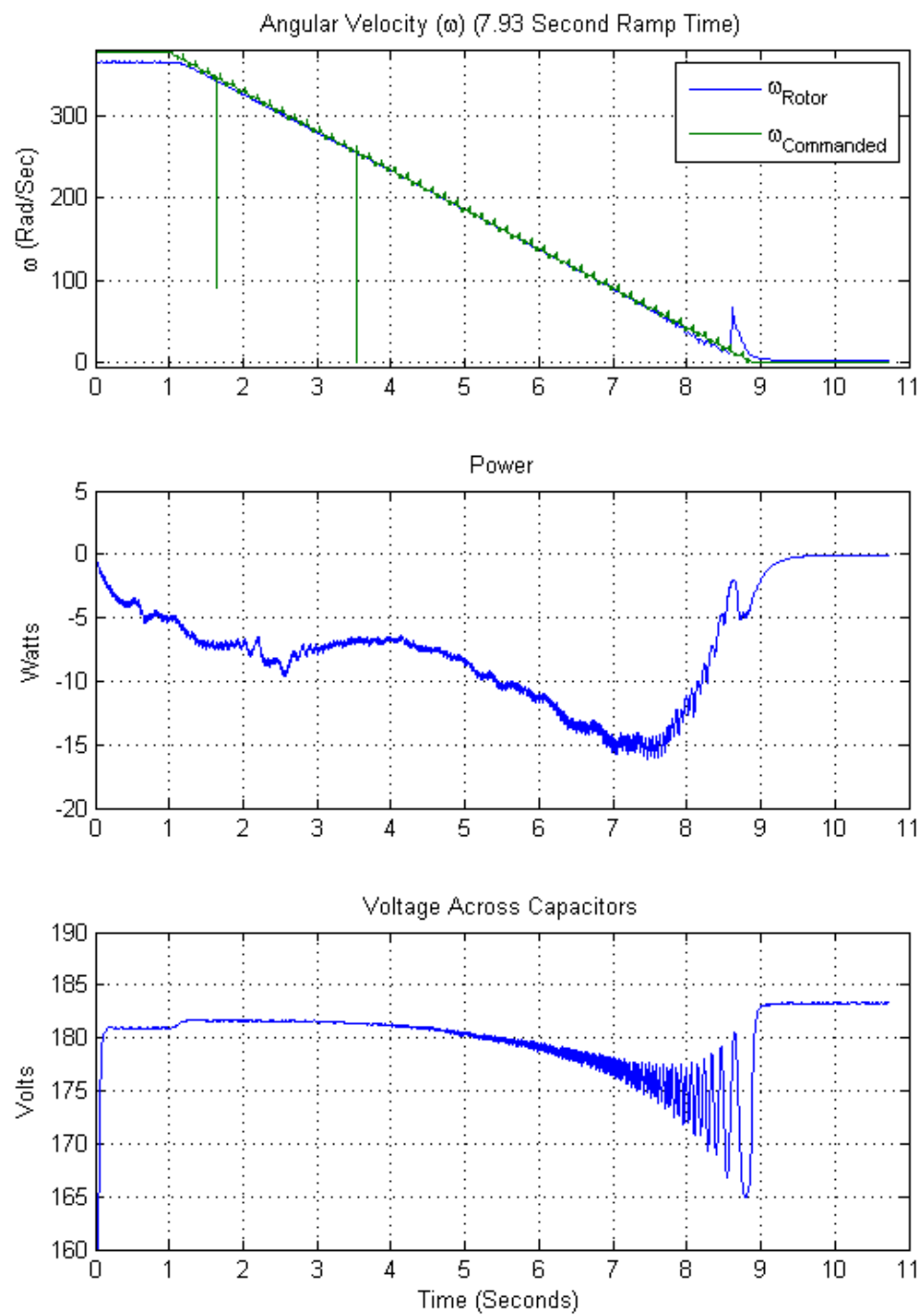


Figure 37. Experiment 5 Results

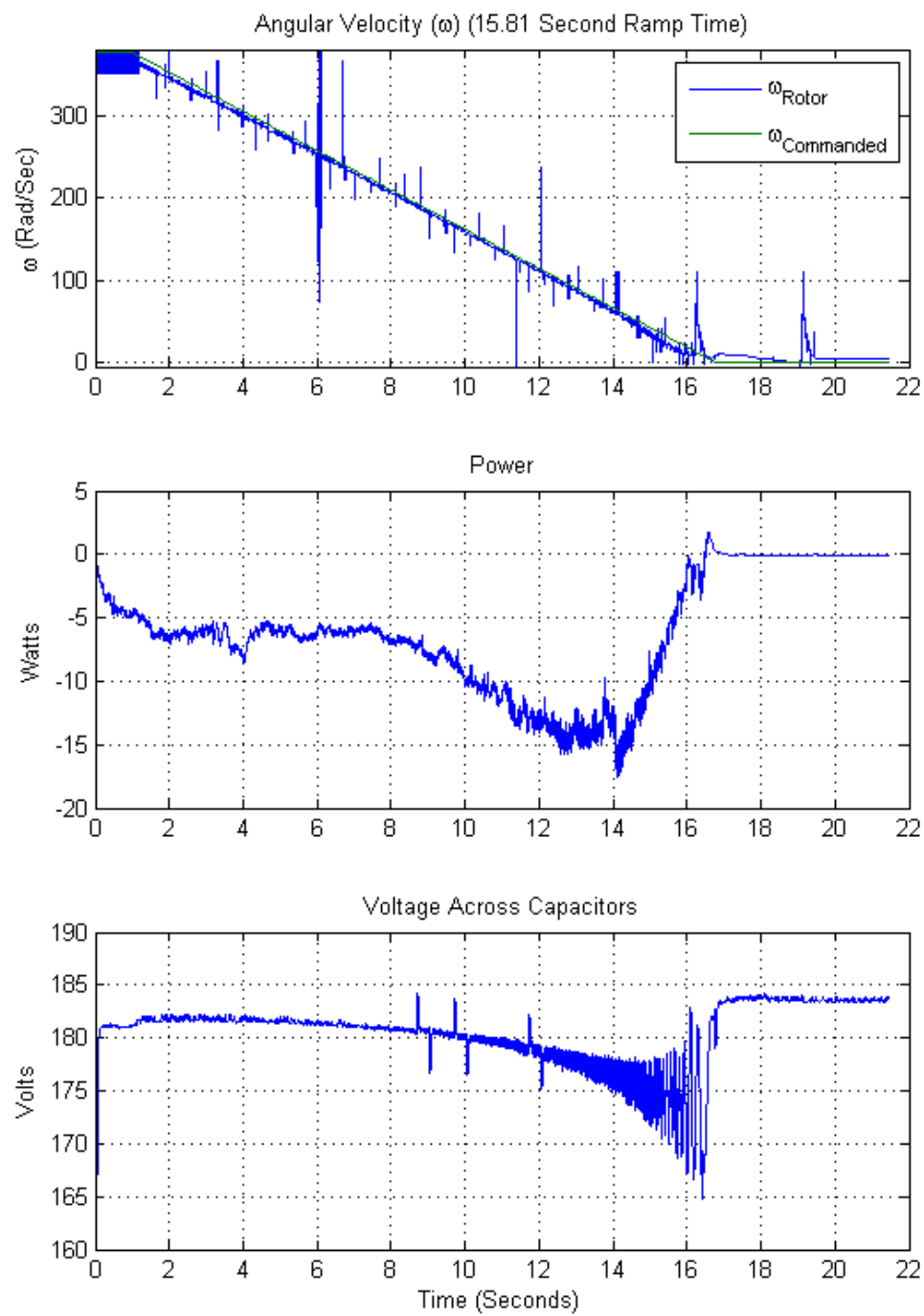


Figure 38. Experiment 6 Results

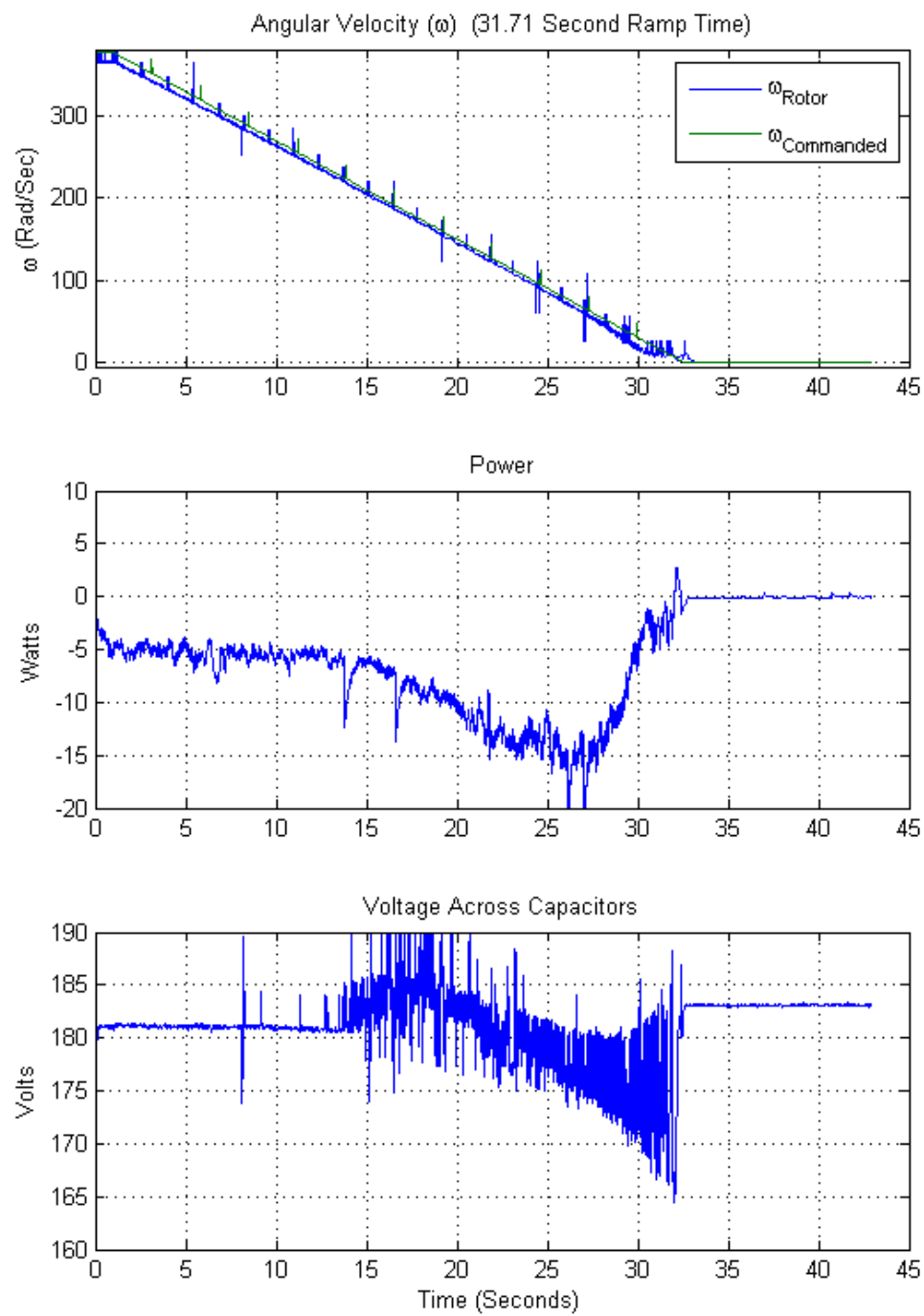


Figure 39. Experiment 7 Results

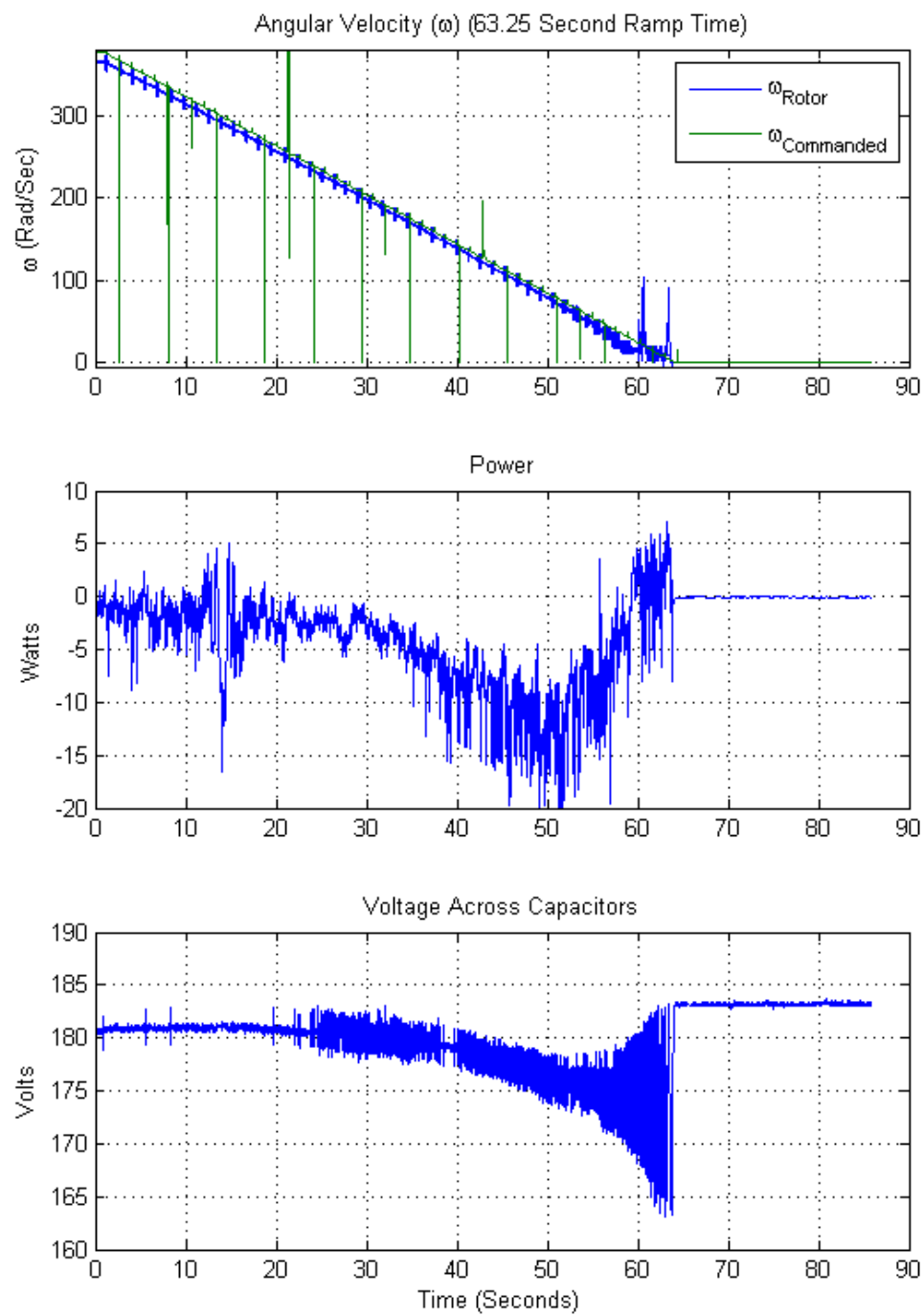


Figure 40. Experiment 8 Results

B. EXPERIMENT COMPARISON ANALYSIS

Figures 41 through 47 contain the comparison graphs of two experiments that are either half or double the deceleration rate of each other. Generally, the Angular Velocities Graphs of the Figures displayed the rate of deceleration of the rotor followed closely to the commanded rate of deceleration as discussed in the previous section. The differences in actual rotor velocity and commanded angular velocity generally go from a negative slip value to a positive slip with decreasing deceleration rates.

The power plots for all of the experiments were similar to one another. The peak negative value for power became more positive as deceleration rate decreased where the largest value was approximately negative thirty Watts for Experiment 1. In the plots for Experiments 2 through 8, power approached negative fifteen Watts. All power plots for each experiment show evidence of regenerative braking occurring for all deceleration rates.

In Experiments 1 through 7, there was a voltage peak across the capacitor bank of the power inverter in descending values as deceleration rates decreased. In Experiment 8, the voltage across the capacitor bank dropped until the braking event was over. This was caused by the power consumed due to the power electronics of the inverter being greater than the power generated from the motor.

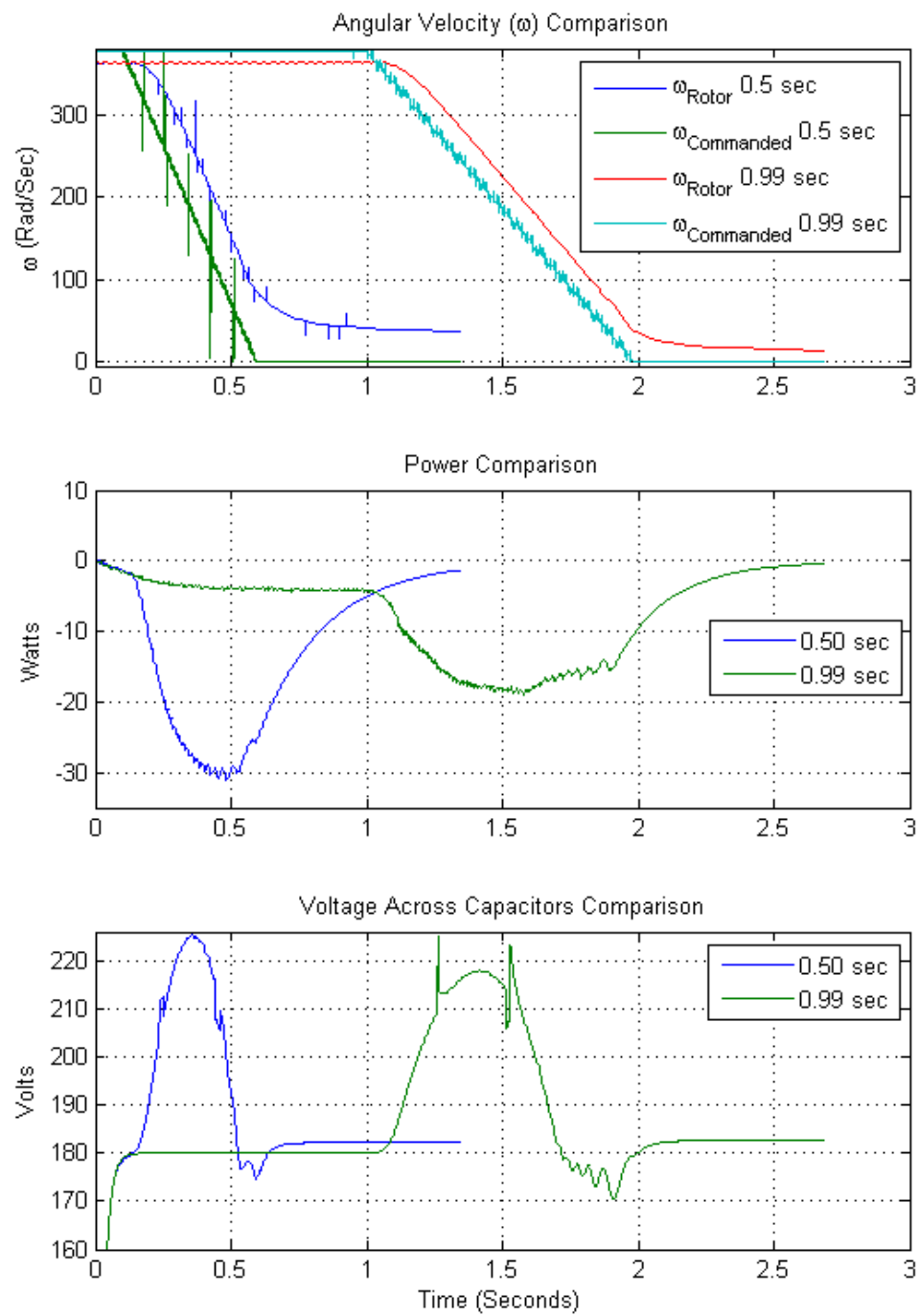


Figure 41. Experiments 1 and 2 Comparison

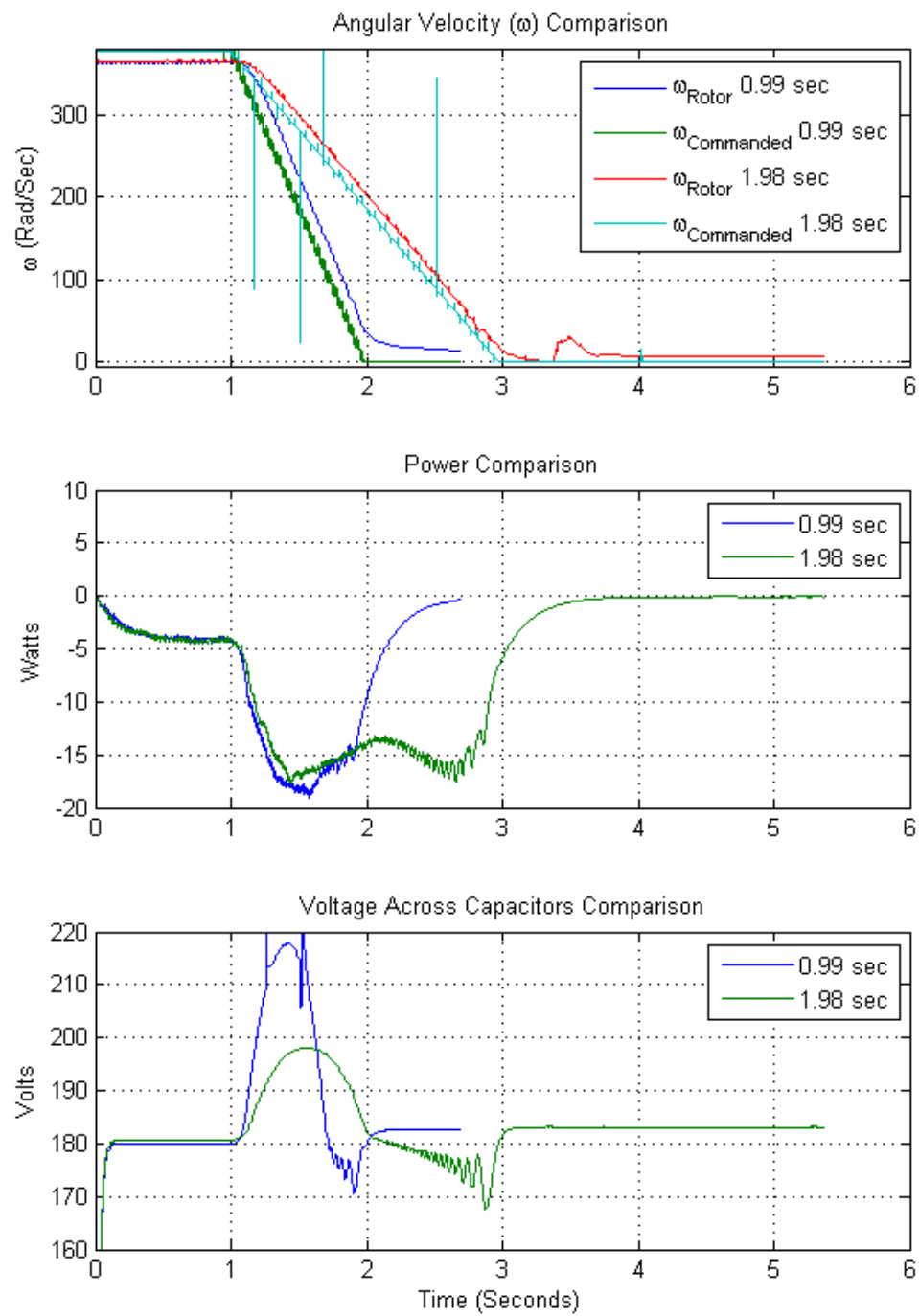


Figure 42. Experiments 2 and 3 Comparison

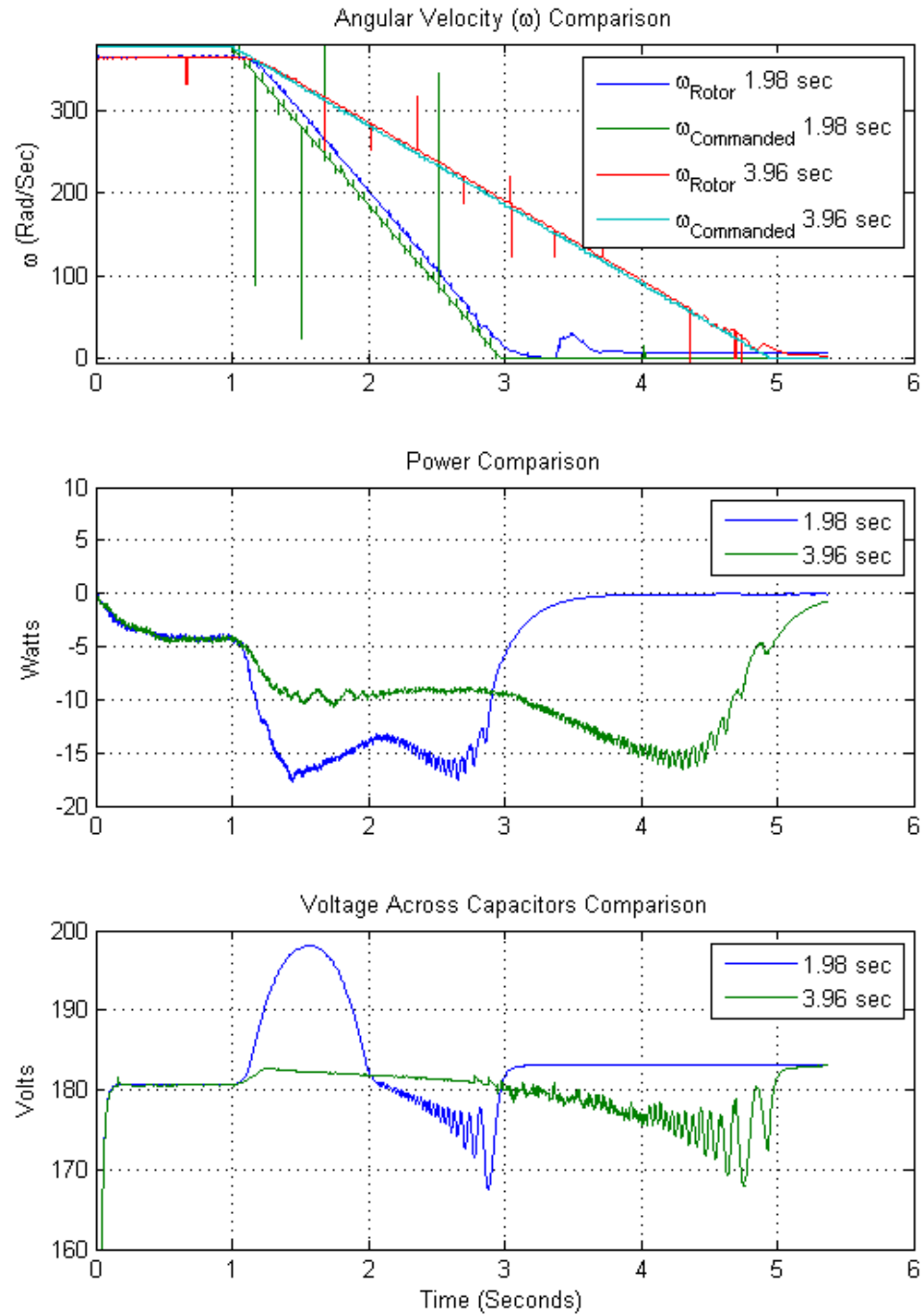


Figure 43. Experiments 3 and 4 Comparison

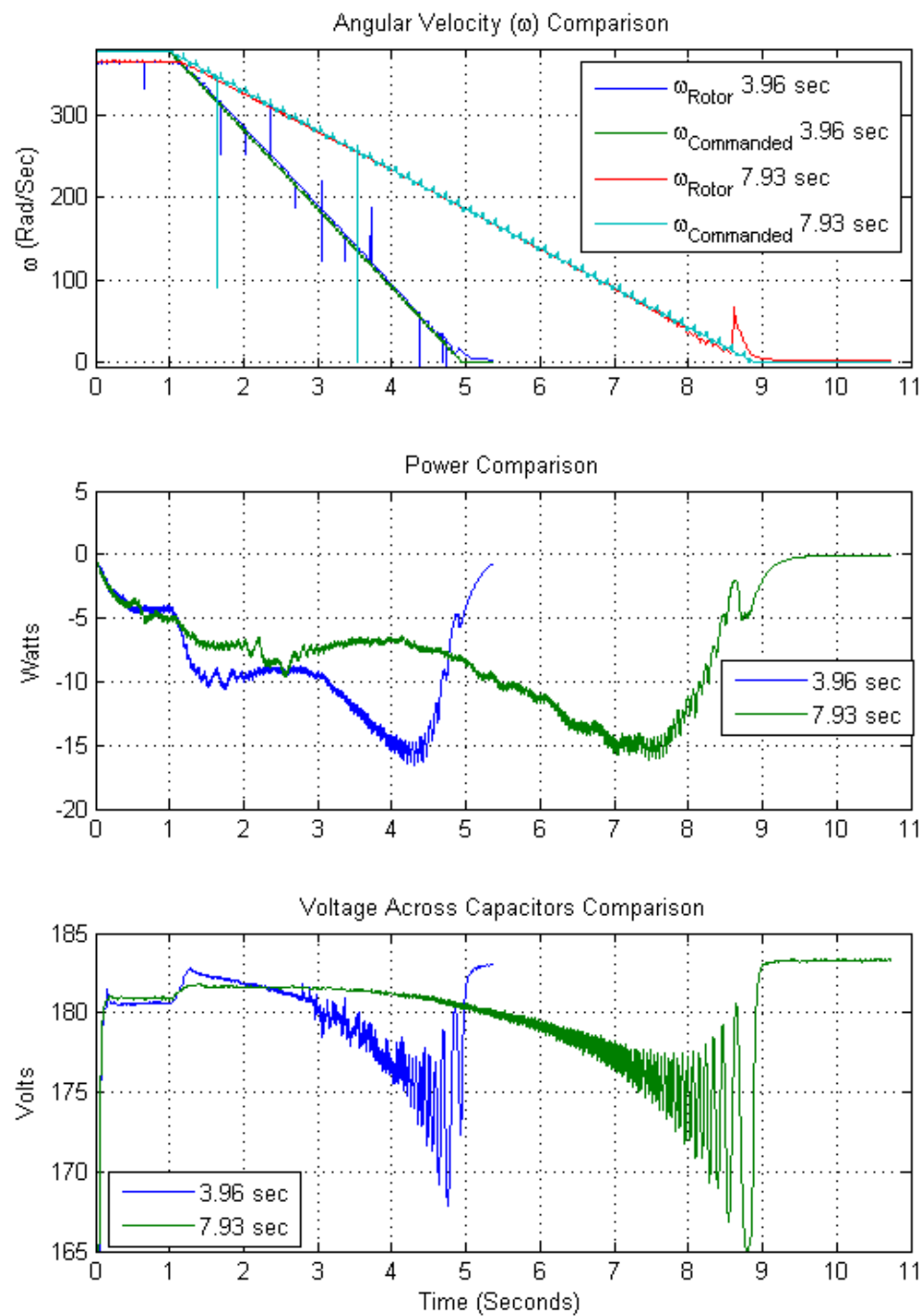


Figure 44. Experiments 4 and 5 Comparison

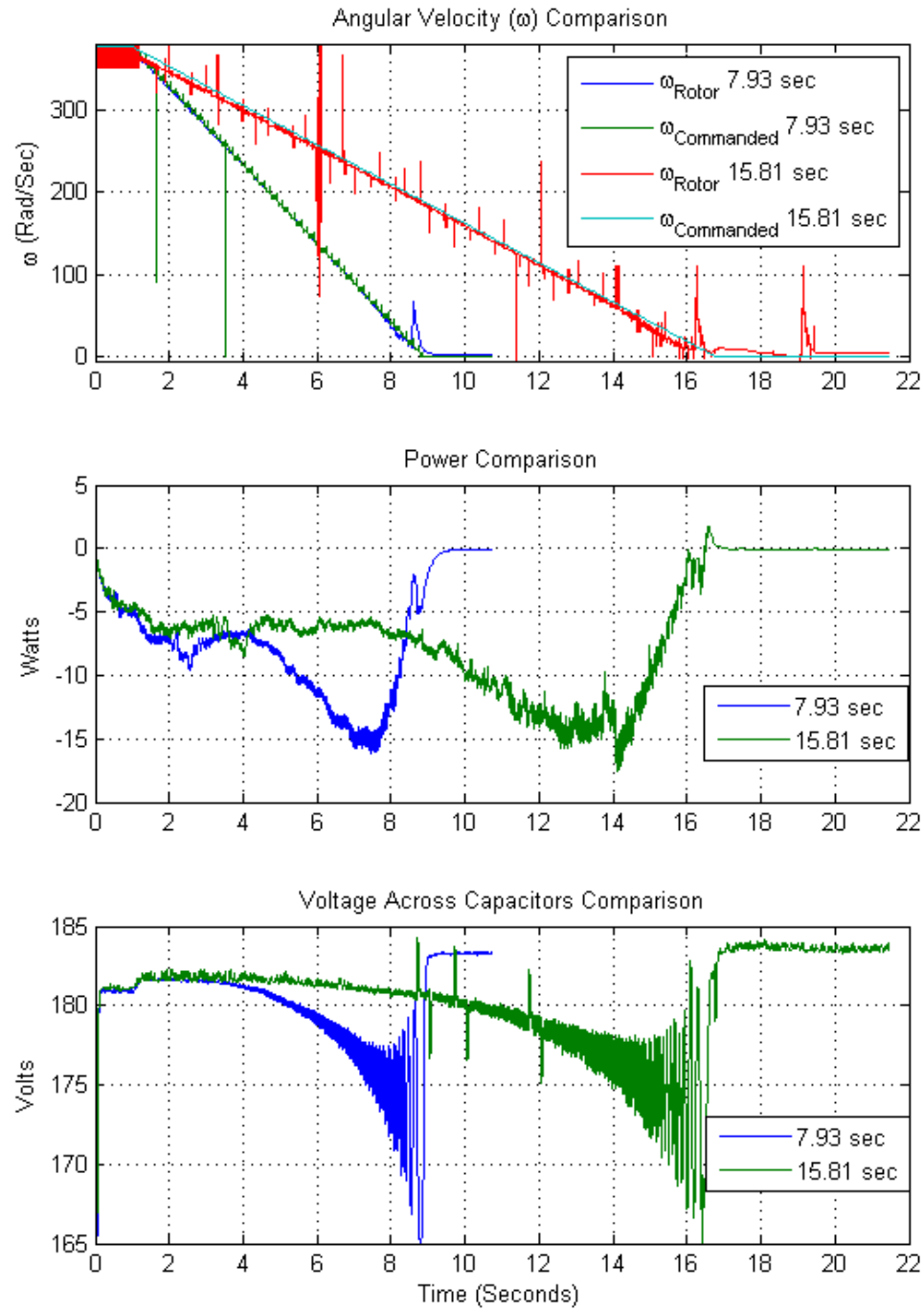


Figure 45. Experiments 5 and 6 Comparison

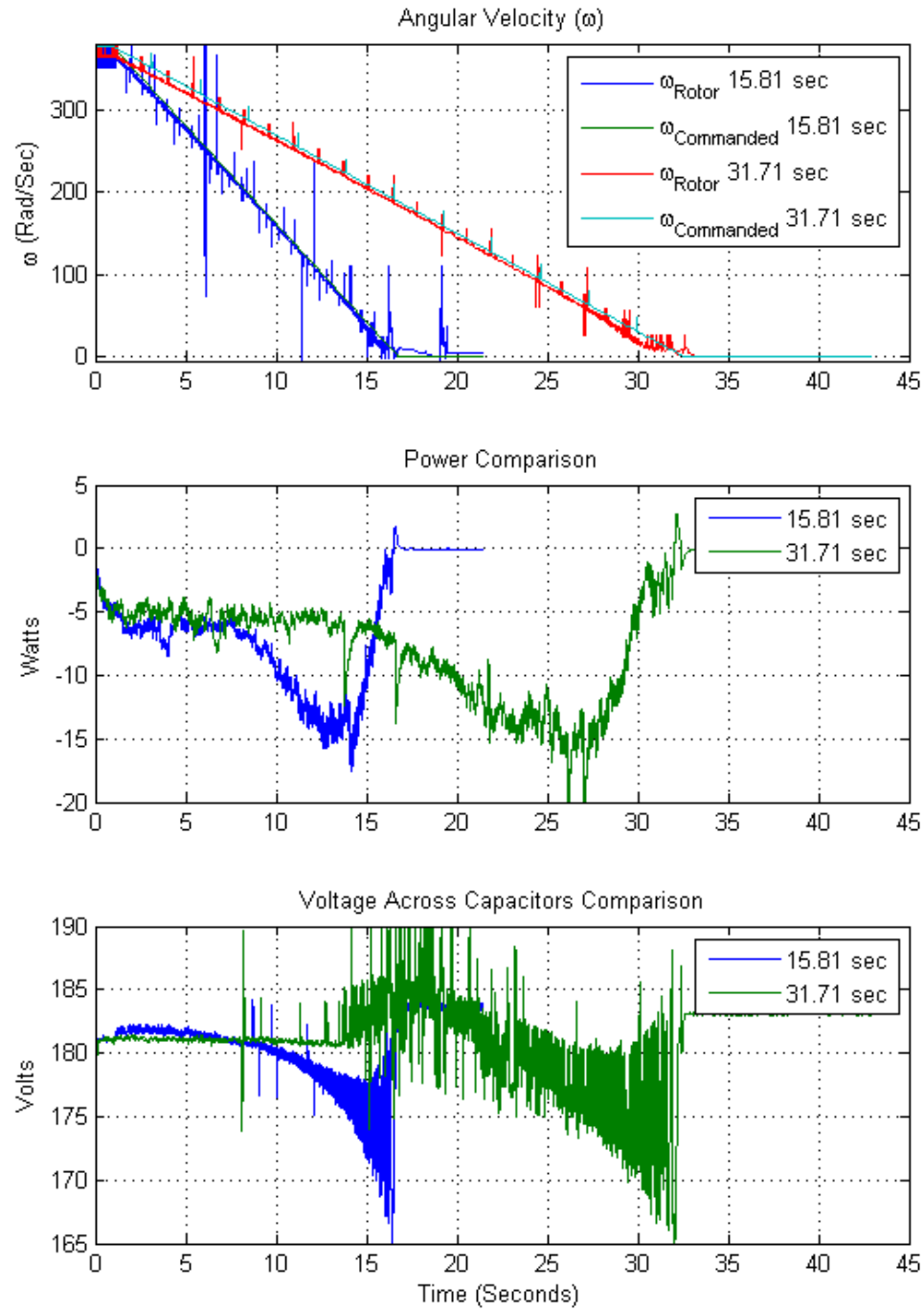


Figure 46. Experiments 6 and 7 Comparison

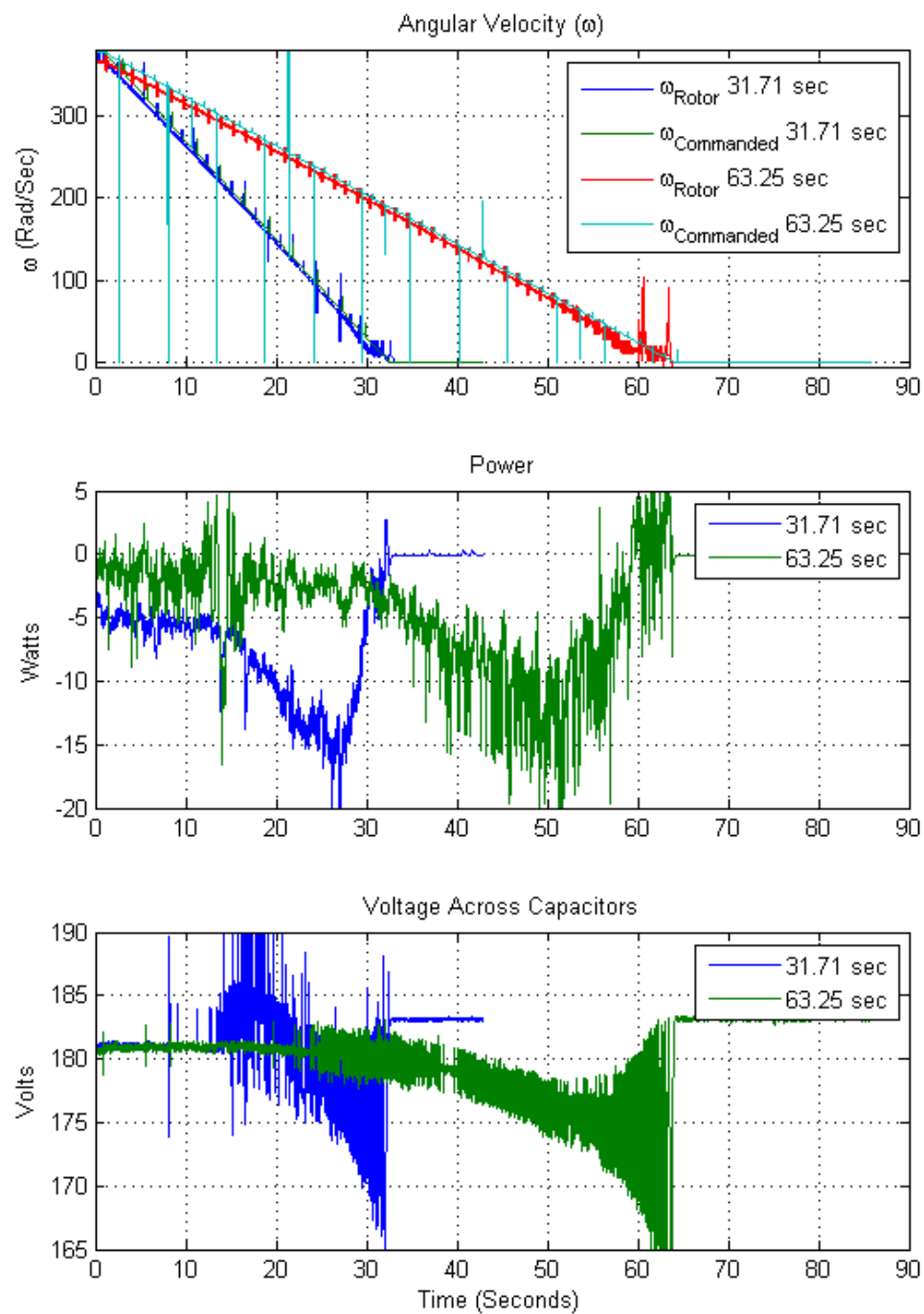


Figure 47. Experiments 7 and 8 Comparison

C. ANGULAR VELOCITY DIFFERENCE ANALYSIS

Figures 48 through 55 contain the Angular Velocity Difference plots which existed between commanded and actual angular velocities of the experiments. A positive angular velocity difference depicts when the commanded velocity is greater than the actual rotor velocity. The opposite holds true for a negative velocity difference. Generally, these plots go from more negative angular velocity difference to more positive angular velocity difference as the deceleration rates decrease. The angular velocity differences approached a value of six radians per second as deceleration rates decreased.

The power plots for all of the experiments are roughly the same with the respect to power following the angular velocity difference plots. The power was at maximum negative value when the angular velocity difference was held constant at the minimum value for the longest length of time. This was where most of the energy was recovered in the experiments. At the end of each event for all the experiments the differences in angular velocity became more positive than the minimum value. At this point in time power seemed to be at maximum negative value.

In all of the experiments, the voltage across the capacitors was at maximum value at the point in time when the angular velocity difference became a constant minimum value. Voltage also followed power at the end of the braking event.

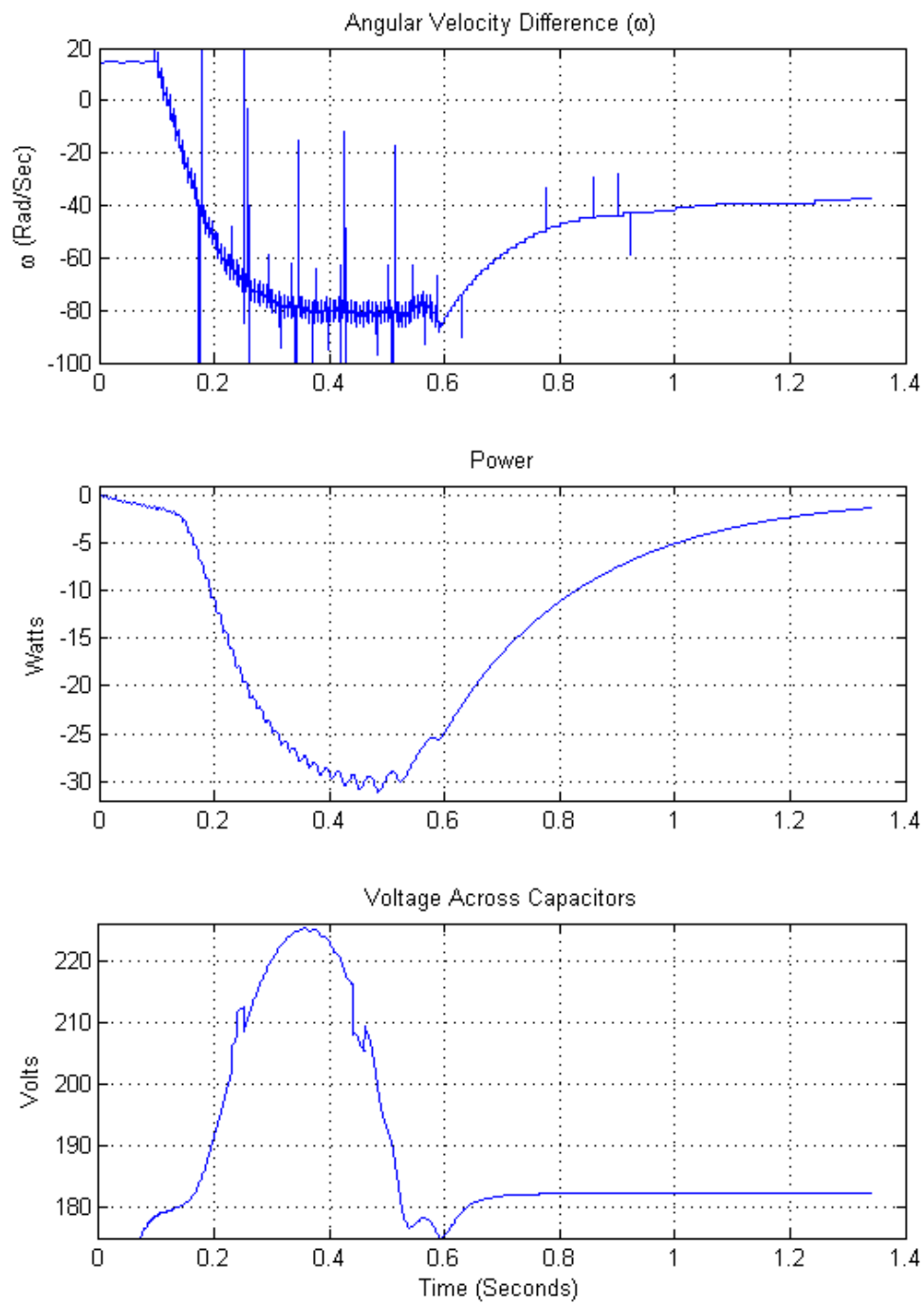


Figure 48. Experiment 1 Velocity Difference Analysis

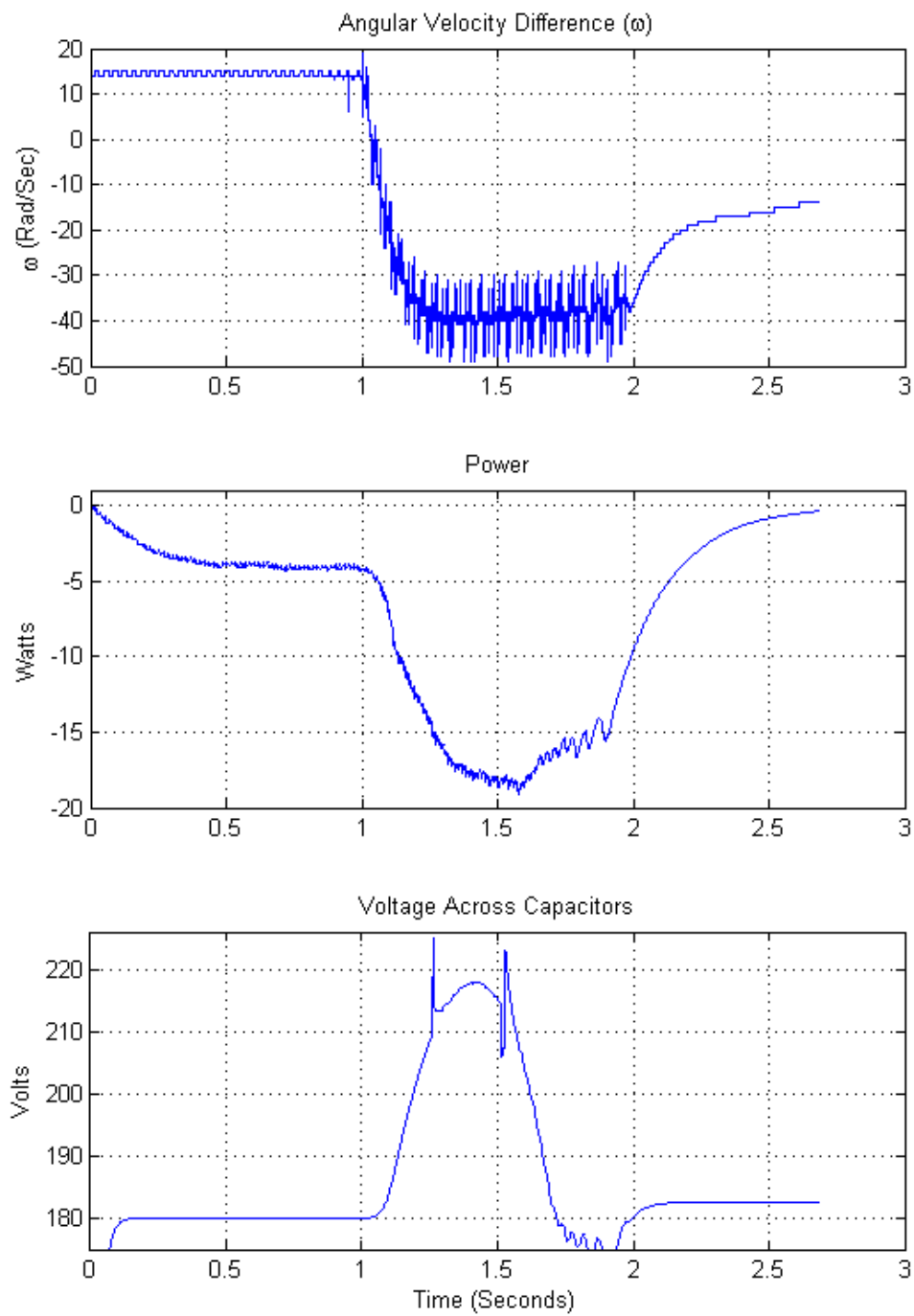


Figure 49. Experiment 2 Velocity Difference Analysis

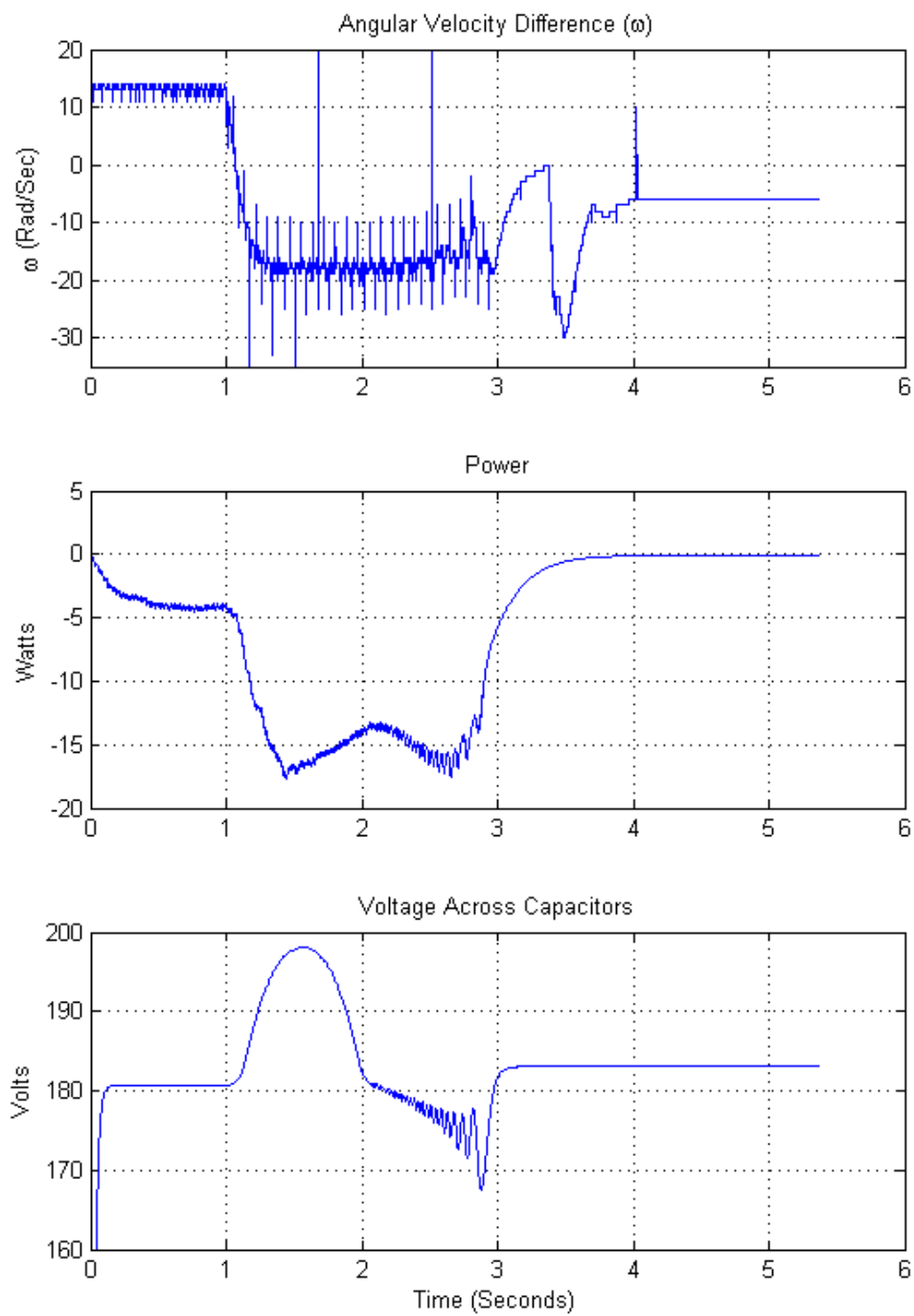


Figure 50. Experiment 3 Velocity Difference Analysis

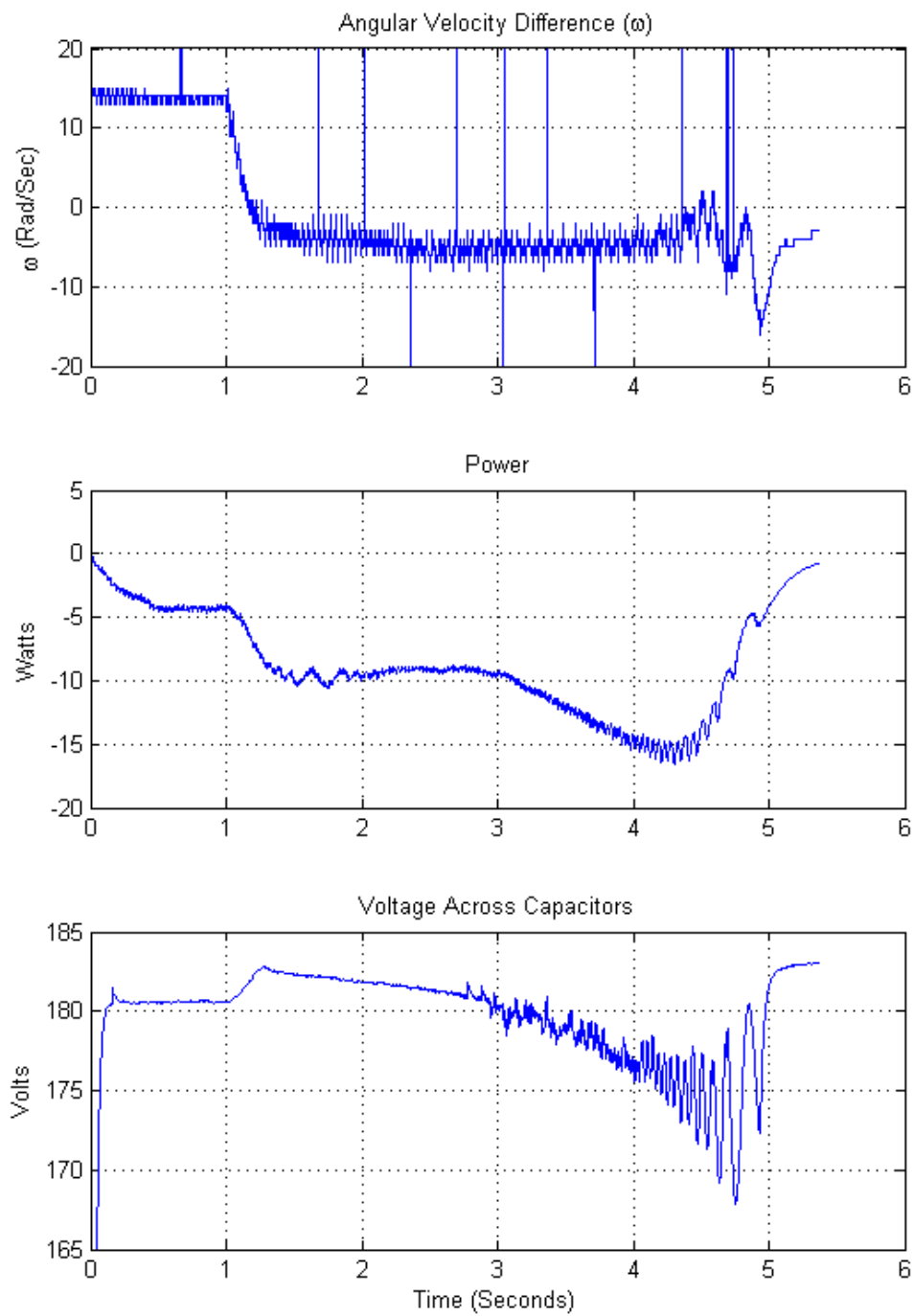


Figure 51. Experiment 4 Velocity Difference Analysis

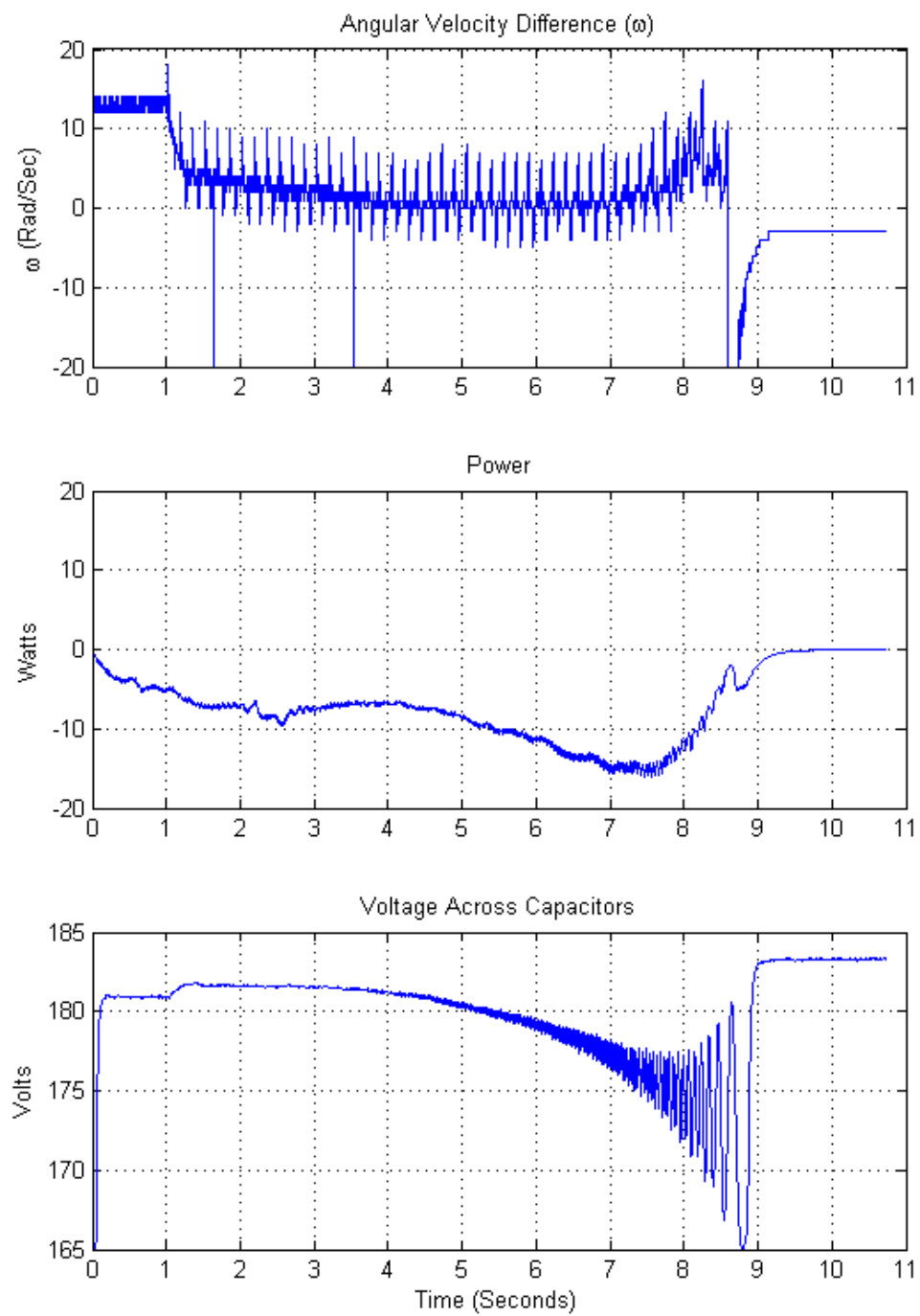


Figure 52. Experiment 5 Velocity Difference Analysis

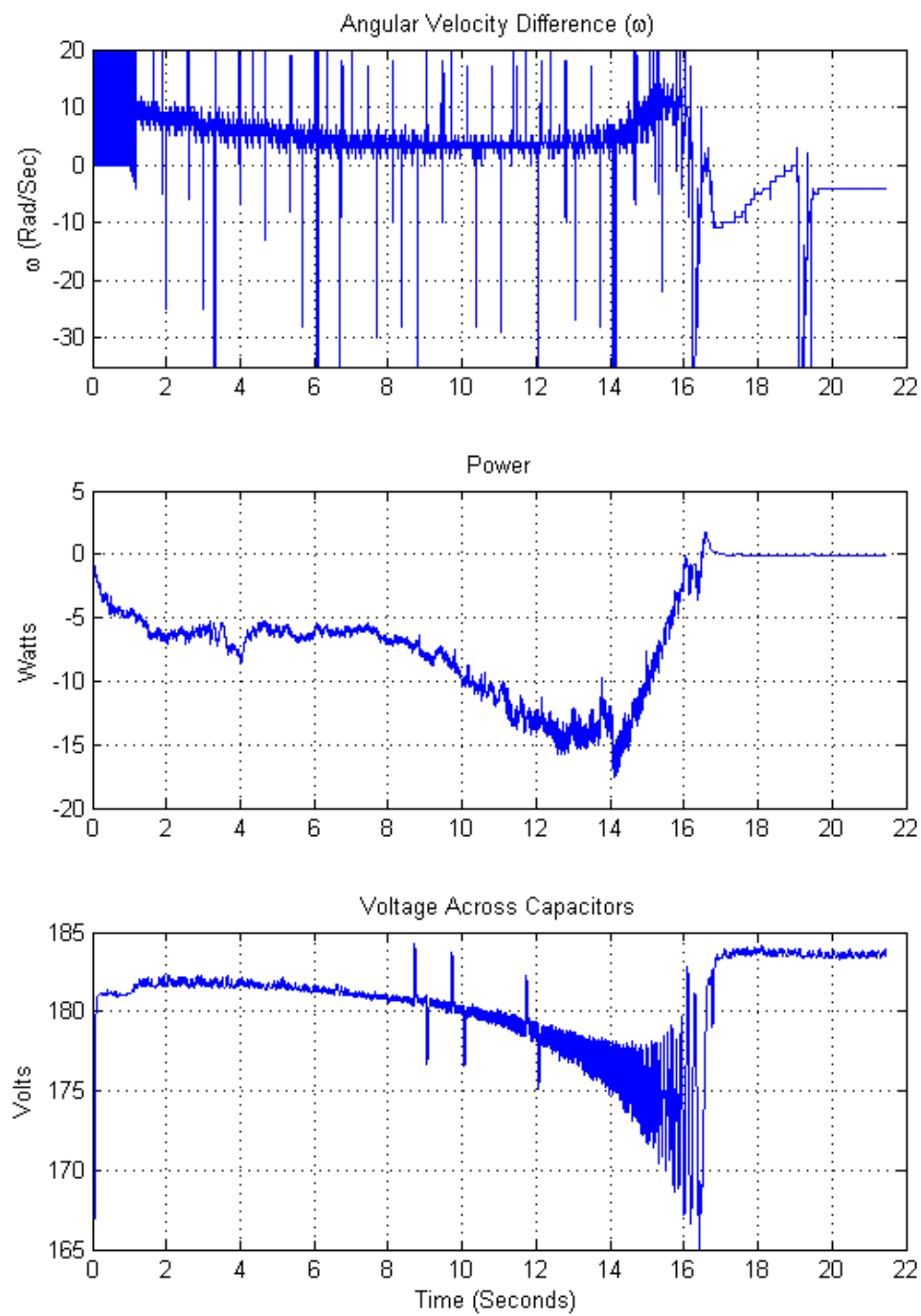


Figure 53. Experiment 6 Velocity Difference Analysis

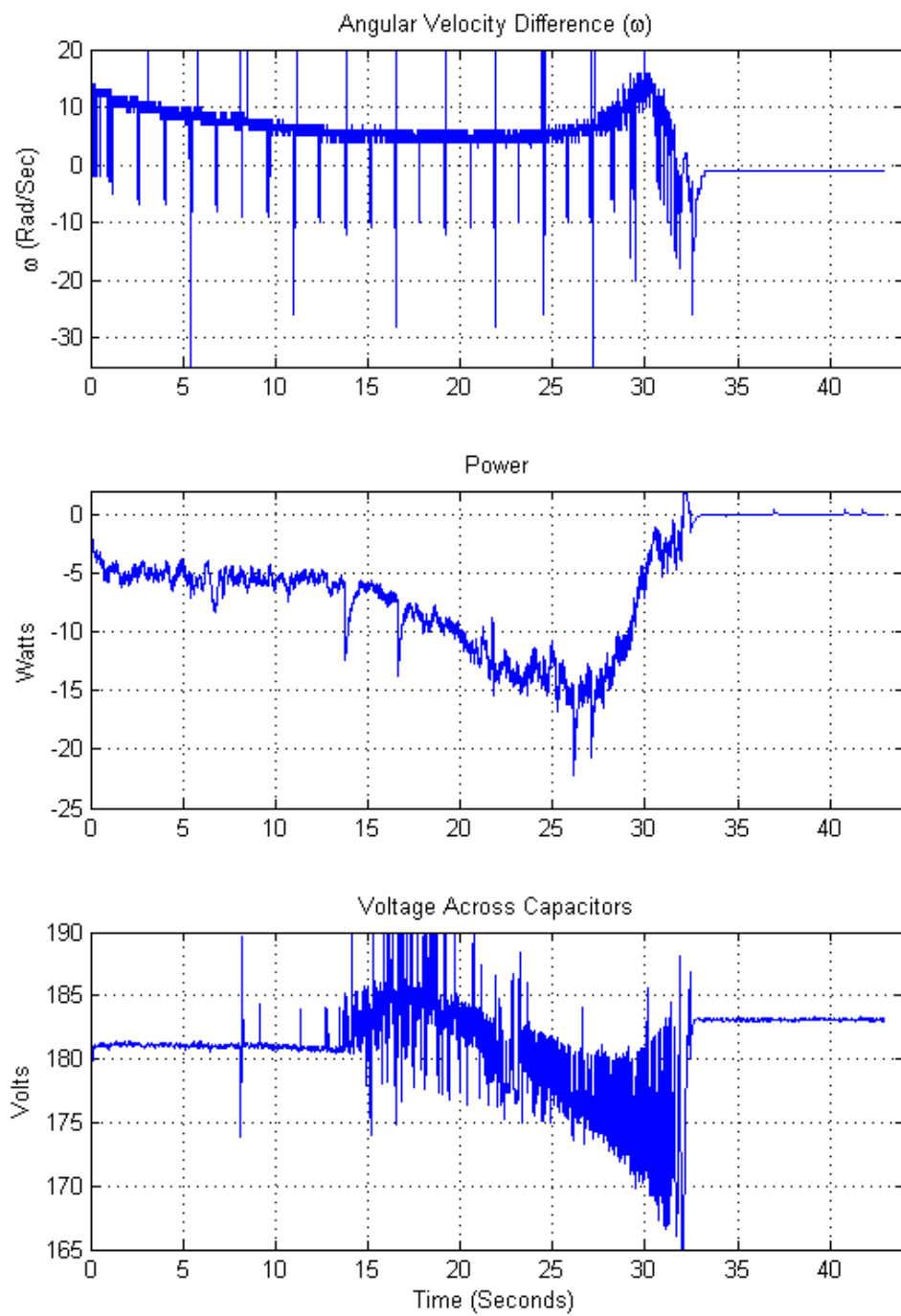


Figure 54. Experiment 7 Velocity Difference Analysis

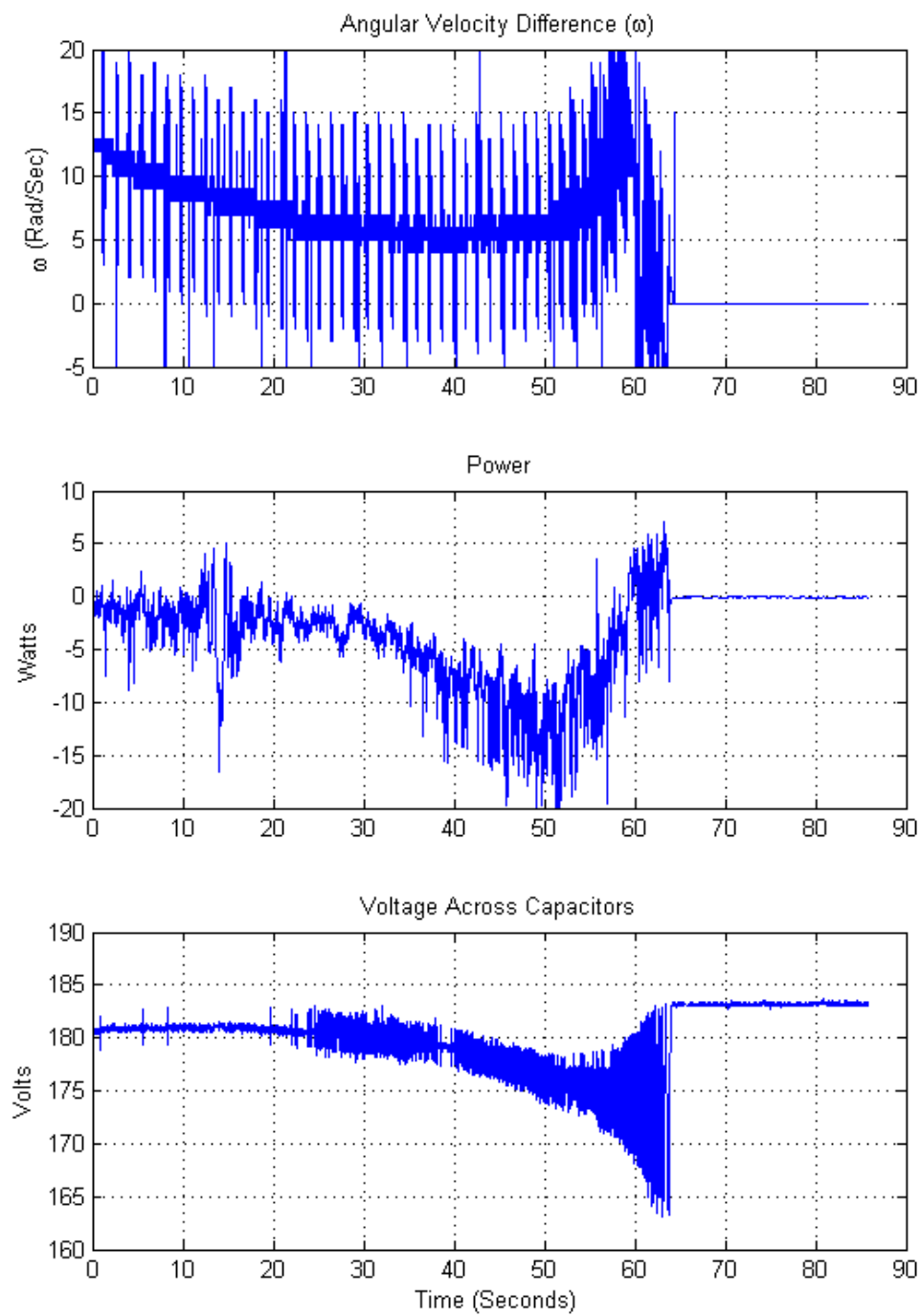


Figure 55. Experiment 8 Velocity Difference Analysis

D. PHASE A CURRENT BEHAVIOR ANALYSIS

In this analysis, Phase A, current behavior, was observed to draw conclusions of the dynamics that occurred during the regeneration events of Experiments 1 and 2. To capture the current data a separate trial had to be performed for each deceleration rate, since the number of A/D converter channels required were less than the A/D converter channels available. The Regenerative Power displays in these figures were all converted to positive values to allow for a better comparison between the I^2R losses and the power generated.

From Figures 56 through 57, it was apparent that the magnitude of the current increased as soon as the motor braking event was initiated. The frequency of the current signal decreased as the rotor velocity decreased. The current also went to zero as soon as commanded velocity went to zero. The power was more affected by the slower rotor velocities and was related to the increased magnitude of current. This was expected as demonstrated earlier in the power calculation methods. Current is proportionally related to power. Both the I^2R loss and power recovered plots are very similar, but there was less I^2R losses in the first half of the braking event. The power generation occurred more in the first half of the braking event. In Experiment 3, there is a dip in the power generation plot halfway through the braking event. This happened due to the minor oscillation of the rotor's deceleration rate at that time.

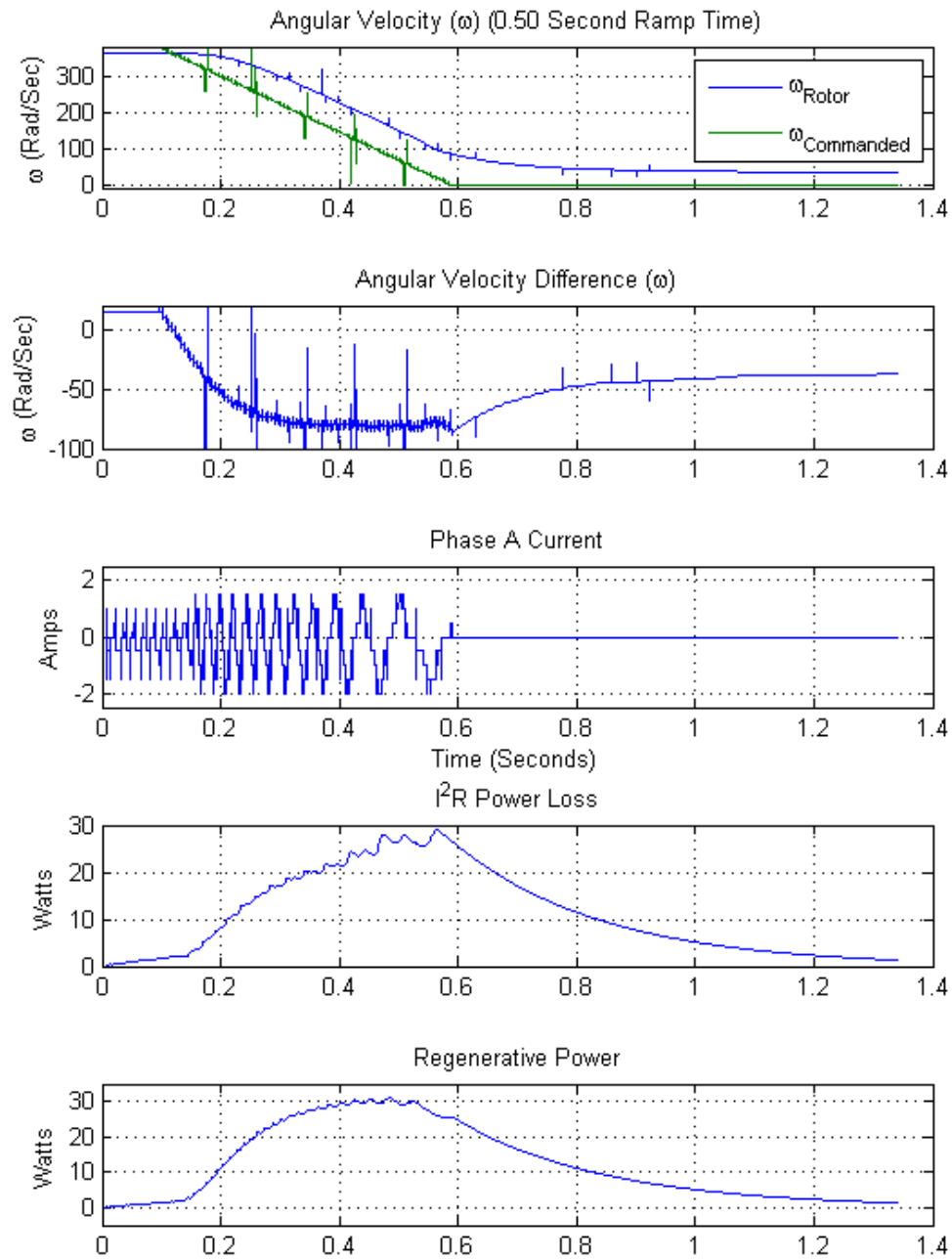


Figure 56. Experiment 1 Current Behavior Analysis

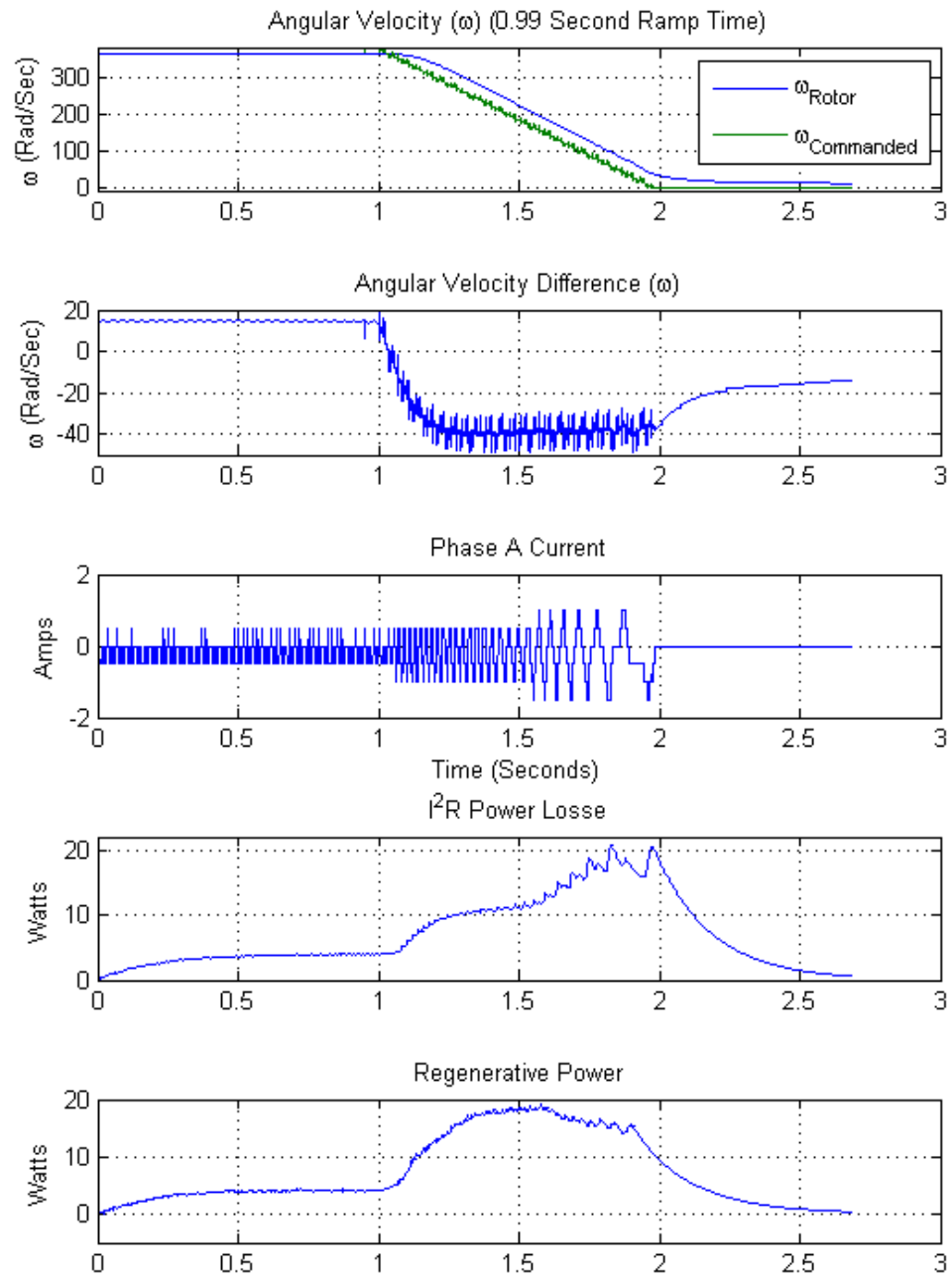


Figure 57. Experiment 2 Current Behavior Analysis

E. ENERGY ANALYSIS

In this analysis, the energy induced and lost during each experiment will be compared to the theoretical value calculated earlier in this thesis. This section only analyzed the data produced during the deceleration of the motor for each experiment. The pre-deceleration and post deceleration data was omitted to allow for energy summations. The Simulink model used to integrate power for both experiments is contained in Appendix F.

The internal resistance of the motor was measured to be 12 ohms. The current flowing through this resistance accounts for the heat energy dissipated, and is known as I^2R losses. Figures 58 and 59 are the resultant energy levels per unit time for both I^2R energy lost and energy recovered. Table 3 contains the results for each experiment. The rate of energy lost due to the motor's internal resistance was relatively the same rate as the energy recovered for Experiments 1 and 2. The total energy of the two experiments did not equate to the final values measured from the experiments. Both experiments have relatively the same percent error. Both experiments still had energy stored in the rotor's moment. There are other energy sinks that were not accounted for since they were not measured. One energy sink might be magnetic leakage as this term is part of the equations that describe the induction motor, as discussed in the theory section of this thesis. Another reason for the total energy difference could be due to calibration errors within the equipment used to take measurements during the experiments.

Table 3. Energy Analysis

Experiment #	Energy (Joules)						% Error
	Lost	Recovered	In Rotor	Total	Theoretical	Difference	
1	8.7	10.6	7.5	26.8	31.2	4.4	14.0
2	11.8	14.3	1.5	27.6	31.2	3.6	11.6

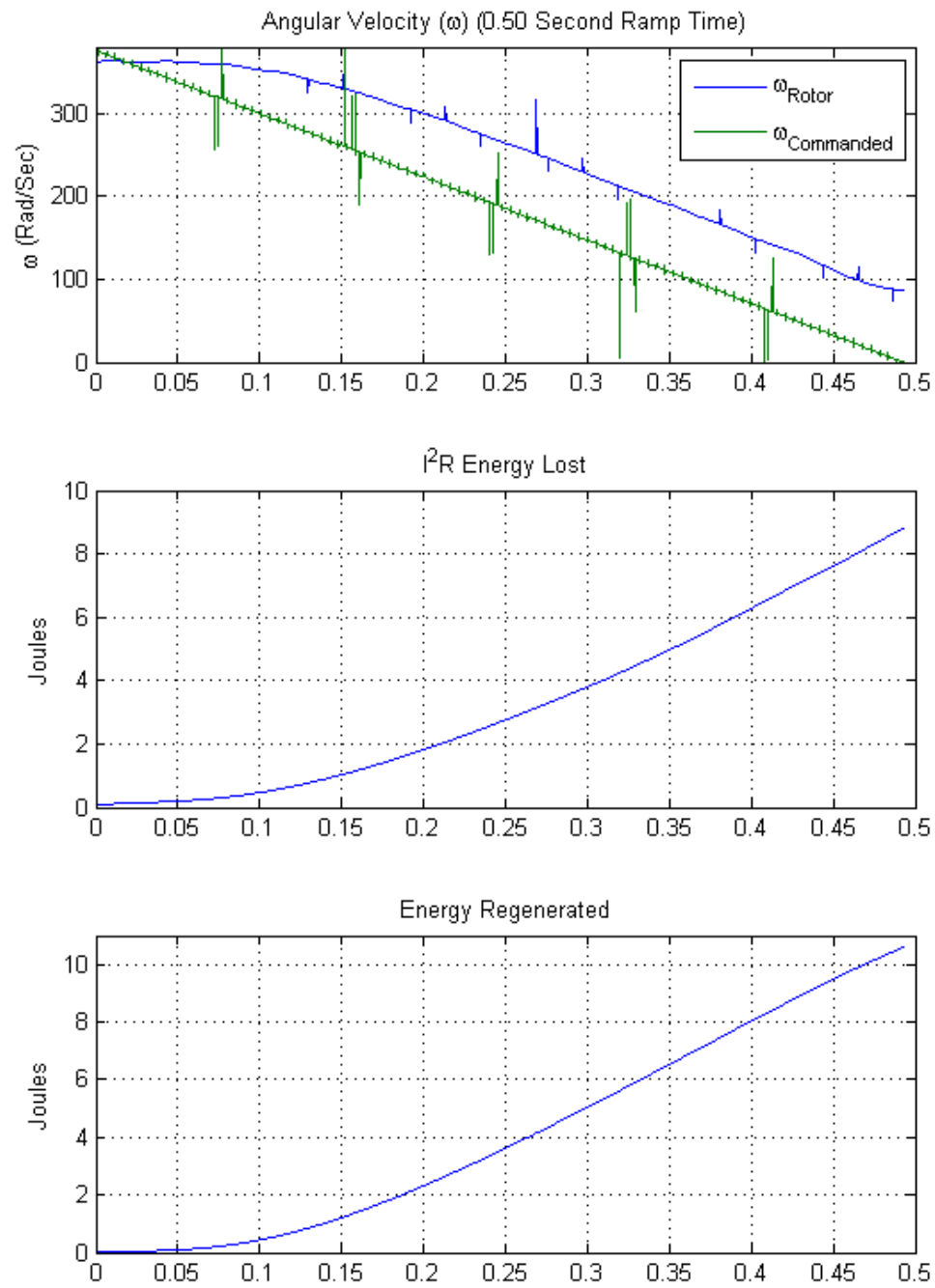


Figure 58. Experiment 1 Energy Analysis

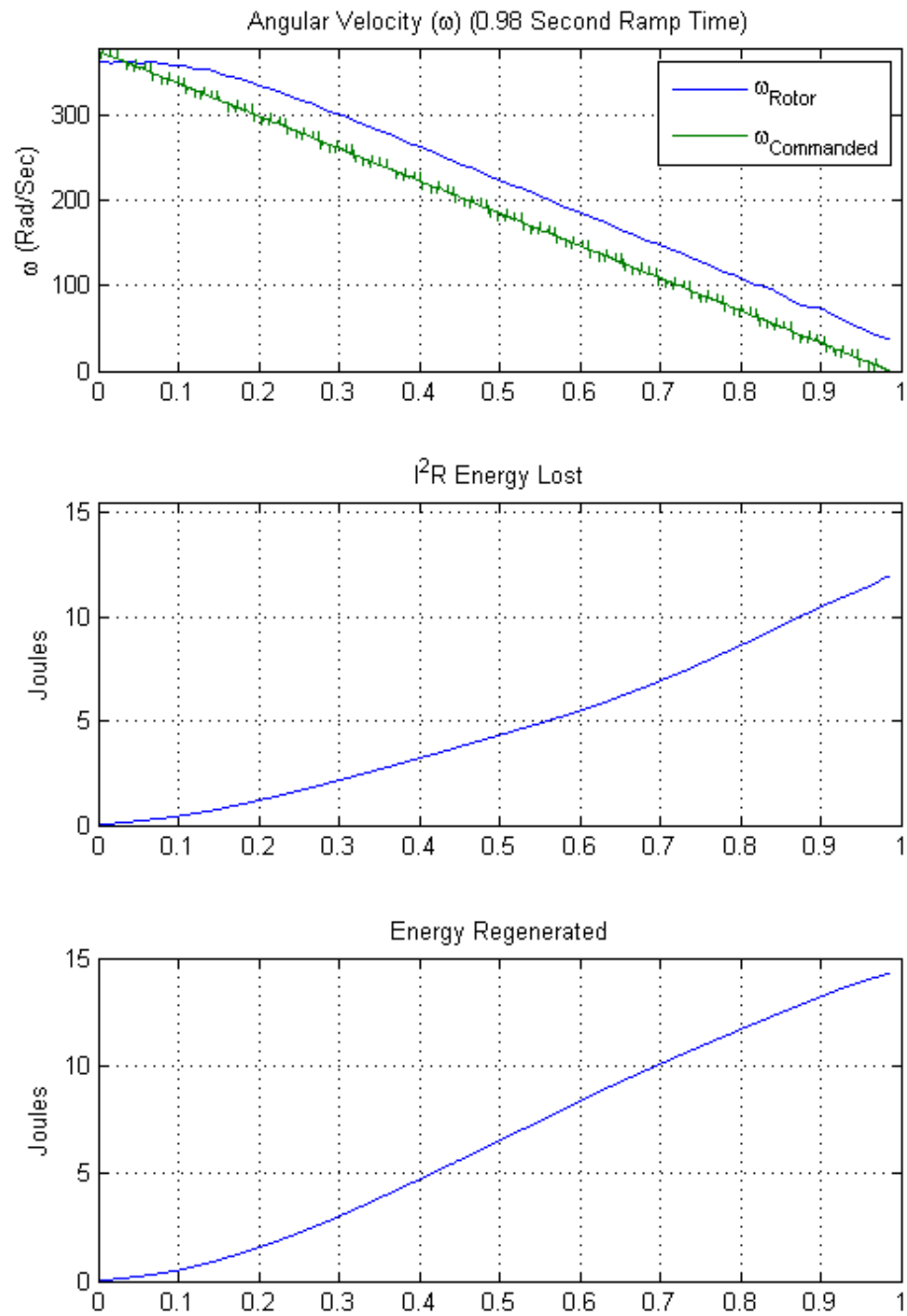


Figure 59. Experiment 2 Energy Analysis

THIS PAGE INTENTIONALLY LEFT BLANK

V. CONCLUSION AND FUTURE RESEARCH RECOMMENDATIONS

A. CONCLUSION

This thesis explored ideas in which the USN can benefit from energy recovery systems that implements regenerative braking technologies. It also provided a historical background and motivation for the development of regenerative braking. This was to provide the reader knowledgeable insight of a hundred year old technology that is now a reality in our daily activities. The theory of symmetrical, asynchronous induction motors was presented to provide a mathematical background for modeling regenerative braking. Also, within this thesis, the experiment's preparation and model setup was covered. From the results, regenerative braking had occurred and was demonstrated through the analysis of the plots produced from the waveforms of various parameters monitored during the experiment. Energy conservation was also presented to further elaborate the evidence of the energy produced through regenerative braking.

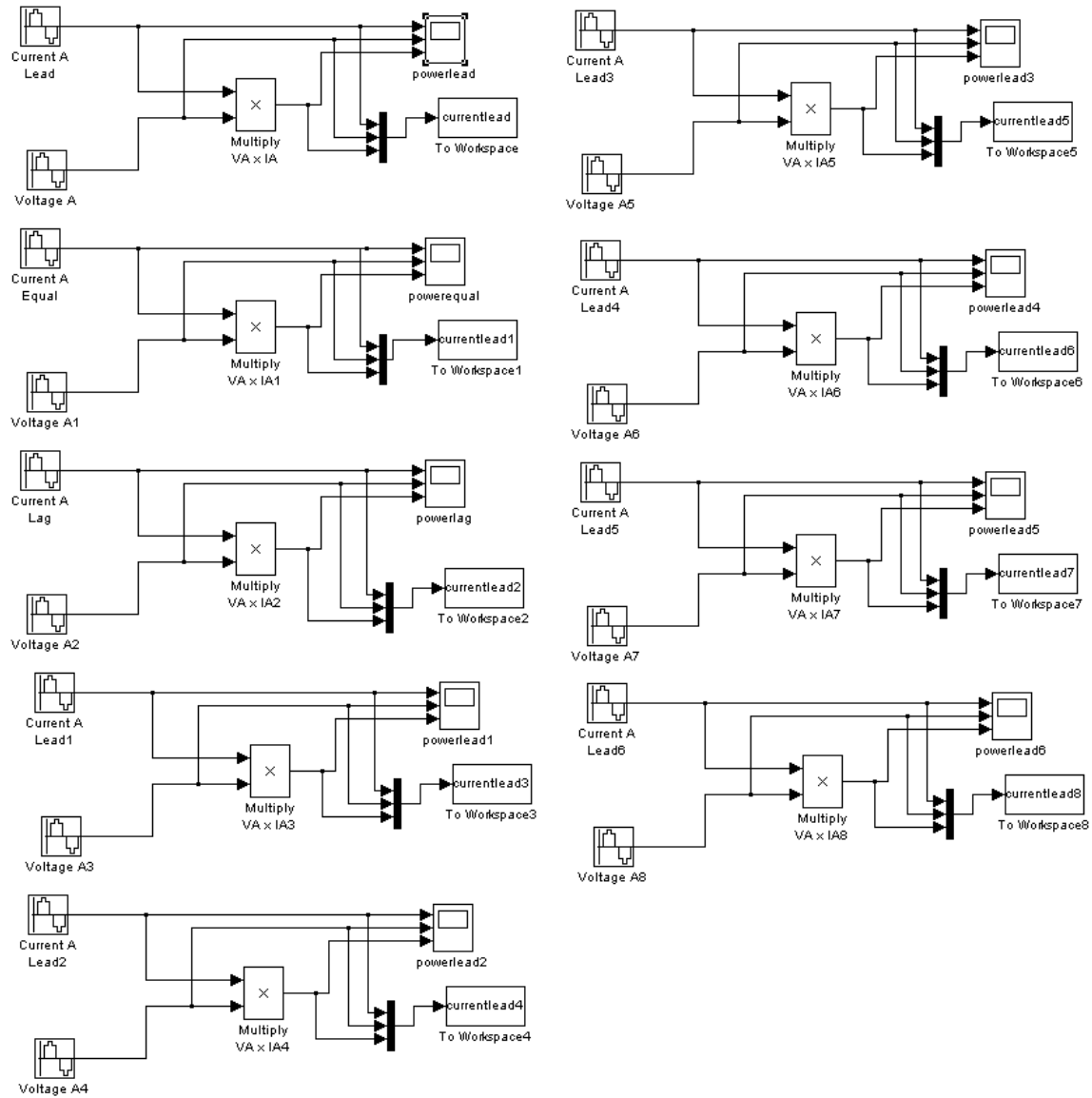
B. FUTURE RESEARCH RECOMMENDATIONS

The data gathered during the experiments show that many opportunities exist to fully understand and improve on regenerative technology. The plots displayed noise interference, which made analysis of the data difficult. An opportunity exists where research in locating and eliminating the noise from the motor to the computer terminal would greatly benefit future research experiments. Research may be conducted in controlling the waveform of power as the motor brakes to maximize power output of the regeneration. Also, minimizing the power lost due to internal resistances can benefit future research. There are potentially many opportunities to understand the dynamics that occur within the power inverter, which controls motor speed during regeneration. Voltage plots in Experiments 1 through 3 displayed spikes that seemed symmetrical on either side of the maximum value in the graphs. A thesis topic could be performed to understand the causes of these spikes and to understand how the spikes affect

regeneration operations. Research could be performed to understand the minimum deceleration rate to achieve regeneration, or research could explore the simulation of the experiments performed in this thesis to predict the waveforms created, and to compare the results.

APPENDIX A: SIMULINK MODELS AND MATLAB CODE USED TO GENERATE FIGURES 3 THROUGH 12

SimuLink Model to generate waveform output



MATLAB code to generate Figures 3 through 11

```
% Phase Shift Effects on Power
time_1l=0:1/60:50;
figure(1)
plot(time_1l,currentlead(:,1),'--
',time_1l,currentlead(:,2),'g',time_1l,currentlead(:,3),'or');
title('45 Degrees Phase Shift');
legend('Current','Voltage','Power');
xlabel('Time');
ylabel('Amplitude');
figure(2)
plot(time_1l,currentlead1(:,1),'--
',time_1l,currentlead1(:,2),'g',time_1l,currentlead1(:,3),'or');
title('36 Degrees Phase Shift');
legend('Current','Voltage','Power');
xlabel('Time');
ylabel('Amplitude');
figure(3)
plot(time_1l,currentlead2(:,1),'--
',time_1l,currentlead2(:,2),'g',time_1l,currentlead2(:,3),'or');
title('27 Degrees Phase Shift');
legend('Current','Voltage','Power');
xlabel('Time');
ylabel('Amplitude');
figure(4)
plot(time_1l,currentlead3(:,1),'--
',time_1l,currentlead3(:,2),'g',time_1l,currentlead3(:,3),'or');
title('18 Degrees Phase Shift');
legend('Current','Voltage','Power');
xlabel('Time');
ylabel('Amplitude');
figure(5)
plot(time_1l,currentlead4(:,1),'--
',time_1l,currentlead4(:,2),'g',time_1l,currentlead4(:,3),'or');
title('9 Degrees Phase Shift');
legend('Current','Voltage','Power');
xlabel('Time');
ylabel('Amplitude');
figure(6)
plot(time_1l,currentlead5(:,1),'--
',time_1l,currentlead5(:,2),'g',time_1l,currentlead5(:,3),'or');
title('0 Degree Phase Shift');
legend('Current','Voltage','Power');
xlabel('Time');
ylabel('Amplitude');
figure(7)
plot(time_1l,currentlead6(:,1),'--',time_1l,currentlead6(:,2),'g');
title('Leading Condition');
legend('Current','Voltage','Power');
xlabel('Time');
ylabel('Amplitude');
figure(8)
plot(time_1l,currentlead7(:,1),'--',time_1l,currentlead7(:,2),'g');
title('Lagging Condition');
```

```

legend('Current','Voltage','Power');
xlabel('Time');
ylabel('Amplitude');
figure(9)
plot(time_ll',currentlead8(:,1),'--',time_ll',currentlead8(:,2),'g');
title('Zero Phase Shift Condition');
legend('Current','Voltage','Power');
xlabel('Time');
ylabel('Amplitude');

```

MATLAB Code to generate Figure 12

```

% To Demonstrate Power Optimization with multiple variables
time=0:0.001*1/120:1/120;
omega=pi*60*2;
phase=-pi:.001*2*pi:pi;
wt=omega*time;
x=wt;
y=phase;
[X,Y]=meshgrid(x,y);
Z=100*sin(X).*sin(X+Y);
mesh(Z)

title('Power Optimization')
xlabel({'Angular Position \omega x time = \theta  
(radians)';'X(0.001)(2\pi)'});
ylabel({'Phase Shift \theta_\delta';'Scale from -\pi to +\pi'});
zlabel('Power (VA)');
axis tight;

```

THIS PAGE INTENTIONALLY LEFT BLANK

APPENDIX B: DATA SHEETS [12]

SEMISTACK - IGBT



SEMITRANS Stack¹⁾

Three-phase rectifier +
inverter with brake
chopper

SEMITEACH - IGBT
SKM 50 GB 123D
SKD 51
P3/250F

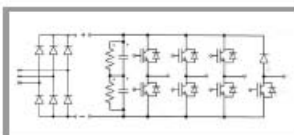
Features

- Multi-function IGBT converter
- Transparent enclosure to allow visualization of every part
- IP2x protection to minimize safety hazards
- External banana/BNC type connectors for all devices
- Integrated drive unit offering short-circuit detection/cut-off, power supply failure detection, interlock of IGBTs + galvanic isolation of the user
- Forced-air cooled heatsink

Typical Applications

- Education: One stack can simulate almost all existing industrial applications:
 - 3-phase inverter+brake chopper
 - Buck or boost converter
 - Single phase inverter
 - Single or 3-phase rectifier

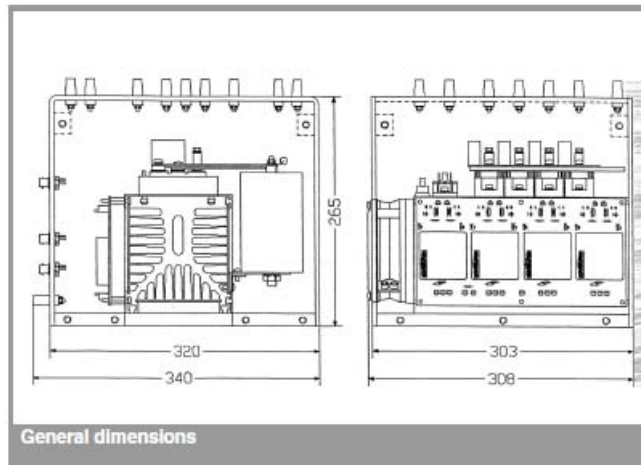
¹⁾ Photo non-contractual



B6U + B6Cl + E1CIKF

Circuit	I_{rms} (A)	V_{ac} / V_{dmax}	Types
B6Cl	30	440 / 750	SEMITEACH - IGBT

Symbol	Conditions	Values	Units
I_{rms}	no overload	30	A
V_{CES}	IGBT - 4x SKM 50 GB 123D	1200	V
$V_{CE(SAT)}$	$I_c = 50A$, $V_{GE} = 15V$, chip level; $T_j = 25(125)^{\circ}C$	2,7 (3,5)	V
V_{GES}		± 20	V
I_c	$T_{case} = 25 (80)^{\circ}C$	50 (40)	A
I_{CM}	$T_{case} = 25 (80)^{\circ}C$; $t_p = 1ms$	100 (80)	A
$V_{in(max)}$	Rectifier - 1x SKD 51/14		
	without filter	3 x 480	V
	with filter	3 x 380	V
C_{eqvl}	DC Capacitor bank - Electrolytic 2x 2200 μ F/400V	1100 / 800	μ F / V
V_{DCmax}	total equivalent capacitance max. DC voltage applied to the capacitor bank	750	V
	Driver - 4x SKHI 22		
Power supply		0 / 15	V
Current consumption	max; per driver	16	mA
Thermal trip	Normally Open type (NO)	71	$^{\circ}C$



General dimensions

This technical information specifies semiconductor devices but promises no characteristics. No warranty or guarantee expressed or implied is made regarding delivery, performance or suitability.



POWER SUPPLY MODEL 8821

The Power Supply provides fixed and variable AC and DC voltage sources, all terminated by color-coded 4 mm safety sockets. Independent circuit breakers, reset at the front panel, protect the input to and output from the Power Supply. Indicator lamps monitor the presence of input voltage in each phase. When a phase leg of the site's power service is out, the lamp goes off to reflect this condition.

A voltmeter, connected through a selector switch, monitors the variable AC and DC outputs and fixed DC output. A 24 V AC output provides a low-voltage supply required to operate other EMS equipment such as metering modules and modules used in the Power Electronics Training System.

SPECIFICATIONS

Model 8821 – Power Supply		120/208 V – 60 Hz	220/380 V – 50 Hz	240/415 V – 50 Hz
Input	Line Voltage	120/208 V	220/380 V	240/415 V
	Line Current	15 A	10 A	
	Service Installation	20 A, 3-phase, 5 wires, star (Wye)- connected, including neutral and ground		
Outputs	Fixed AC 3-Phase	120/208 V – 15 A	220/380 V – 10 A	240/415 V – 10 A
	Variable AC 3-Phase	0-120/208 V – 5 A	0-220/380 V – 3 A	0-240/415 V – 3 A
	Variable DC	0-120 V – 8 A	0-220 V – 5 A	0-240 V – 5 A
	Fixed DC	120 V – 2 A	220 V – 1 A	240 V – 1 A
	Low Power AC	24 V – 3 A		
Wall Outlet included		NEMA L21-20	NEMA L22-20	CLIPSAL 56SO520
Power Cord		3 m (10 ft)		
Physical Characteristics	Dimensions (H x W x D)	308 x 287 x 500 mm (12.1 x 11.3 x 19.7 in)		
	Net Weight	18.4 kg (40.5 lb)		

APPENDIX C: MATLAB CODE TO GENERATE CAPACITANCE OPTIMIZATION PLOT

```
%Capacitance Optimization Plot

cap = 0:1e-6:1100e-6; %Capacitance required for a given energy
volt=0:1:800;         %Change in Voltage
x=cap;
y=volt;

[X,Y]=meshgrid(x,y);
Z=.5*X.*(Y.^2); %Z=Energy=1/2CV^2

figure(1)
mesh(x,y,Z);
title('Capacitor Bank Capability');
xlabel('Capacitance (\muF)');
ylabel('Change in Voltage (\Delta Volt)');
zlabel('Energy (Joules)')
axis tight
```

THIS PAGE INTENTIONALLY LEFT BLANK

APPENDIX D: MATLAB CODE TO GENERATE FIGURES 33 THROUGH 60

```
% Different Experimental Event Times

% Experiment 1  $2^{12} \cdot 40e-9 \cdot 8191 = 1.34$  sec
% Experiment 2  $2^{13} \cdot 40e-9 \cdot 8191 = 2.68$  sec
% Experiment 3  $2^{14} \cdot 40e-9 \cdot 8191 = 5.37$  sec
% Experiment 4  $2^{14} \cdot 40e-9 \cdot 8191 = 5.37$  sec
% Experiment 5  $2^{15} \cdot 40e-9 \cdot 8191 = 10.74$  sec
% Experiment 6  $2^{16} \cdot 40e-9 \cdot 8191 = 21.47$  sec
% Experiment 7  $2^{17} \cdot 40e-9 \cdot 8191 = 42.94$  sec
% Experiment 8  $2^{18} \cdot 40e-9 \cdot 8191 = 85.89$  sec

% Different Deceleration Rates

% Experiment 1  $2^{-15} = 0.50$  sec
% Experiment 2  $2^{-16} = 0.99$  sec
% Experiment 3  $2^{-17} = 1.98$  sec
% Experiment 4  $2^{-18} = 3.96$  sec
% Experiment 5  $2^{-19} = 7.93$  sec
% Experiment 6  $2^{-20} = 15.81$  sec
% Experiment 7  $2^{-21} = 31.71$  sec
% Experiment 8  $2^{-22} = 63.25$  sec

% Trigger_Motor_Stop Delay Time

% Experiment 1  $2^{12} \cdot 40e-9 \cdot 100 = 0.02$  sec
% Experiment 2  $2^{13} \cdot 40e-9 \cdot 100 = 0.03$  sec
% Experiment 3  $2^{14} \cdot 40e-9 \cdot 100 = 0.07$  sec
% Experiment 4  $2^{14} \cdot 40e-9 \cdot 100 = 0.07$  sec
% Experiment 5  $2^{15} \cdot 40e-9 \cdot 100 = 0.13$  sec
% Experiment 6  $2^{16} \cdot 40e-9 \cdot 100 = 0.26$  sec
% Experiment 7  $2^{17} \cdot 40e-9 \cdot 100 = 0.52$  sec
% Experiment 8  $2^{18} \cdot 40e-9 \cdot 100 = 1.04$  sec

fignum=0;
figsize=[0 0 600 1200];
figsize1=[0 0 600 1200];

% Experiment Data Plot Analysis

figure(1)

subplot(3,1,1), plot(time15,omega15,time15,adc315ramp);
title ('\Angular Velocity (\omega) (0.50 Second Ramp Time)');
ylabel ('\omega (Rad/Sec)');
legend ('\omega_R_o_t_o_r', '\omega_C_o_m_m_a_n_d_e_d');
axis([0 1.4 -5 380]);
grid on;
subplot(3,1,2), plot(time15,power15);
```

```

title ('Power');
ylabel('Watts');
axis([0 1.4 -35 5]);
grid on;
subplot(3,1,3), plot(time15,cap15);
title ('Voltage Across Capacitors');
ylabel('Volts');
xlabel('Time (Seconds)');
axis([0 1.4 175 226]);
grid on;

fignum=fignum+1;
set(fignum,'OuterPosition',figsize);
saveas(fignum,'analysisone15.tif','tif');

figure(2)

subplot(3,1,1), plot(time16,omega16,time16,adc316ramp);
title ('Angular Velocity (\omega) (0.99 Second Ramp Time)');
ylabel('\omega (Rad/Sec)');
legend('\omega_R_o_t_o_r', '\omega_C_o_m_m_a_n_d_e_d');
axis([0 3 -5 380]);
grid on;
subplot(3,1,2), plot(time16,power16);
title ('Power');
ylabel('Watts');
axis([0 3 -20 5]);
grid on;
subplot(3,1,3), plot(time16,cap16);
title ('Voltage Across Capacitors');
ylabel('Volts');
xlabel('Time (Seconds)');
axis([0 3 160 220]);
grid on;

fignum=fignum+1;
set(fignum,'OuterPosition',figsize);
saveas(fignum,'analysisone16.tif','tif');

figure(3)

subplot(3,1,1), plot(time17,omega17,time17,adc317ramp);
title ('Angular Velocity (\omega) (1.98 Second Ramp Time)');
ylabel('\omega (Rad/Sec)');
legend('\omega_R_o_t_o_r', '\omega_C_o_m_m_a_n_d_e_d');
axis([0 4 -5 380]);
grid on;
subplot(3,1,2), plot(time17,power17);
title ('Power');
ylabel('Watts');
axis([0 4 -20 5]);
grid on;
subplot(3,1,3), plot(time17,cap17);
title ('Voltage Across Capacitors');

```

```

ylabel('Volts');
xlabel('Time (Seconds)');
axis([0 4 160 200]);
grid on;

fignum=fignum+1;
set(fignum,'OuterPosition',figsize);
saveas(fignum,'analysisone17.tif','tif');

figure(4)

subplot(3,1,1), plot(time18,omega18,time18,adc318ramp);
title ('Angular Velocity (\omega) (3.96 Second Ramp Time)');
ylabel('\omega (Rad/Sec)');
legend('\omega_R_o_t_o_r','\omega_C_o_m_m_a_n_d_e_d');
axis([0 6 -5 380]);
grid on;
subplot(3,1,2), plot(time18,power18);
title ('Power');
ylabel('Watts');
axis([0 6 -20 5]);
grid on;
subplot(3,1,3), plot(time18,cap18);
title ('Voltage Across Capacitors');
ylabel('Volts');
xlabel('Time (Seconds)');
axis([0 6 160 190]);
grid on;

fignum=fignum+1;
set(fignum,'OuterPosition',figsize);
saveas(fignum,'analysisone18.tif','tif');

figure(5)

subplot(3,1,1), plot(time19,omega19,time19,adc319ramp);
title ('Angular Velocity (\omega) (7.93 Second Ramp Time)');
ylabel('\omega (Rad/Sec)');
legend('\omega_R_o_t_o_r','\omega_C_o_m_m_a_n_d_e_d');
axis([0 11 -5 380]);
grid on;
subplot(3,1,2), plot(time19,power19);
title ('Power');
ylabel('Watts');
axis([0 11 -20 5]);
grid on;
subplot(3,1,3), plot(time19,cap19);
title ('Voltage Across Capacitors');
ylabel('Volts');
xlabel('Time (Seconds)');
axis([0 11 160 190]);
grid on;

fignum=fignum+1;

```

```

set(fignum, 'OuterPosition', figsize);
saveas(fignum, 'analysisone19.tif', 'tif');

figure(6)

subplot(3,1,1), plot(time20, omega20, time20, adc320ramp);
title ('Angular Velocity (\omega) (15.81 Second Ramp Time)');
ylabel ('\omega (Rad/Sec)');
legend ('\omega_R_o_t_o_r', '\omega_C_o_m_m_a_n_d_e_d');
grid on;
axis([0 22 -5 380]);
subplot(3,1,2), plot(time20, power20);
title ('Power');
ylabel ('Watts');
axis([0 22 -20 5]);
grid on;
subplot(3,1,3), plot(time20, cap20);
title ('Voltage Across Capacitors');
ylabel ('Volts');
xlabel ('Time (Seconds)');
axis([0 22 160 190]);
grid on;

fignum=fignum+1;
set(fignum, 'OuterPosition', figsize);
saveas(fignum, 'analysisone20.tif', 'tif');

figure(7)

subplot(3,1,1), plot(time21, omega21, time21, adc321ramp);
title ('Angular Velocity (\omega) (31.71 Second Ramp Time)');
ylabel ('\omega (Rad/Sec)');
legend ('\omega_R_o_t_o_r', '\omega_C_o_m_m_a_n_d_e_d');
axis([0 45 -5 380]);
grid on;
subplot(3,1,2), plot(time21, power21);
title ('Power');
ylabel ('Watts');
axis([0 45 -20 10]);
grid on;
subplot(3,1,3), plot(time21, cap21);
title ('Voltage Across Capacitors');
ylabel ('Volts');
xlabel ('Time (Seconds)');
axis([0 45 160 190]);
grid on;

fignum=fignum+1;
set(fignum, 'OuterPosition', figsize);
saveas(fignum, 'analysisone21.tif', 'tif');

figure(8)

subplot(3,1,1), plot(time22, omega22, time22, adc322ramp);

```

```

title ('Angular Velocity (\omega) (63.25 Second Ramp Time)');
ylabel ('\omega (Rad/Sec)');
legend ('\omega_R_o_t_o_r', '\omega_C_o_m_m_a_n_d_e_d');
axis([0 90 -5 380]);
grid on;
subplot(3,1,2), plot(time22,power22);
title ('Power');
ylabel('Watts');
axis([0 90 -20 10]);
grid on;
subplot(3,1,3), plot(time22,cap22);
title ('Voltage Across Capacitors');
ylabel('Volts');
xlabel('Time (Seconds)');
axis([0 90 160 190]);
grid on;

fignum=fignum+1;
set(fignum, 'OuterPosition', figsize);
saveas(fignum, 'analysisone22.tif', 'tif');

% Comparison Analysis

figure(9)

subplot(3,1,1),
plot(time15,omega15,time15,adc315ramp,time16,omega16,time16,adc316ramp)
title ('Angular Velocity (\omega) Comparison');
ylabel ('\omega (Rad/Sec)');
legend ('\omega_R_o_t_o_r 0.5 sec', '\omega_C_o_m_m_a_n_d_e_d 0.5
sec', '\omega_R_o_t_o_r 0.99 sec', '\omega_C_o_m_m_a_n_d_e_d 0.99 sec');
axis([0 3 -5 380]);
grid on;
subplot(3,1,2), plot(time15,power15,time16,power16);
title ('Power Comparison');
ylabel('Watts');
legend('0.50 sec', '0.99 sec');
axis([0 3 -35 10]);
grid on;
subplot(3,1,3), plot(time15,cap15,time16,cap16);
title ('Voltage Across Capacitors Comparison');
ylabel('Volts');
xlabel('Time (Seconds)');
legend('0.50 sec', '0.99 sec');
axis([0 3 160 226]);
grid on;

fignum=fignum+1;
set(fignum, 'OuterPosition', figsize);
saveas(fignum, 'analysistwo15.tif', 'tif');

figure(10)

```

```

subplot(3,1,1),
plot(time16,omega16,time16,adc316ramp,time17,omega17,time17,adc317ramp)
title ('Angular Velocity (\omega) Comparison');
ylabel('\omega (Rad/Sec)');
legend('\omega_R_o_t_o_r 0.99 sec', '\omega_C_o_m_m_a_n_d_e_d 0.99
sec', '\omega_R_o_t_o_r 1.98 sec', '\omega_C_o_m_m_a_n_d_e_d 1.98 sec');
axis([0 6 -5 380]);
grid on;
subplot(3,1,2), plot(time16,power16,time17,power17);
title ('Power Comparison');
ylabel('Watts');
axis([0 6 -20 10]);
legend('0.99 sec', '1.98 sec');
grid on;
subplot(3,1,3), plot(time16,cap16,time17,cap17);
title ('Voltage Across Capacitors Comparison');
ylabel('Volts');
xlabel('Time (Seconds)');
legend('0.99 sec', '1.98 sec');
axis([0 6 160 220]);
grid on;

fignum=fignum+1;
set(fignum, 'OuterPosition', figsize);
saveas(fignum, 'analysistwol6.tif', 'tif');

figure(11)

subplot(3,1,1),
plot(time17,omega17,time17,adc317ramp,time18,omega18,time18,adc318ramp)
title ('Angular Velocity (\omega) Comparison');
ylabel('\omega (Rad/Sec)');
axis([0 6 -5 380]);
legend('\omega_R_o_t_o_r 1.98 sec', '\omega_C_o_m_m_a_n_d_e_d 1.98
sec', '\omega_R_o_t_o_r 3.96 sec', '\omega_C_o_m_m_a_n_d_e_d 3.96 sec');
grid on;
subplot(3,1,2), plot(time17,power17,time18,power18);
title ('Power Comparison');
ylabel('Watts');
axis([0 6 -20 10]);
legend('1.98 sec', '3.96 sec');
grid on;
subplot(3,1,3), plot(time17,cap17,time18,cap18);
title ('Voltage Across Capacitors Comparison');
ylabel('Volts');
xlabel('Time (Seconds)');
axis([0 6 160 200]);
legend('1.98 sec', '3.96 sec');
grid on;

fignum=fignum+1;
set(fignum, 'OuterPosition', figsize);
saveas(fignum, 'analysistwol7.tif', 'tif');

```

```

figure(12)

subplot(3,1,1),
plot(time18,omega18,time18,adc318ramp,time19,omega19,time19,adc319ramp)
title ('Angular Velocity (\omega) Comparison');
ylabel ('\omega (Rad/Sec)');
axis([0 11 -5 380]);
grid on;
legend('\omega_R_o_t_o_r 3.96 sec', '\omega_C_o_m_m_a_n_d_e_d 3.96
sec', '\omega_R_o_t_o_r 7.93 sec', '\omega_C_o_m_m_a_n_d_e_d 7.93 sec');
subplot(3,1,2), plot(time18,power18,time19,power19);
title ('Power Comparison');
ylabel('Watts');
axis([0 11 -20 5]);
legend('3.96 sec', '7.93 sec');
grid on;
subplot(3,1,3), plot(time18,cap18,time19,cap19);
title ('Voltage Across Capacitors Comparison');
ylabel('Volts');
xlabel('Time (Seconds)');
axis([0 11 165 185]);
legend('3.96 sec', '7.93 sec');
grid on;

fignum=fignum+1;
set(fignum, 'OuterPosition', figsize);
saveas(fignum, 'analysistwo18.tif', 'tif');

figure(13)

subplot(3,1,1),
plot(time19,omega19,time19,adc319ramp,time20,omega20,time20,adc320ramp)
title ('Angular Velocity (\omega) Comparison');
ylabel ('\omega (Rad/Sec)');
legend('\omega_R_o_t_o_r 7.93 sec', '\omega_C_o_m_m_a_n_d_e_d 7.93
sec', '\omega_R_o_t_o_r 15.81 sec', '\omega_C_o_m_m_a_n_d_e_d 15.81
sec');
axis([0 22 -5 380]);
grid on;
subplot(3,1,2), plot(time19,power19,time20,power20);
title ('Power Comparison');
ylabel('Watts');
legend('7.93 sec', '15.81 sec');
axis([0 22 -20 5]);
grid on;
subplot(3,1,3), plot(time19,cap19,time20,cap20);
title ('Voltage Across Capacitors Comparison');
ylabel('Volts');
xlabel('Time (Seconds)');
legend('7.93 sec', '15.81 sec');
axis([0 22 165 185]);
grid on;

fignum=fignum+1;

```

```

set(fignum, 'OuterPosition', figsize);
saveas(fignum, 'analysistwo19.tif', 'tif');

figure(14)

subplot(3,1,1),
plot(time20, omega20, time20, adc320ramp, time21, omega21, time21, adc321ramp)
title ('Angular Velocity (\omega)');
ylabel('\omega (Rad/Sec)');
legend('\omega_R_o_t_o_r 15.81 sec', '\omega_C_o_m_m_a_n_d_e_d 15.81 sec', '\omega_R_o_t_o_r 31.71 sec', '\omega_C_o_m_m_a_n_d_e_d 31.71 sec');
axis([0 45 -5 380]);
grid on;
subplot(3,1,2), plot(time20, power20, time21, power21);
title ('Power Comparison');
ylabel('Watts');
legend('15.81 sec', '31.71 sec');
axis([0 45 -20 5]);
grid on;
subplot(3,1,3), plot(time20, cap20, time21, cap21);
title ('Voltage Across Capacitors Comparison');
ylabel('Volts');
xlabel('Time (Seconds)');
legend('15.81 sec', '31.71 sec');
axis([0 45 165 190]);
grid on;

fignum=fignum+1;
set(fignum, 'OuterPosition', figsize);
saveas(fignum, 'analysistwo20.tif', 'tif');

figure(15)

subplot(3,1,1),
plot(time21, omega21, time21, adc321ramp, time22, omega22, time22, adc322ramp)
title ('Angular Velocity (\omega)');
ylabel('\omega (Rad/Sec)');
legend('\omega_R_o_t_o_r 31.71 sec', '\omega_C_o_m_m_a_n_d_e_d 31.71 sec', '\omega_R_o_t_o_r 63.25 sec', '\omega_C_o_m_m_a_n_d_e_d 63.25 sec');
axis([0 90 -5 380]);
grid on;
subplot(3,1,2), plot(time21, power21, time22, power22);
title ('Power');
ylabel('Watts');
legend('31.71 sec', '63.25 sec');
axis([0 90 -20 5]);
grid on;
subplot(3,1,3), plot(time21, cap21, time22, cap22);
title ('Voltage Across Capacitors');
ylabel('Volts');
xlabel('Time (Seconds)');
legend('31.71 sec', '63.25 sec');

```



```

axis([0 90 165 190]);
grid on;

fignum=fignum+1;
set(fignum, 'OuterPosition',figsize);
saveas(fignum, 'analysistwo21.tif', 'tif');

% Angular Velocity Analysis

figure(16)

compare15=adc315ramp'-omega15;
subplot(3,1,1), plot(time15,compare15);
title ('Angular Velocity Difference (\omega)');
ylabel ('\omega (Rad/Sec)');
axis([0 1.4 -100 20]);
grid on;
subplot(3,1,2), plot(time15,power15);
title ('Power');
ylabel ('Watts');
axis([0 1.4 -32 1]);
grid on;
subplot(3,1,3), plot(time15,cap15);
title ('Voltage Across Capacitors');
ylabel ('Volts');
xlabel ('Time (Seconds)');
axis([0 1.4 175 226]);
grid on;

fignum=fignum+1;
set(fignum, 'OuterPosition',figsize);
saveas(fignum, 'analysisthree15.tif', 'tif');

figure(17)

compare16=adc316ramp'-omega16;
subplot(3,1,1), plot(time16,compare16);
title ('Angular Velocity Difference (\omega)');
ylabel ('\omega (Rad/Sec)');
axis([0 3 -50 20]);
grid on;
subplot(3,1,2), plot(time16,power16);
title ('Power');
ylabel ('Watts');
axis([0 3 -20 1]);
grid on;
subplot(3,1,3), plot(time16,cap16);
title ('Voltage Across Capacitors');
ylabel ('Volts');
xlabel ('Time (Seconds)');
axis([0 3 175 226]);
grid on;

fignum=fignum+1;

```

```

set(fignum, 'OuterPosition', figsize);
saveas(fignum, 'analysisthreel6.tif', 'tif');

figure(18)

compare17=adc317ramp'-omega17;
subplot(3,1,1), plot(time17,compare17);
title ('Angular Velocity Difference (\omega)');
ylabel('\omega (Rad/Sec)');
axis([0 6 -35 20]);
grid on;
subplot(3,1,2), plot(time17,power17);
title ('Power');
ylabel('Watts');
axis([0 6 -20 5]);
grid on;
subplot(3,1,3), plot(time17,cap17);
title ('Voltage Across Capacitors');
ylabel('Volts');
xlabel('Time (Seconds)');
axis([0 6 160 200]);
grid on;

fignum=fignum+1;
set(fignum, 'OuterPosition', figsize);
saveas(fignum, 'analysisthreel7.tif', 'tif');

figure(19)

compare18=adc318ramp'-omega18;
subplot(3,1,1), plot(time18,compare18);
title ('Angular Velocity Difference (\omega)');
ylabel('\omega (Rad/Sec)');
axis([0 6 -20 20]);
grid on;
subplot(3,1,2), plot(time18,power18);
title ('Power');
ylabel('Watts');
axis([0 6 -20 5]);
grid on;
subplot(3,1,3), plot(time18,cap18);
title ('Voltage Across Capacitors');
ylabel('Volts');
xlabel('Time (Seconds)');
axis([0 6 165 185]);
grid on;

fignum=fignum+1;
set(fignum, 'OuterPosition', figsize);
saveas(fignum, 'analysisthreel8.tif', 'tif');

figure(20)

compare19=adc319ramp'-omega19;

```

```

subplot(3,1,1), plot(time19,compare19);
title ('Angular Velocity Difference (\omega)');
ylabel('\omega (Rad/Sec)');
axis([0 11 -20 20]);
grid on;
subplot(3,1,2), plot(time19,power19);
title ('Power');
ylabel('Watts');
axis([0 11 -20 20]);
grid on;
subplot(3,1,3), plot(time19,cap19);
title ('Voltage Across Capacitors');
ylabel('Volts');
xlabel('Time (Seconds)');
axis([0 11 165 185]);
grid on;

fignum=fignum+1;
set(fignum, 'OuterPosition',figsize);
saveas(fignum, 'analysisthree19.tif', 'tif');

figure(21)

compare20=adc320ramp'-omega20;
subplot(3,1,1), plot(time20,compare20);
title ('Angular Velocity Difference (\omega)');
ylabel('\omega (Rad/Sec)');
axis([0 22 -35 20]);
grid on;
subplot(3,1,2), plot(time20,power20);
title ('Power');
ylabel('Watts');
axis([0 22 -20 5]);
grid on;
subplot(3,1,3), plot(time20,cap20);
title ('Voltage Across Capacitors');
ylabel('Volts');
xlabel('Time (Seconds)');
axis([0 22 165 185]);
grid on;

fignum=fignum+1;
set(fignum, 'OuterPosition',figsize);
saveas(fignum, 'analysisthree20.tif', 'tif');

figure(22)

compare21=adc321ramp'-omega21;
subplot(3,1,1), plot(time21,compare21);
title ('Angular Velocity Difference (\omega)');
ylabel('\omega (Rad/Sec)');
axis([0 44 -35 20]);
grid on;
subplot(3,1,2), plot(time21,power21);

```

```

title ('Power');
ylabel('Watts');
axis([0 44 -25 2]);
grid on;
subplot(3,1,3), plot(time21,cap21);
title ('Voltage Across Capacitors');
ylabel('Volts');
xlabel('Time (Seconds)');
axis([0 44 165 190]);
grid on;

fignum=fignum+1;
set(fignum,'OuterPosition',figsize);
saveas(fignum,'analysisthree21.tif','tif');

figure(23)

compare22=adc322ramp'-omega22;
subplot(3,1,1), plot(time22,compare22);
title ('Angular Velocity Difference (\omega)');
ylabel('\omega (Rad/Sec)');
axis([0 90 -5 20]);
grid on;
subplot(3,1,2), plot(time22,power22);
title ('Power');
ylabel('Watts');
axis([0 90 -20 10]);
grid on;
subplot(3,1,3), plot(time22,cap22);
title ('Voltage Across Capacitors');
ylabel('Volts');
xlabel('Time (Seconds)');
axis([0 90 160 190]);
grid on;

fignum=fignum+1;
set(fignum,'OuterPosition',figsize);
saveas(fignum,'analysisthree22.tif','tif');

% Current Behavior Analysis

figure(24)

subplot(4,1,1), plot(time15,omega15);
title ('Angular Velocity (\omega)');
ylabel('\omega (Rad/Sec)');
axis([0 1.4 -1 380]);
grid on;
subplot(4,1,2), plot(time15,power15);
title ('Power');
ylabel('Watts');
axis([0 1.4 -36 2]);
grid on;
subplot(4,1,3), plot(time15,cap15);

```

```

title ('Voltage Across Capacitors');
ylabel('Volts');
axis([0 1.4 160 227]);
grid on;
subplot(4,1,4), plot(time15,icurrent15);
title ('Phase A Current');
ylabel('Amps');
xlabel('Time (Seconds)');
axis([0 1.4 -2.5 2.5]);
grid on;

fignum=fignum+1;
set(fignum,'OuterPosition',figsize1);
saveas(fignum,'analysisfour15.tif','tif');

figure(25)

subplot(4,1,1), plot(time16,omega16);
title ('Angular Velocity (\omega)');
ylabel('\omega (Rad/Sec)');
axis([0 3 -1 380]);
grid on;
subplot(4,1,2), plot(time16,power16);
title ('Power');
ylabel('Watts');
axis([0 3 -20 1]);
grid on;
subplot(4,1,3), plot(time16,cap16);
title ('Voltage Across Capacitors');
ylabel('Volts');
axis([0 3 160 226]);
grid on;
subplot(4,1,4), plot(time16,icurrent16);
title ('Phase A Current');
ylabel('Amps');
xlabel('Time (Seconds)');
axis([0 3 -2 2]);
grid on;

fignum=fignum+1;
set(fignum,'OuterPosition',figsize1);
saveas(fignum,'analysisfour16.tif','tif');

figure(26)

subplot(4,1,1), plot(time17,omega17);
title ('Angular Velocity (\omega)');
ylabel('\omega (Rad/Sec)');
axis([0 4 -5 380]);
grid on;
subplot(4,1,2), plot(time17,power17);
title ('Power');
ylabel('Watts');
axis([0 4 -20 5]);

```

```

grid on;
subplot(4,1,3), plot(time17,cap17);
title ('Voltage Across Capacitors');
ylabel('Volts');
xlabel('Time (Seconds)');
axis([0 4 160 200]);
grid on;
subplot(4,1,4), plot(time17,icurrent17);
title ('Phase A Current');
ylabel('Amps');
xlabel('Time (Seconds)');
axis([0 4 -2 2]);
grid on;

fignum=fignum+1;
set(fignum,'OuterPosition',figsize1);
saveas(fignum,'analysisfour17.tif','tif');

% Energy Conservation Analysis

% kerotate=.5*2.04e-3*(1670/60*2*pi())^2

% Total Power Calculation = I^R + Regenerative Power

% Ramp CMD starts to zero at 616 goes to zero at 3623 Delay =
0.10092544
% Ramp CMD starts to zero at 3055 goes to zero at 6062 Delay =
1.00106240

epwr15time=0:2^12*40e-9:(3623-616)*2^12*40e-9;
epwr16time=0:2^13*40e-9:(6062-3055)*2^13*40e-9;

epwr15energy=max(epwr15final)
epwr16energy=max(epwr16final)

% irlossenergytotal15=irenergytotal151(3623,1)-irenergytotal151(616,1)
% irlossenergytotal16=irenergytotal161(6062,1)-irenergytotal161(3055,1)
%
% powerregentotal15=-
powertotalenergy15(3623,1)+powertotalenergy15(616,1)
% powerregentotal16=-
powertotalenergy16(6062,1)+powertotalenergy16(3055,1)
%
% totalpower15=irlossenergytotal15+powerregentotal15
% totalpower16=irlossenergytotal16+powerregentotal16

% loop=1;
% te=1:8190;
% while loop <= 8190;
% kenergyvolt15(loop,1)=.5*1100e-6*(cap15(loop+1,1)^2-cap15(loop,1)^2);
% kenergyvolt16(loop,1)=.5*1100e-6*(cap16(loop+1,1)^2-cap16(loop,1)^2);
% loop=loop+1;
% end
%
```

```

% kenergy15=trapz(kenergy15volt1)
% kenergy16=trapz(kenergy16volt1)

% kel5volt=.5*1100e-6*(225.38^2-180^2) %Ramp CMD goes to zero at 3624
% kel6volt=.5*1100e-6*(225.10^2-180^2) %Ramp CMD goes to zero at 6063

motorresistance=12;

irloss15=3*icurrent15.^2*motorresistance;
irloss16=3*icurrent16.^2*motorresistance;

% irenergy15=trapz(irloss15)
% irenergy16=trapz(irloss16)

figure(27)

subplot(5,1,1), plot(time15,omega15,time15,adc315ramp);
title ('Angular Velocity (\omega) (0.50 Second Ramp Time)');
ylabel ('\omega (Rad/Sec)');
legend ('\omega_R_o_t_o_r', '\omega_C_o_m_m_a_n_d_e_d');
axis([0 1.4 -5 380]);
grid on;
compare15=adc315ramp'-omega15;
subplot(5,1,2), plot(time15,compare15);
title ('Angular Velocity Difference (\omega)');
ylabel ('\omega (Rad/Sec)');
axis([0 1.4 -100 20]);
grid on;
subplot(5,1,3), plot(time15,icurrent15);
title ('Phase A Current');
ylabel ('Amps');
xlabel ('Time (Seconds)');
grid on;
axis([0 1.4 -2.5 2.5]);
subplot(5,1,4), plot(time15,irenergy15);
title ('I^2R Power Loss');
ylabel ('Watts');
axis([0 1.4 0 30]);
grid on;
subplot(5,1,5), plot(time15,-power15);
title ('Regenerative Power');
ylabel ('Watts');
axis([0 1.4 -5 35]);
grid on;

fignum=fignum+1;
set(fignum, 'OuterPosition', figsize);
saveas(fignum, 'analysisfive15.tif', 'tif');

figure(28)

subplot(5,1,1), plot(time16,omega16,time16,adc316ramp);
title ('Angular Velocity (\omega) (0.99 Second Ramp Time)');
ylabel ('\omega (Rad/Sec)');

```

```

legend('\omega_R_o_t_o_r', '\omega_C_o_m_m_a_n_d_e_d');
axis([0 3 -5 380]);
grid on;
compare16=adc316ramp'-omega16;
subplot(5,1,2), plot(time16,compare16);
title ('Angular Velocity Difference (\omega)');
ylabel('\omega (Rad/Sec)');
axis([0 3 -50 20]);
grid on;
subplot(5,1,3), plot(time16,icurrent16);
title ('Phase A Current');
ylabel('Amps');
xlabel('Time (Seconds)');
grid on;
subplot(5,1,4), plot(time16,irenergy16);
title ('I^2R Power Losse');
ylabel('Watts');
axis([0 3 0 22]);
grid on;
subplot(5,1,5), plot(time16,-power16);
title ('Regenerative Power');
ylabel('Watts');
axis([0 3 -5 20]);
grid on;

fignum=fignum+1;
set(fignum, 'OuterPosition', figsize);
saveas(fignum, 'analysisfivel6.tif', 'tif');

% Plotting only Deceleration Event

timed15=1:3623-616;
justenergyir15(:,1)=irenergytotal151(615+timed15,1);
justenergypower15(:,1)=-powertotalenergy15(615+timed15,1);
justramp15(:,1)=adc315ramp(1,615+timed15)';
justomega15(:,1)=omega15(615+timed15,1);

timed16=1:6062-3055;
justenergyir16(:,1)=irenergytotal161(3054+timed16,1);
justenergypower16(:,1)=-powertotalenergy16(3054+timed16,1);
justramp16(:,1)=adc316ramp(1,3054+timed16)';
justomega16(:,1)=omega16(3054+timed16,1);

justenergymeasured15=max(justenergyir15(:,1)+justenergypower15(:,1))-
min(justenergyir15()-justenergypower15(:,1));
justenergymeasured16=max(justenergyir16(:,1)+justenergypower16(:,1))-
min(justenergyir16()-justenergypower16(:,1));

figure(29)

time15d=0:2^12*40e-9:3006*2^12*40e-9;
subplot(3,1,1), plot(time15d,justomega15,time15d,justramp15);
title ('Angular Velocity (\omega) (0.50 Second Ramp Time)');

```



```

ylabel('\omega (Rad/Sec)');
legend('\omega_R_o_t_o_r', '\omega_C_o_m_m_a_n_d_e_d');
grid on;
axis([0 0.5 0 380]);
subplot(3,1,2), plot(time15d,justenergyir15);
title ('I^2R Energy Lost');
ylabel('Joules');
axis([0 0.5 0 10]);
grid on;
subplot(3,1,3), plot(epwr15time,epwr15);
title ('Energy Regenerated');
ylabel('Joules');
axis([0 0.5 0 7]);
grid on;

fignum=fignum+1;
set(fignum, 'OuterPosition', figsize);
saveas(fignum, 'analysissix15.tif', 'tif');

figure(30)

time16d=0:2^13*40e-9:3006*2^13*40e-9;
subplot(3,1,1), plot(time16d,justomega16,time16d,justramp16);
title ('Angular Velocity (\omega) (0.98 Second Ramp Time)');
ylabel('\omega (Rad/Sec)');
legend('\omega_R_o_t_o_r', '\omega_C_o_m_m_a_n_d_e_d');
grid on;
axis([0 1 0 380]);
subplot(3,1,2), plot(time16d,justenergyir16-3.1802);
title ('I^2R Energy Lost');
ylabel('Joules');
axis([0 1 0 15.5]);
grid on;
subplot(3,1,3), plot(epwr16time,epwr16);
title ('Energy Regenerated');
ylabel('Joules');
axis([0 1 0 15]);
grid on;

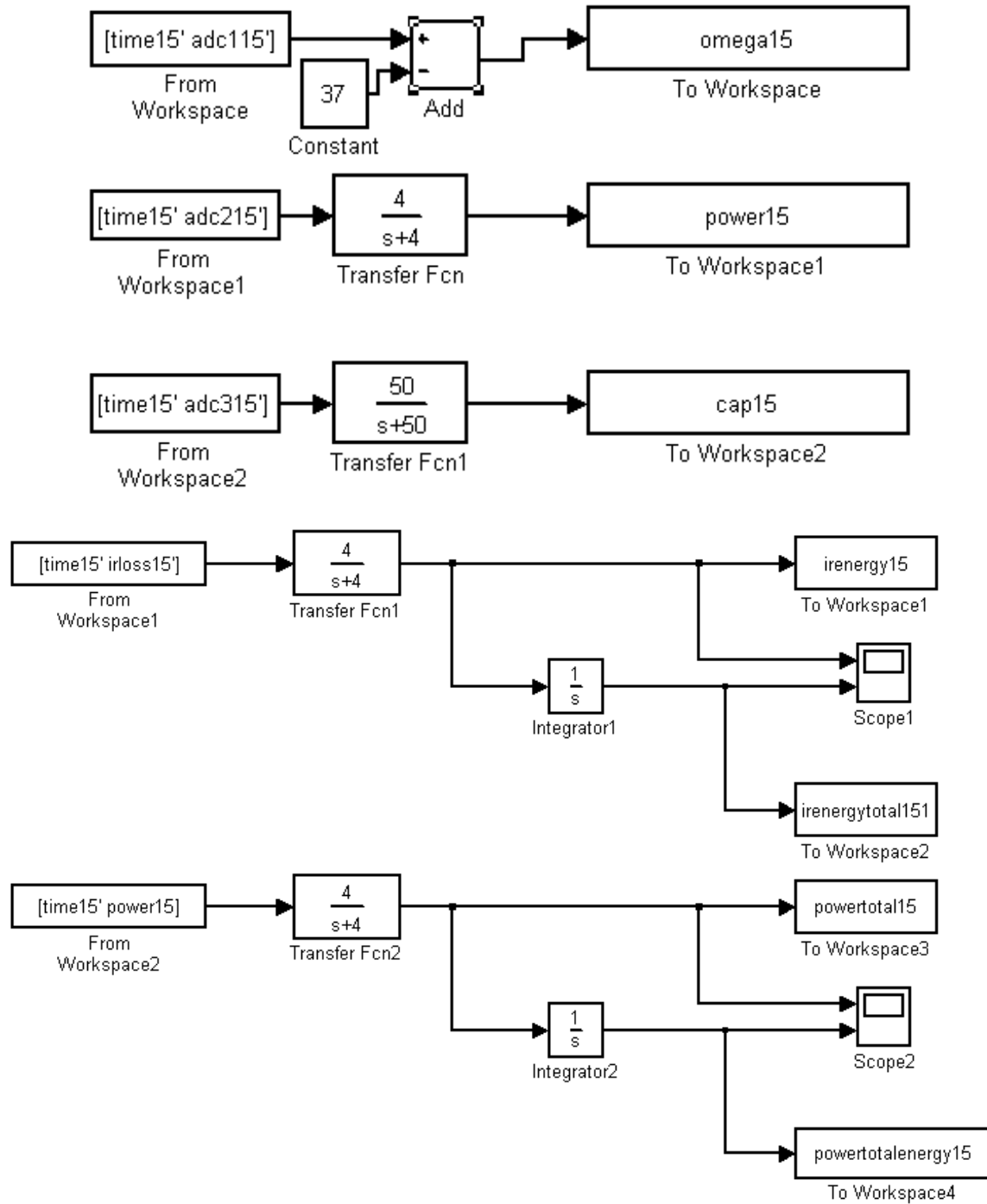
fignum=fignum+1;
set(fignum, 'OuterPosition', figsize);
saveas(fignum, 'analysissix16.tif', 'tif');

```

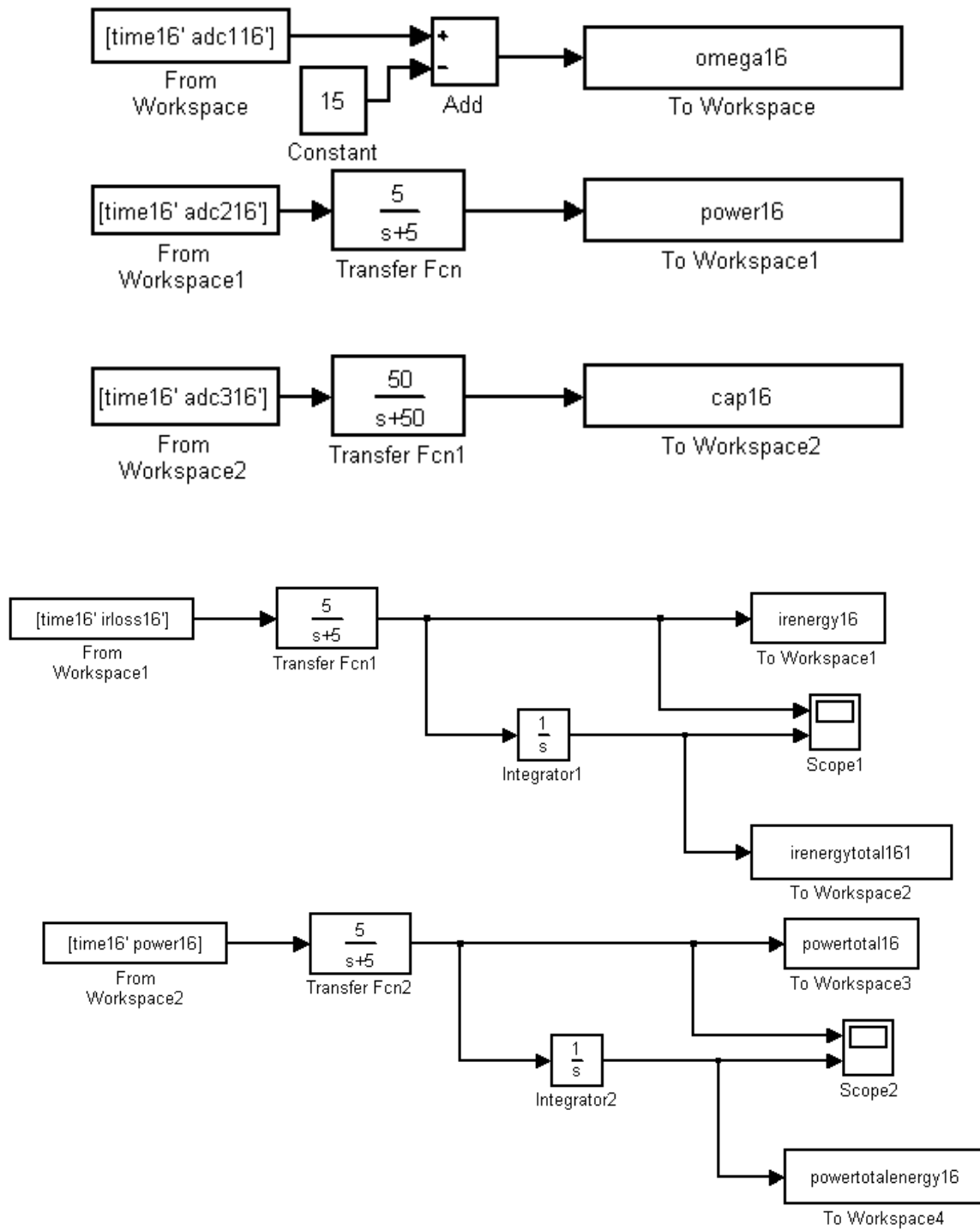
THIS PAGE INTENTIONALLY LEFT BLANK

APPENDIX E: FILTER DESIGNS

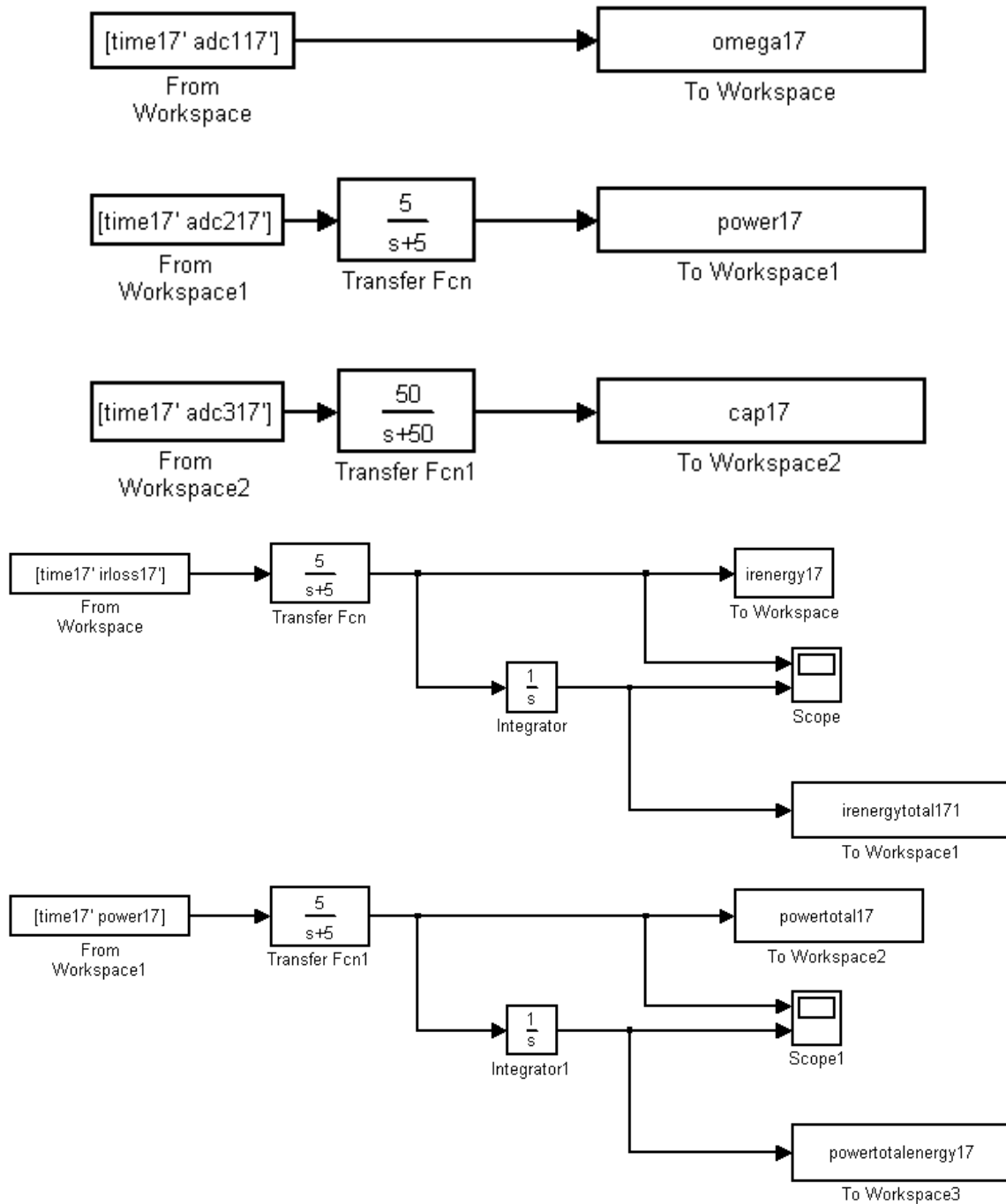
Experiment 1 SimuLink Filter Design



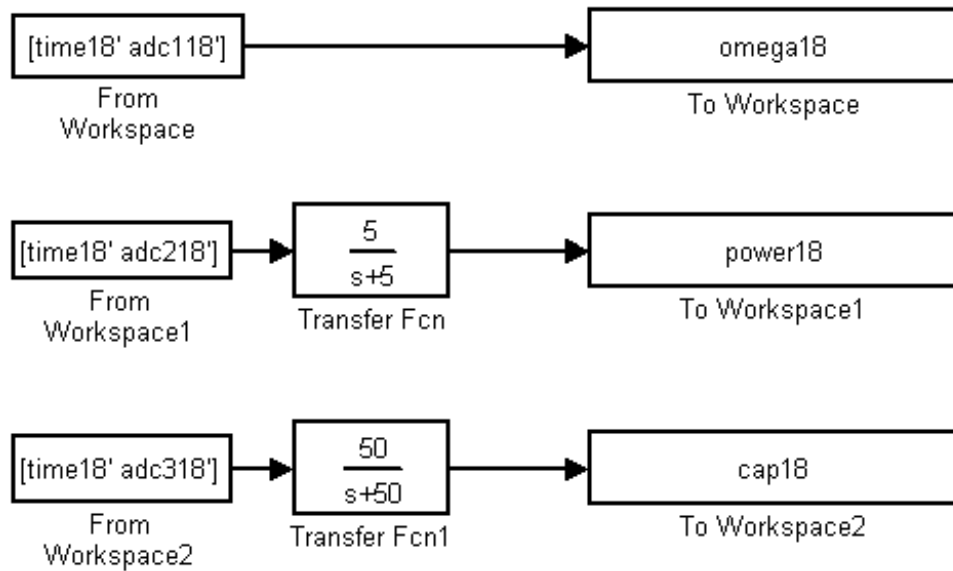
Experiment 2 SimuLink Filter Design



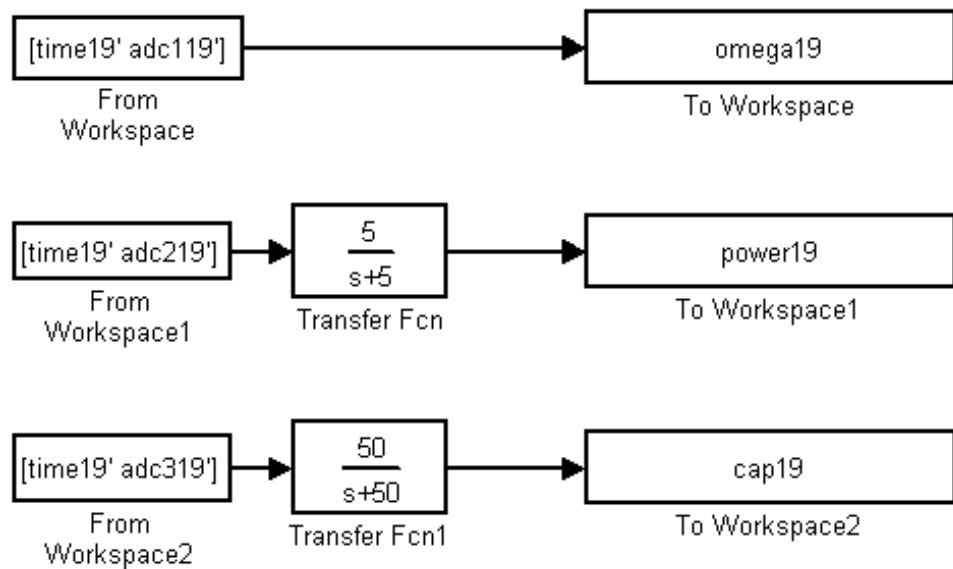
Experiment 3 SimuLink Filter Design



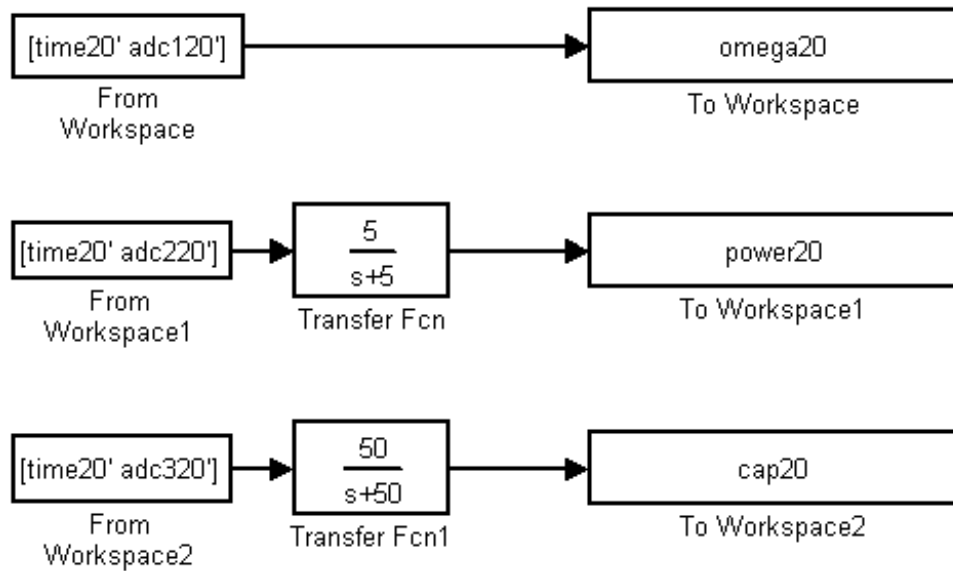
Experiment 4 Filter Design



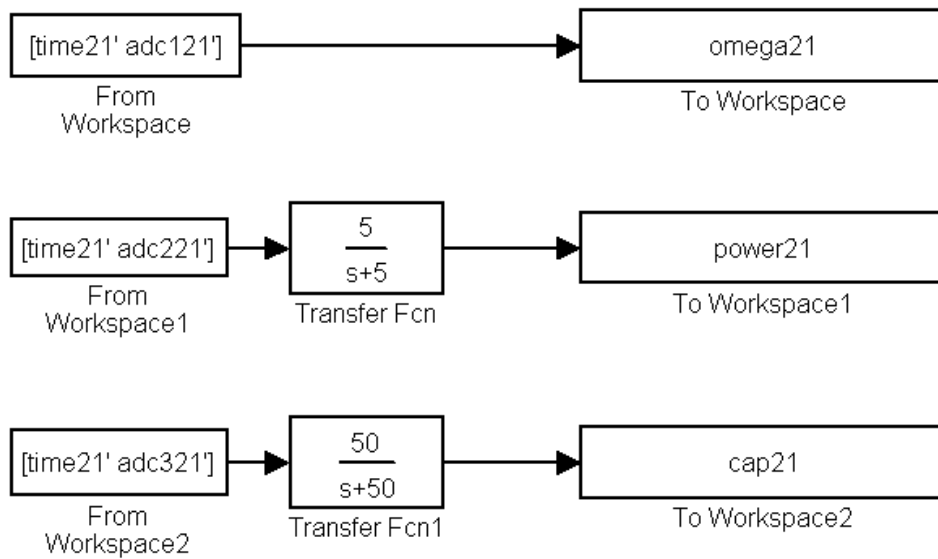
Experiment 5 SimuLink Filter Design



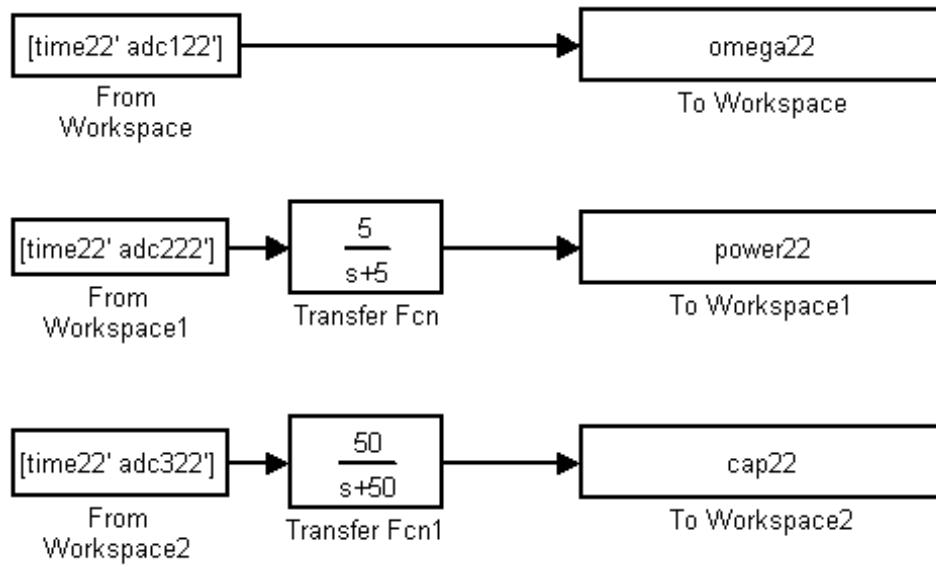
Experiment 6 SimuLink Filter Design



Experiment 7 SimuLink Filter Design

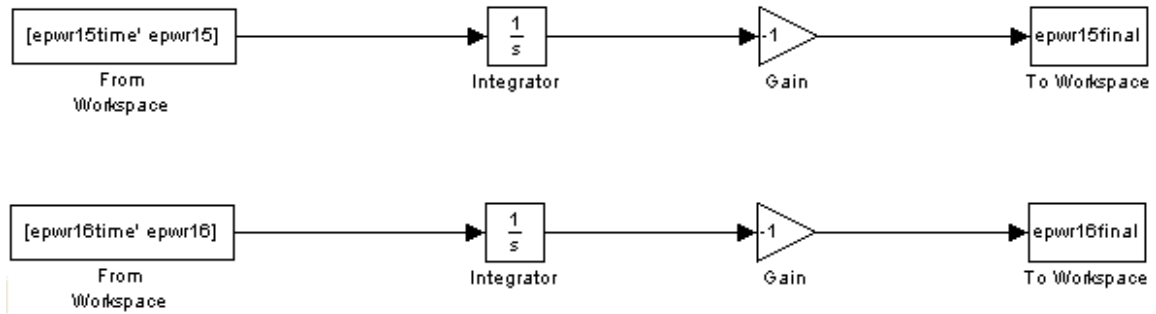


Experiment 8 Filter Design



APPENDIX F: POWER INTEGRATOR TO CALCULATE ENERGY

Experiments 1 and 2 Regenerative Energy Integrator



THIS PAGE INTENTIONALLY LEFT BLANK

LIST OF REFERENCES

- [1] D. Smith, "Encyclopedia, Automobile Industry," history.com, [Online]. Available: <http://www.history.com/encyclopedia.do?articleId=201868> [Accessed: January 11, 2010].
- [2] Anonymous, "The History of Electric Vehicles, The Early Years - Electric Cars (1890–1930)," about.com, [Online]. Available: <http://inventors.about.com/library/weekly/aacarselectrica.htm> [Accessed: January 21, 2010].
- [3] Anonymous, "Victor Wouk and The Great Hybrid Car Cover-up of 1974," hybridcars.com, [Online]. Available: <http://www.hybridcars.com/history/the-great-hybrid-car-cover-up-of-74.html> [Accessed: January 10, 2010].
- [4] T. Painter, "Recovering Railroad Diesel-Electric Locomotive Dynamic Brake Energy," M.S. thesis, University of Illinois at Urbana-Champaign, 2006.
- [5] S. T. Robertson, and J. D. Markham, The Regenerative Braking Story, The Scottish Tramway & Transport Society and Venture Publications LTD., 2006, pp. 14–50.
- [6] A. Allaby, and M. Allaby, "self-exciting dynamo." A Dictionary of Earth Sciences. 1999. encyclopedia.com, [Online] Available: <http://www.encyclopedia.com/doc/1O13-selfexcitingdynamo.html> [Accessed: January 20, 2010].
- [7] Anonymous, "Compound Winding", Answers.com, [Online]. Available: <http://www.answers.com/topic/compound-winding> [Accessed: January 20, 2010].
- [8] Anonymous, "Asynchronous (Induction Generators)," Talentfactory.dk, [Online]. Available: <http://www.talentfactory.dk/en/tour/wtrb/async.htm> [Accessed: May 24, 2010].
- [9] Paul C. Krause, Oleg Wasynczuk, and Scott D. Sudhoff, "Analysis of Electric Machinery and Drive Systems, Second Edition," John Wiley & Sons Inc., 2002.
- [10] Anonymous, "Three Phase Induction Machine," Naval Postgraduate School, Monterey, CA EC4130 Laboratory Experiment #1 October 15, 1997.
- [11] Dr. G. Oriti, "Three Phase Voltage Source Inverter (VSI) Driving an Induction Motor with Open Loop V/f Control," Naval Postgraduate School, Monterey, CA EC4150 Laboratory #3 – rev2 November 2008.

- [12] G. Edwards, "Wind Turbine Power Generation Emulation Via Doubly Fed Induction Generator Control," M.S. thesis, Naval Postgraduate School, Monterey, CA, 2009.
- [13] C. R. Nave, "Rotational Kinetic Energy," 2005, Georgia State University, Hyperphysics, [Online]. Available: <http://hyperphysics.phy-astr.gsu.edu/hbase/rke.html#rke> [Accessed: May 01, 2010].
- [14] C. R. Nave, "Storing Energy in a Capacitor," 2005, Georgia State University, Hyperphysics, [Online]. Available: <http://hyperphysics.phy-astr.gsu.edu/hbase/electric/capeng2.html> [Accessed: May 01, 2010].
- [15] Anonymous, "MATWEB Material Property Data," Matweb.com, [Online]. Available:
<http://www.matweb.com/search/DataSheet.aspx?MatGUID=098700ed63b24b14bd3bfdbec937489f> [Accessed: May 24, 2010].
- [16] Anonymous, "MATWEB Material Property Data," Matweb.com, [Online]. Available:
<http://www.matweb.com/search/DataSheet.aspx?MatGUID=ab9706916818406b80c22b7f39db0c78> [Accessed: May 24, 2010].
- [17] C. R. Nave, "Moment of Inertia," 2005, Georgia State University, Hyperphysics, [Online]. Available: <http://hyperphysics.phy-astr.gsu.edu/hbase/hframe.html> [Accessed: May 01, 2010].
- [18] C. R. Nave, "Thick Hoops and Hollow Cylinders," 2005, Georgia State University, Hyperphysics, [Online]. Available: <http://hyperphysics.phy-astr.gsu.edu/hbase/hframe.html> [Accessed: May 01, 2010].
- [19] A. L. Julian, Professor, Department of Electrical and Computer Engineering, Naval Postgraduate School, Monterey, California.

INITIAL DISTRIBUTION LIST

1. Defense Technical Information Center
Ft. Belvoir, Virginia
2. Dudley Knox Library
Naval Postgraduate School
Monterey, California
3. Dr. Alexander Julian
Electrical Engineering and Computer Department
Code EC/J1
Naval Postgraduate School
Monterey, California
4. Dr. Roberto Cristi
Electrical Engineering and Computer Department
Code EC/C1
Naval Postgraduate School
Monterey, California